POLITECNICO
MILANO 1863

SCUOLA DI INGEGNERIA INDUSTRIALE
E DELL'INFORMAZIONE

Computational Fluid Dynamics Investigation and Validation on Bike Wheels Rotation Modeling

Tesi di Laurea Magistrale in
Mechanical Engineering - Ingegneria Meccanica

Author: **Federico Amadori**

Student ID: 971231
Advisor: Prof. Paolo Schito
Co-advisors:
Academic Year: 2022-23

Abstract

Aerodynamic drag plays an important role in cycling races and can determine victory or defeat. One of the main contributors to the overall drag of a bicycle are the wheels. The flow that develops through the rotating wheel is complex and no standard approach for simulating individual wheels can be found in the literature. High accuracy is achieved with the Sliding Mesh (SM) approach, but it requires high computational costs. Therefore, there are steady-state methods such as Rotating Wall Boundary Condition (RWBC) or Moving Reference Frame (MRF) that reduce the computational time, but it is not clear to what extent their application is sensitive to the computational parameters.

This work focuses on the comparison of different rotation models applied to the lenticular wheel and spoked wheel. First, a validation test is performed comparing the simulation results with a previous wind tunnel test campaign. Then, the three standard methods (RWBC, MRF, SM) are compared for both wheels at different yaw angles to find the best way to estimate the flow and forces. A DDES simulation using MRF is performed for both wheels to verify the difference between a steady-state and a transient turbulence model. For the spoked wheel, an alternative approach is also implemented based on replacing the actual spoke geometry with volume forces derived using the BET method. With this method, a better mesh quality can be obtained to avoid the meshing procedure of the spokes, which can cause skewness. For all methods, the solutions are compared qualitatively and quantitatively.

The results show that the applied rotational approach plays an important role. In particular, the MRF can have a significant impact on the flow characteristics and force prediction, even though it is widely used in the literature. An optimized way to apply the MRF approach is developed, which shows good agreement with the experimental results for both wheels.

Keywords: CFD Analysis, Bike Wheels, Cycling Aerodynamics, Validation, Rotation Modeling, Crosswind Modeling

Abstract in lingua italiana

La resistenza aerodinamica gioca un ruolo importante nelle gare ciclistiche e può determinare la vittoria o la sconfitta. Uno dei principali fattori che contribuiscono alla resistenza aerodinamica complessiva di una bicicletta sono le ruote. Il flusso che si sviluppa attraverso la ruota rotante è complesso e in letteratura non si trova un approccio standard per la simulazione delle singole ruote. L'approccio Sliding Mesh (SM)consente di ottenere un'elevata precisione, ma richiede costi computazionali elevati. Esistono quindi metodi stazionari come la Rotating Wall Boundary Condition (RWBC) o il Moving Reference Frame (MRF) che riducono il tempo di calcolo, ma non è chiaro in che misura la loro applicazione sia sensibile alle impostazioni iniziali.

Questo lavoro si concentra sul confronto di diversi modelli di rotazione applicati alla ruota lenticolare e alla ruota a raggi. In primo luogo, viene eseguito un test di validazione confrontando i risultati della simulazione con una precedente campagna di test in galleria del vento. Poi, i tre metodi standard (RWBC, MRF, SM) vengono confrontati per entrambe le ruote a diversi angoli di imbardata per trovare il modo migliore per calcolare il flusso e le forze. Per entrambe le ruote viene eseguita una simulazione DDES con MRF per verificare la differenza tra un modello di turbolenza stazionario e uno transitorio. Per la ruota a raggi, viene implementato anche un approccio alternativo basato sulla sostituzione della geometria effettiva dei raggi con forze volumetriche derivate dal metodo BET. Con questo metodo, è possibile ottenere una migliore qualità della mesh per evitare la procedura di meshing dei raggi, che può causare skewness. Per tutti i metodi, le soluzioni vengono confrontate qualitativamente e quantitativamente.

I risultati mostrano che l'approccio rotazionale applicato gioca un ruolo importante. In particolare, l'MRF può avere un impatto significativo sulle caratteristiche del flusso e sulla previsione della forza, nonostante sia ampiamente utilizzato in letteratura. È stato sviluppato un'applicaizone ottimizzata per l'approccio MRF, che è in linea con i risultati sperimentali per entrambe le ruote.

Parole chiave: Analisi CFD, Ruote Bicicletta, Aerodinamica del Ciclismo, Validazione, Modellazione della Rotazione, Modellazione del Vento Laterale

Contents

1 | Introduction

1.1. Cycling Aerodynamics

Aerodynamic drag is the greatest obstacle for a cyclist. It accounts for up to 90% of the total resistance when cycling at a speed of 40 km/h on flat terrain [7, 14]. This air resistance is primarily caused by the cyclist's body, which contributes 60% to 82% of the total resistance, depending on the position on the bicycle [7, 9], while the remaining air resistance is generated by the bicycle. Although aerodynamic drag is only a small part of total drag, optimizing the aerodynamic design of the bicycle is critical to improving the performance of elite cyclists. After all, races can be won or lost by a few seconds or fractions of a second. Greg Lemond, for example, won the 1989 Tour de France by just 8 seconds after beating Laurent Fignon by 58 seconds in the 24.5km individual time trial. Kristina Vogel won the gold medal in the track cycling sprint at the Rio 2016 Olympic Games by a margin of just 0.016 and 0.004 seconds over Becky James in two races of 200 m length with a flying start.

In addition, Filippo Ganna set a new hour record last year thanks to an optimized time-trial bike and accessories such as helmets and shoes which were developed after hours of wind tunnel testing, CFD simulations, and new manufacturing processes. In particular, the hour record and all other cycling disciplines that take place in the velodrome, where there are no altitude differences and no crosswinds, benefit from improving aerodynamics, because the main force that the cyclist has to overcome is basically air resistance. In fact, every detail can make a difference. All companies and teams invest resources every year to achieve the so-called "marginal gains" and improve the performance of their bikes, their accessories, and their athletes.

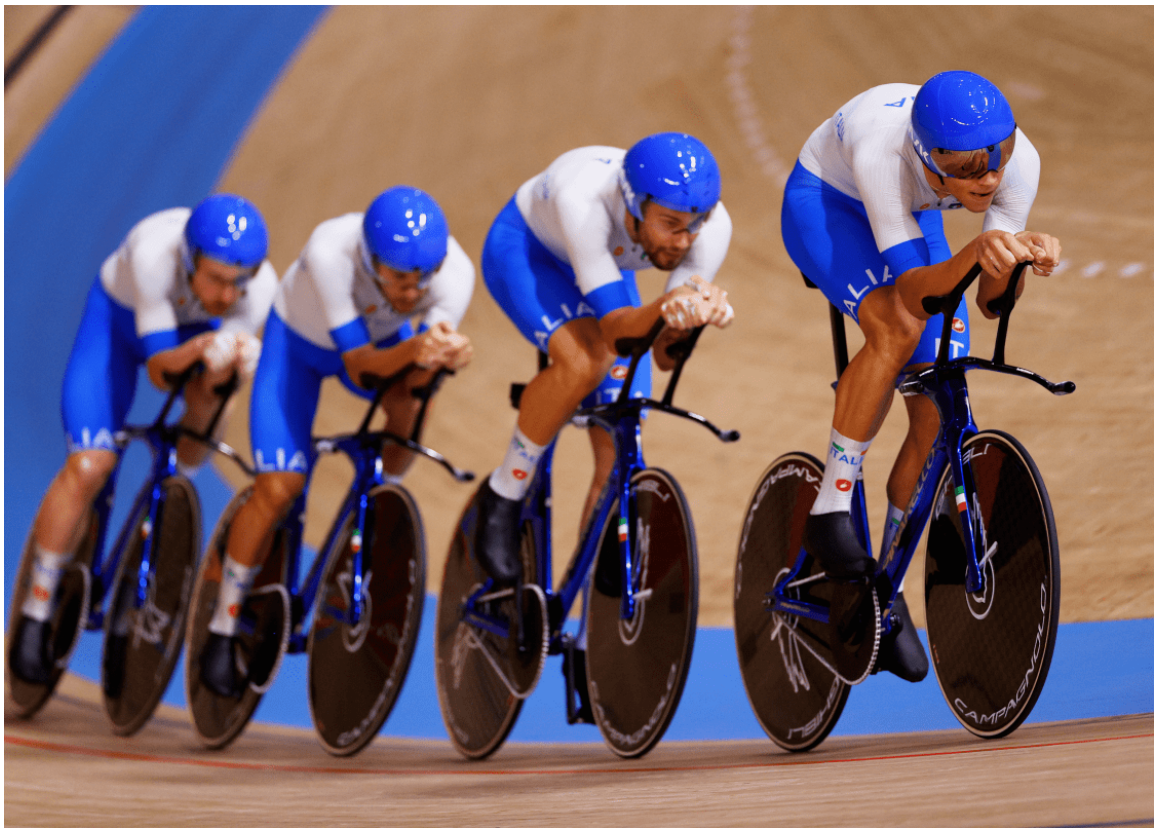

Figure 1.1: After 61 years, the Italian team won Gold in the men's team pursuit, breaking their own world record[2].

In consequence, aerodynamic optimization can be the result of:

- Wind Tunnel tests (WT)
- Computational Fluid Dynamics simulations (CFD)
- Field tests which can take place indoors or outdoors [9].

All tests have advantages and disadvantages. For example, wind tunnel tests have the advantage that they can be carried out in a controlled location. However, the ground is not always in motion, indeed, only some wind tunnels offer the possibility to test with the moving ground. Only in some cases, the effects of the boundary layer are negligible, while they have to be taken into account when most of the tested parts are inside the boundary layer generated by the floor. Another advantage is the possibility to test the effects of the crosswind, even if in the real scenario only the lateral component is characterized by the boundary layer due to friction with the ground. The test campaigns in the wind tunnel, which focus on optimizing the crosswind, are simulated by specifying the relative speed of the wind component with respect to the object while the object is

rotated at the appropriate angle of attack. The relative wind speed under real conditions is the combination of the crosswind and the cyclist's speed. The boundary layer of the crosswind should be reproduced in the wind tunnel, but combining a flow with a boundary layer with another flow without a boundary layer is not possible. The second way to improve aerodynamic performance is through Computational Fluid Dynamics (CFD) simulations. In this case, the test takes place virtually. Computational Fluid Dynamics (CFD) is a highly effective tool for obtaining an approximate solution to the Navier-Stokes equation, which describes the behavior of fluids in space and time. By applying the basic principles of conservation of mass, energy, and momentum, CFD enables the analysis of flow phenomena. In the simulations of CFD simulations, a discretized spatial domain, commonly referred to as a mesh, is used to solve the flow field, resulting in either transient or steady-state solutions. Recent advances in meshing techniques, coupled with improved computational capabilities and improved enhanced turbulence modeling, have broadened the practical applicability of CFD. Consequently, CFD has proven to be a valuable tool for studying viscous flows around complex three-dimensional structures, such as a cyclist [8]. Simulations from CFD offer numerous advantages, including visualization of flow fields, evaluation of forces acting on individual components of the cyclist, the ability to distinguish between pressure and viscous drag, and the ability to compare different configurations of the cyclist configurations, ultimately leading to cost savings.

Last but not least, the real field tests use a power meter on the pedals to compare the real actual power during the ride, especially in the indoor test where the wind and the gradient are constant. In this case, the disadvantage is the repeatability of the tests, which depends on the sensitivity of the rider to stay in the same position during each lap, but it assures ensures that at least the improvement of the riding position is comfortable for the rider during the performance [11].

In addition, specific mathematical models have been developed to evaluate the effects of drag reduction on race times [27, 32]. For example, Martin et al. [26] found that a 2% reduction in the combined air resistance area of the cyclist and bicycle would result in time savings of 0.030 s, 0.120 s, and 0.314 s, respectively, for three different cyclists in a 250 m, 500 m and 1000 m track race. This highlights the significant impact that bicycle aerodynamics can have on the performance and outcome of bicycle races. The most important elements of the bicycle to reduce drag are the frame, wheels, and handlebars.

1.2. Wheel Aerodynamics and Simulations

According to Greenwell et al [15], the wheels alone can account for 10% of the total resistance. As a result, great efforts have been made to improve the aerodynamics of wheels, leading to a variety of options from different manufacturers. In the 2023 Tour de France, 18 cycling teams will use wheels from 14 different manufacturers [29], each offering multiple wheel types. This diversity necessitates the use of established methods to accurately compare the aerodynamics of different wheels.

The evaluation of the aerodynamic performance of cycling wheels therefore usually involves wind tunnel testing (WT) tests, computational fluid dynamics simulations (CFD), and track testing and requires a specific focus. In wind tunnel tests, the wheel is in the testing room while the wind blows on it. Then the wheel starts moving thanks to a belt. It can also rotate around itself to simulate crosswind conditions. In addition, some track tests can be performed carried out to test the wheels (in this case with cyclists and bikes) in a real scenario.

The first cycling wheels chosen for their aerodynamic performance were the disc wheels used by Francesco Moser for his world hour record in 1984 [28] and then at the Olympic Games in 1984. In the tests at that time, the wheels were still in the wind tunnel and it was found that narrower tires, fewer spokes, aerodynamic rims, and small wheel diameters could reduce drag. Some other tests were done by rolling the wheel off a ramp and measuring the deceleration at the end, which is a function of drag, rotational torque, and rolling resistance [23].

The first available tests conducted in a wind tunnel were performed by Kyle [20, 23]. In this study, about 30 wheels were considered and the total drag was given as the sum of the translational drag and the equivalent drag calculated from the rotational torque measurements. In most wind tunnel tests, however, the rotational moment is not evaluated, while the measurement is limited to drag and lateral force. But even the results of measuring drag force alone for the same type of wheel show discrepancies between different studies. For example, Godo has pointed out [13] that the same wheels in the literature have two different measured drag forces and the difference in values is more than 15%. Both tests agreed on the fact that for aerodynamically optimized wheels the axial resistance decreases with increasing yaw angle, while other wheels show an opposite trend.

In recent years, it is common to focus on isolated wheels when studying the aerodynamic performance of bicycle wheels, i.e. without a frame but with a slender support structure in WT tests or the possible presence of a flat surface, roller, or rolling belt nearby to represent

the ground. The aim of these tests is to reduce the aerodynamic drag of the whole system, including the bike and the rider. Still, when the wheels are tested together with the rest of the bike, the results may depend on the bike and the rider, making comparison difficult. Most previous studies of bicycle wheel aerodynamics have been conducted for isolated wheels. However, Crane and Morton pointed out that testing protocols can vary widely from manufacturer to manufacturer and from researcher to researcher, which can lead to large discrepancies in reported drag coefficients. Some results from bicycle manufacturers have not been scientifically processed and verified, so they should be taken with a grain of salt. Discrepancies in aerodynamic drag can also be caused by different test conditions, e.g. different wind tunnels, tires, wheel types, and supports [21, 22].

The lack of a standardized test methodology in wind tunnel experiments for bicycle wheels can also be observed in the simulations of CFD, as shown by the wide range of calculation settings in different publications. Malizia et al. investigated the effects of three calculation parameters on the calculated forces and moments: spatial discretization, wheel rotation modeling, and turbulence modeling, but only used the steady-state model [23]. In this study, an isolated wheel was used without considering the presence of the ground, similar to the wind tunnel experiments of Tew and Sayers[35]. Each of these parameters was found to have a significant effect on the results, leading to the establishment of guidelines for future CFD simulations. However, this study did not consider the effects of soil, some other rotational models, and transient simulations on the resulting forces and moments.

The discrepancy found in the aerodynamic drag between different wind tunnel results for the same wheel is also present in the CFD simulations. In the papers [3, 12, 13, 30] the drag coefficient results for the Zipp 404 spoked wheel ranged from 0.017 to 0.051, while the value calculated by CFD was 0.03. This illustrates the difficulty of reproducing results not only between WT tests but also between WT tests and CFD simulations. Various CFD studies on the aerodynamics of the wheel are presented in the literature, but in previous works, it is difficult to find a systematic analysis of the dependence on computational parameters. Only this work [23] investigated the dependence on the grid resolution, the surface resolution, the turbulence model, and the rotational model. However, the rotation model was investigated only in the Moving Reference Frame, while in CFD there are different ways to consider the rotation within the domain.

In all previous works, there is a wider range of computational parameters, starting from a grid of order 1M [3] up to 16M [12], different ways to simulate the rotation of RWBC, MRF, and SM, and turbulence models such as $k-\omega$ and $k-\varepsilon$. A few studies also used DDES [12]. The widespread use of RANS in bicycle aerodynamics is consistent with the choice in many other areas of wind engineering and industrial aerodynamics. Also, the

influence of the y^+ has not been studied in depth and previous work includes values from 30 to 70, the assumption of wall functions, and only a few papers report the cell height of the first cell [12, 13, 23].

1.3. Objectives

The aim of this thesis work is to extend the existing literature on numerical experiments for cycling aerodynamics. Previous studies have mainly used steady-state solvers (RANS) due to time and cost constraints. In this work a computational sensitivity with respect to rotation modeling parameters has been investigated, firstly the focus has mainly been on mesh refinement, then on the effects of different rotation approaches. The moving reference model is also validated by comparing the simulated results with a previous wind tunnel campaign.

To further improve the understanding of rotation models, this study aims to investigate and compare different rotation approaches, starting with the lenticular wheel and then moving to a traditional spoked wheel. In the study, the flow is considered at different yaw angles and the rotation is modeled not only with the stationary solver with rotating wall boundary conditions, and the moving reference model but also with the computationally intensive sliding mesh approach, which may not be readily accessible in an industrial context.

In addition, a novel application of the rotor disk model is briefly presented to simulate the flow around the spokes and mitigate potential instability problems caused by the meshing of the spokes during the simulations. Furthermore, the thesis incorporates Detached Eddy Simulation (DDES) to compare this turbulence modeling approach, which has become increasingly practical with the increase in available computing power.

The structure of this work is as follows:

Section 2 provides a description of the governing equations used to model the flow, focusing on the formulation employed in this study.

Section 3 presents the numerical setup, emphasizing the rotational models studied.

Section 4 validates the model based on the improved results obtained.

Section 5 is dedicated to the presentation and discussion of the results and consists of two subsections: the first focuses on the analysis of the lenticular wheel, including a comparison with the results of aeroCloud, while the second subsection presents the results for the spokes wheel and introduces the rotor disk model.

Finally, Section 6 concludes the thesis and suggests future development directions in the field.

2 | Governing Equations

In this chapter is described a brief introduction to the flow governing equations derived depending on the following different cases. The software employed for this work is the latest version available (V10) of OpenFOAM. The free availability, the possibility to look inside and eventually modify the source code, and the opportunity to run the simulations are the reasons for the choice of this software.

2.1. Mathematical Governing Equation

The Navier-Stokes Equations are a set of equations that describe the motion of fluids and the forces acting on them. They are derived from the basic laws of physics, such as the conservation of mass, momentum, and energy, and are used to model fluid flow in various engineering and scientific applications. This set of equations is not analytically solvable, thus usually they are solved through different methods of numerical computations. The equations are written in vector form and take into account the effects of fluid viscosity and pressure.

The Navier-Stokes Equations can be written as:

$$\begin{cases} \frac{\partial \rho}{\partial t} + \nabla(\rho \mathbf{u}) = 0 \\ \frac{\partial(\rho \mathbf{u})}{\partial t} + \nabla \cdot (\rho \mathbf{u} \times \mathbf{u}) = \nabla \sigma + \rho \mathbf{b} \end{cases} \tag{2.1}$$

where:

ρ is the fluid density

$\mathbf{u}$ is the fluid velocity vector

σ is the stress tensor

$\mathbf{b}$ is a external forces vector

∇ is the gradient operator

The first equation represents the conservation of mass, which states that the rate of change of fluid density in a given region is equal to the rate of fluid flowing into or out of that region.

The second equation represents the conservation of momentum, which states that the rate of change of fluid momentum in a given region is equal to the sum of all the forces acting on the fluid in that region. This includes the pressure gradient, viscous forces, and external forces such as gravity. Another important propriety of the fluid is that the air is a Newtonian fluid, thus a relationship between the stress tensor to the gradient of the velocity field is obtained through the dynamic viscosity ($\tau = \mu \frac{\partial u}{\partial t}$) . All these hypotheses are the basis to write the Navier-Stokes equations 2.5 [33]. Thus the stress tensor can be written as:

$$\sigma = -(p + \frac{2}{3}\mu\nabla\mathbf{u})\mathbf{I} + \mu(\mathbf{u} + (\nabla\mathbf{u})^T) = -p\mathbf{I} + \tau \tag{2.2}$$

where:

p is the fluid pressure

μ is the dynamic viscosity

τ is the viscous stress tensor.

Hence, the *momentun equation* can be rewritten as:

$$\frac{\partial(\rho\mathbf{u})}{\partial t} + \nabla \cdot (\rho\mathbf{u} \times \mathbf{u}) = -\nabla p + \nabla\tau + \rho\mathbf{b} \tag{2.3}$$

Furthermore, there is also a third equation which represents the conservation of energy. This equation states that the rate of change of fluid energy in a given region is equal to the rate at which energy is being added to or removed from the fluid in that region. This includes the work done by the fluid on its surroundings, the heat transfer due to conduction, and the energy input due to external forces:

$$\frac{\partial(\rho e)}{\partial t} + \frac{\partial(\rho K)}{\partial t} = -\nabla \cdot \mathbf{q} + \rho r + \nabla \cdot (\sigma \cdot \mathbf{u}) + \rho\mathbf{b} \cdot \mathbf{u} \tag{2.4}$$

where:

e is the internal energy per unit mass

K is the kinetic energy

r is the thermal heat source

$\mathbf{q}$ is the thermal flux.

The Navier-Stokes Equations are highly complex and nonlinear, and finding a solution for a given fluid flow problem can be challenging. However, these equations provide a powerful tool for understanding and predicting fluid behavior, and are widely used in various fields such as aerodynamics, hydrodynamics, and heat transfer.

Moreover, a significant hypothesis can be assumed which simplifies the equations for the problem under investigation. Indeed the flow is characterized by low pressure, temperature, and speed far below the Mach number. Due to these assumptions, the air in this fluid-dynamic problem is described as an in-compressible, low-viscosity, and single-phase fluid. Since an incompressible fluid is assumed, the state equation is $\rho = \text{const.}$ and in this case, the energy equation is waived as there is no heat transfer. The mass and momentum equations for this problem are the following:

$$\begin{cases} \nabla \cdot \mathbf{u} = 0 \\ \frac{\partial \mathbf{u}}{\partial t} + (\mathbf{u} \cdot \nabla)\mathbf{u} = -\nabla \frac{p}{\rho} + \nu \nabla^2 \mathbf{u} + \mathbf{b} \end{cases} \tag{2.5}$$

Which are the Navier-Stokes equations for incompressible flow. In particular, the dynamic viscosity μ is assumed constant, dividing it by the density the kinematic viscosity ν is obtained ($\nu = \frac{\mu}{\rho} \simeq 10^{-5}$).

It is important to introduce the two other parameters required to describe the flow. The former is the Reynolds number which refers to the ratio between inertial and viscous forces in fluids. In the case of a number below 2000, the flow can be described as laminar; if it exceeds 10000, the flow will likely be turbulent. The latter is turbulence intensity, a measure of wind speed fluctuations, which is the standard deviation of fluctuating wind velocity divided by mean wind speed: if this index is below 1% the turbulence is low, when it reaches intensities above 5% means high turbulence.

$$\begin{cases} Re = \frac{\rho U L}{\mu} \\ I = \frac{\mathbf{u}_{RMS}}{U_{in}} \end{cases} \tag{2.6}$$

Where U is the local mean stream-wise flow velocity and u_{RMS} is the local root-mean-square (RMS) of the turbulent stream-wise velocity fluctuations [4].

2.2. RANS Equations

As the flow speeds up, depending on the fluid characteristics and on the geometry, the laminar flow becomes turbulent and eddy structures are observed at different scales [5]. These structures create a virtuous cycle where the bigger ones absorb energy and propagate it to the smaller ones where the energy is dissipated because of viscous friction.

In the presence of turbulence, the Navier-Stokes equation remains valid, however, the inertial terms cannot be simplified, prohibiting the construction of an analytical solution. Numerical discretization (Direct numerical discretization, DNS) can be used, but it is computationally expensive and can be avoided for this report. In this case, the Reynolds averaged equations (RANS) model is used since it is capable of capturing the key process characteristics.

The RANS works because they relate to the average proprieties and they take into account only the small fluctuations. in this way, the mean parameter over time is estimated even if the turbulence flow is not solved entirely. Every component, indeed, can be expressed as:

$$\mathbf{u}(\mathbf{x},t) = \overline{\mathbf{u}}(\mathbf{x},t) + \mathbf{u'}(\mathbf{x},t) \tag{2.7}$$

The equations obtained for an incompressible fluid can be rewritten in indexes notation:

The continuity equation:

$$\frac{\partial u_i}{\partial x_i} = 0 \tag{2.8}$$

The momentum equation:

$$\frac{\partial u_i}{\partial t} + u_j \frac{\partial u_i}{\partial x_j} = -\frac{1}{\rho}\frac{\partial p}{\partial x_i} + \nu \frac{\partial^2 u_i}{\partial x_j \partial x_j} - \frac{\partial \overline{u_j' u_i'}}{\partial x_i} + f_i \tag{2.9}$$

where u_i is the velocity vector in the ith direction, p is the pressure, ρ is the fluid density, ν is the kinematic viscosity, and f_i is the body force in the i_{th} direction.

From these equations, it is possible to see that there are four equations (three from 2.9 and one from 2.8) with ten unknowns (pressure, velocity in three directions, and six from the term $\partial\overline{u_j' u_i'}$). To make the number of equations and unknowns equal there are different ways to proceed. One of these is based on the *turbolent − viscosity hypothesis*. In this

case, the Reynolds stress tensor can be decomposed in an isotropic and a deviatoric part:

$$\partial\overline{u_j'u_i'} = \frac{2}{3}k\delta_{ij} + a_{ij} \tag{2.10}$$

where k is the Turbulent Kinetic Energy (TKE), defined as $k \equiv \frac{1}{2}\partial\overline{u_j'u_i'}$, is isotropic and a_{ij} is the deviatoric part. This hypothesis estimates the deviatoric part as proportional to the mean rate of strain: $\overline{S_{ij}} = \frac{1}{2}(\frac{\partial\overline{u_i}}{\partial x_j} + \frac{\partial\overline{u_j}}{\partial x_i})$ where the proportionality constant is called *turbolent viscosity* (ν_{turb}), thus:

$$\partial\overline{u_j'u_i'} = \frac{2}{3}k\delta_{ij} - 2\nu_{turb}\overline{S_{ij}} = \frac{2}{3}k\delta_{ij} - \nu_{turb}(\frac{\partial\overline{u_i}}{\partial x_j} + \frac{\partial\overline{u_j}}{\partial x_i}) \tag{2.11}$$

Hence the governing equations become:

$$\begin{cases} \nabla\cdot\mathbf{u} = 0 \\ \frac{\partial\mathbf{u}}{\partial t} + \nabla\cdot(\mathbf{u}\times\mathbf{u}) = -\nabla p + (\nu+\nu_{turb})\nabla^2\mathbf{u} + \rho\mathbf{g} \end{cases} \tag{2.12}$$

Comparing the RANS with the Navier-Stokes equations, it must be noticed an extra dissipative term, called Reynolds' turbulent stress tensor. This component needs a high computational resource to be estimated, but if the turbulence is enough isotropic, like in this case study, it can be seen as an additional turbulent viscosity. This viscosity has the propriety to be flow dependent and not fluid-dependent, this means that needs to be calculated respecting the mean characteristic of the flow.

To determine the turbulence viscosity, various models ranging from zero-equation to two-equation models are utilized. For external incompressible aerodynamics, two-equation models are typically preferred due to their ability to provide reliable results consistent with experimental data while remaining computationally feasible. Indeed, the two-equation model adopted in this work it is described in the following section.

2.3. DDES Equations

Large Eddy Simulation (LES) is a step forward in turbulence modeling since with this approach it is possible to compute the large eddies of the flow while the smallest ones are modeled. In this way, the computation effort can be reduced by ignoring the smallest length scales. To do so, a low pass filter is implemented and introduced into the Navier-

Stokes equations.

Starting from the governing equations used by the LES model which are called filtered incompressible Navier-Stokes equations (FNS) and they are:

$$\begin{cases} \nabla \cdot \tilde{\mathbf{u}} = 0 \\ \frac{\partial \tilde{\mathbf{u}}}{\partial t} + \nabla \cdot (\tilde{\mathbf{u}} \times \tilde{\mathbf{u}}) = \frac{-\nabla \tilde{p}}{\rho} + \nu \nabla^2 \tilde{\mathbf{u}} - \frac{1}{\rho} \nabla \cdot \tau^{SGS} \end{cases} \tag{2.13}$$

Where $\sim$ represents filtered quantity. As it can be seen, the FNS are very similar to the starting equations and the RANS equations. The main difference is that all variables are filtered in space and we need to somehow model the sub-grid scale stress tensor τ^{SGS}. To derive the compressible LES equations, we proceed in a similar way, but we use mass-weighted averaging.

Considering a general field $\phi(\mathbf{x}, t)$, the LES filter is defined as:

$$\overline{\phi(\mathbf{x}, t)} = \int_{-\infty}^{\infty} \int_{-\infty}^{\infty} \phi(\mathbf{r}, \tau) G(\mathbf{x} - \mathbf{r}, t - \tau) d\tau d\mathbf{r} \tag{2.14}$$

where $\mathbf{G}$ is the filter convolution kernel, which has a cutoff length scale Δ and a cutoff time scale τ_c.

This filter can be seen as a time and spatial averaging of the numerical solution. Small scales are eliminated and any field ϕ may be split into a filtered and subfiltered component ($\phi = \tilde{\phi} + \phi'$). In this case, the filtered quantity is the resolved scales (grid scales), whereas the sub-grid scales remain unresolved.

However, the removed information about small eddies is not negligible and its effect on the flow must be modeled through sub-grid scale models. LES simulations require modeling of part of the inertial subrange and into the beginning of the dissipation scales. The amount of required modeling is set by the grid resolution but is unlikely that the grid will scale worse than Re_T^2.
Even if this requirement appears to be high, LES simulations are starting to become affordable in modern supercomputers. In this work, a DES (Detached Eddy Calculations) model is applied to compare the efficiency of RANS turbulence model. Indeed DES applied LES model where the grid is fine enough to calculate the turbulence and it applied the RANS model on the other sections of the grid. Detached-Eddy Simulation (DES) is a hybrid technique first proposed by Spalart et al. [31] for the prediction of turbulent flows at high Reynolds numbers [37]. The aim of DES is to combine the most favorable

aspects of RANS and LES techniques, so be capable to resolute the time-dependent, three-dimensional large eddies in the core of the flow, while RANS models the attached boundary layers. In this work, the improvement of DES is used and it is the SST DDES that used several blending and shielding functions which are computed starting from the $k-\omega$ model which is described in the following paragraph. This model allows us to study with a reasonable amount of computational time the unsteadiness of the bigger vortex created by the turbulence [16].

2.4. Turbulence Model

The k-epsilon model is a popular turbulence model used in Computational Fluid Dynamics (CFD) simulations. It is a two-equation model that solves two additional transport equations for turbulent kinetic energy (k) and the rate of dissipation of turbulent kinetic energy (ε). This approach is able to solve the problem even with a coarse mesh. In this case, the turbulence viscosity can be expressed as $\nu_{turb} = C_\mu \frac{k^2}{\varepsilon}$. The governing equations, to be solved in parallel with the RANS, are the following:

$$\begin{cases} \frac{\partial k}{\partial t} + \overline{\mathbf{u}} \cdot \nabla k = \nabla \cdot [(\nu + \nu_{turb}\sigma_k)\nabla k] + P_k - \varepsilon \\ \frac{\partial \varepsilon}{\partial t} + \overline{\mathbf{u}} \cdot \nabla \varepsilon = \nabla \cdot [(\nu + \nu_{turb}\sigma_\varepsilon)\nabla \varepsilon] + C_{\varepsilon_1} \frac{P_k \varepsilon}{k} - C_{\varepsilon_2} \frac{\varepsilon^2}{k} \\ \text{where } \; P_k = \nu_{turb} \nabla \overline{\mathbf{u}} : (\overline{\mathbf{u}} + \overline{\mathbf{u}}^T - \frac{2}{3} k \mathbf{I}) - \frac{2}{3}\varepsilon \end{cases} \tag{2.15}$$

The five constants, determined experimentally, are:
$C_\mu = 0.09$, $C_{\varepsilon_1} = 1.44$, $C_{\varepsilon_2} = 1.92$, $\sigma_k = 1.0$, $\sigma_\varepsilon = 1.3$, and $\nu_{turb} = C_\mu k^2/\varepsilon$

The k equation derives directly from Navier-Stokes equations but the flux is modeled according to the gradient-diffusion hypothesis [34] and reads the same equations used for the k-ε turbulence model. The problem with the previous model is that performs quite well only in free-stream conditions but not in the near-wall region.

Thus, an equation for the *specific turbolence kinetic energy dissipation rate* ω can be added:

$$\frac{\partial \omega}{\partial t} + \overline{\mathbf{u}} \cdot \nabla \omega = \nabla \cdot [(\nu + \nu_{turb}\sigma_\omega)\nabla \omega] + \alpha P_\omega - \beta \omega^2 \tag{2.16}$$

With $\alpha = 5/9$, $\beta = 0.075$ and $\sigma_{omega} = 0.5$. The first equation in 2.15 and the equation

2.16 form the k-ω turbulence model. Hence, it is possible to insert the relation:

$$\omega = \frac{\varepsilon}{k\beta*} \tag{2.17}$$

in the second equation in 2.15 and derived a modified equation for ω:

$$\frac{\partial\omega}{\partial t} + \overline{\mathbf{u}} \cdot \nabla\omega = \nabla \cdot [(\nu + \nu_{turb}\sigma_\omega)\nabla\omega] + \alpha P_\omega - \beta\omega^2 + 2\sigma_{\omega^2}\frac{1}{\omega}\nabla k\nabla\omega \tag{2.18}$$

The last expression is actually the ε equation and differs from the last by a single term. By using a proper blending function on the last term of the equation is possible to switch between the k-ω and the k-ε model according to the wall proximity. Particularly the k-ε model is used far from any surfaces while k-ω is adopted when a wall is approached.

In the end, the k-ω *Shear Stress Trasnport SST* is the turbulence model adopted for this work.

y^+ Analysis

Because near the wall the viscous phenomena become preponderant, it is difficult to analyze it without an excellent resolution grid [25]. Hence a wall function is introduced to study the behavior of the flow near the wall in order to improve the precision because the distribution close to the wall is similar for almost turbulent flow.

The wall function works with two non-dimensional values: the non-dimensional flow velocity u^+ and the distance from the wall y^+. Thanks to the value of y^+, the model k-ε is able to compute the profile velocity. In the sub-layer where the wall functions can be applied, three different zones can be distinguished.

- Linear sub-layer: where $y^+ < 5$, the correlation between non-dimensional velocity and distance is linear: $u^+ = y^+$. This correlation is given because the viscous effect is preponderant with respect to turbulence ones.
- Outer layer: where $30 < y^+ < 300$, the velocity can be stated as: $u^+ = \frac{logEy^+}{\kappa}$. This logarithmic correlation covers the interaction between viscous and turbulence forces.
- Buffer layer: $5 < y^+ < 30$, no mathematical correlations are present, but it is the zone that links the two different functions. The value where the intercept of the function is $y^+ = 11$.

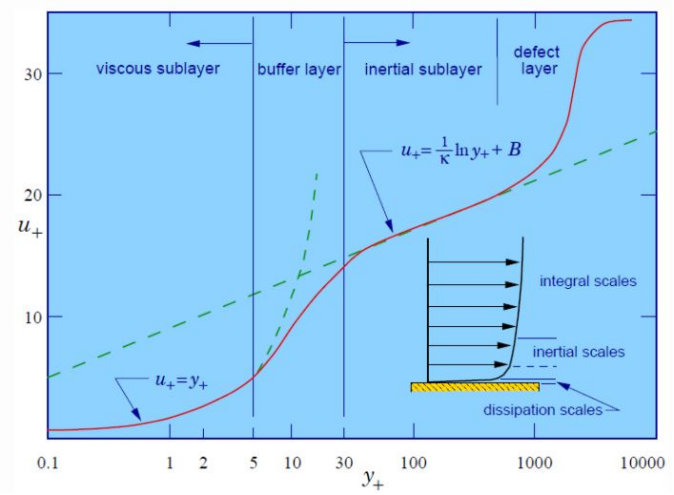

Figure 2.1: Velocity profiles in turbulent wall flow [1].

The two values are computed as:

$$\begin{cases} y^+ = y\frac{C_\mu^{\frac{1}{4}}\sqrt{\kappa}}{\mu} \\ v^+ = y\frac{u}{C_\mu^{\frac{1}{4}}\sqrt{\kappa}} \end{cases} \tag{2.19}$$

The empirical constants assume the value of:

$\kappa = 0.4$, $E = 9.0$.
The velocity profile is depicted in Fig. 2.1 [1].

In this work, the boundary layer is solved when $y+$ is below 6, hence when the mesh is enough fine to reach this requirements, while for unsteady models, due to the higher computational cost, the wall functions are applied near the wall to limit the number of cells and make the simulation computational affordable for the objective of this thesis.

Q criterion

The Q criterion is one of the possible ways to define a vortex and is good indicator of turbulent flow structures. It uses the second invariant of the velocity gradient tensor, which must be higher than zero:

$$Q = \frac{1}{2}[tr(\nabla \mathbf{u}))^2 - tr(\nabla \mathbf{u} \cdot \nabla \mathbf{u})] \tag{2.20}$$

where $\mathbf{u}$ is the velocity vector. In this way, the Q criterion defines a connected fluid region. An additional condition for the vortex definition is given by the the pressure, which must

be lower than the asymptotic value. From the equation can be seen that Q represents the local balance between the shear strain rate and the vorticity magnitude, and defines a vortex as the area where the vorticity magnitude is higher respect to the magnitude of the shear strain rate.

2.5. Rotating Models

Accurately modeling wheels is paramount to achieve realistic simulations of flows and aerodynamic forces. It plays a crucial role in determining the accuracy of the results in terms of force prediction generated by the entire vehicle and the simulated flows around the wheels. Furthermore, minute details can significantly modify vortex structures, wake shapes, and intensity.

Numerical simulations of rotating wheels pose significant challenges in modeling rotation and deformation. Although some methods are more suitable than others, each has its limitations.

The presence of rotation is a vital aspect of wheel aerodynamics, as it completely alters the flow. Numerical modeling of rotation in CFD simulations involves different approaches. The choice of rotation model is critical in obtaining high-quality results while optimizing computational resources. The three primary numerical approaches to describe models with rotational parts are Rotating Wall Boundary Condition (RWBC), Moving Reference Frame (MRF), and Sliding Mesh (SM). Moreover, rotor Disk method is introduced as a new method to simulate the spokes of the wheel.

2.5.1. Rotating Wall Boundary Condition

The Rotating Wall boundary Condition is a boundary condition that can be applied to any patch that comprises a geometry. The user can set the patches on which a velocity vector is imposed, as well as the center of rotation, the angular velocity, and the rotational axis.

During the simulation, the velocity vector is computed for each face cell on which the boundary condition is applied. This is done using the following formula:

$$\vec{u_p} = -\omega(\vec{r_f} - \vec{r_0}) \times \frac{\vec{\Omega}}{|\vec{\Omega}|} \tag{2.21}$$

Here, ω represents the angular velocity, $\vec{r_f}$ represents the center of the cell face, $\vec{r_0}$ represents the center of rotation, and $\vec{\Omega}$ represents the rotational axis. After calculating the rotational wall velocity, the normal of the cell faces ($\vec{n}$) is determined. This normal is then used to remove the normal component of the velocity by projecting the velocity onto the normal direction of the face. If the boundary condition were to keep the component normal to the surface, it would represent a flow through the surface, i.e., an inlet or outlet boundary condition. This is not possible, so the rotational wall velocity is corrected as follows:

$$\vec{u}_{p,new} = \vec{u_p} - \vec{n}(\vec{n} \cdot \vec{u_p}) \tag{2.22}$$

This step confirms that a rotating wall is not suitable for cases where the desired velocity component is largely normal to the surface. If the normal of a face is parallel to the rotational wall velocity, it would mean that:

$$\vec{n} \cdot \vec{u} = \vec{u_p} \tag{2.23}$$

Hence,

$$\vec{u}_{p,new} = 0 \tag{2.24}$$

When it comes to simulating wheels, this is not a negligible limitation. The rim geometry is crucial in wheel simulations but is largely characterized by surfaces that are largely normal to the velocity vector. While for a rotating cylinder, or in this case a disc-wheel (lenticular) this boundary condition should perfectly simulate the rotation.

2.5.2. Moving Reference Frame

The Moving Reference Frame (MRF), which is also known as the Multiple Reference Frame or Rotating Reference Frame method, involves placing cells in a rotating reference frame. This method overcomes the issue of resolving the velocity component normal to the surface, which was a limitation of the Rotating Wall Boundary Condition. Specifically, for a surface whose normal is parallel to the rotational wall velocity, the corrected velocity value will be zero in the rotating reference frame but will be non-zero in a stationary reference frame.

This approach is achieved by introducing a change of variables to the Navier-Stokes equations. The modified incompressible equations are given by:

$$\frac{\partial \vec{u}_R}{\partial t} + \frac{\partial \vec{\Omega}}{\partial t} \times \vec{r} + \nabla \cdot (\vec{u}_R \otimes \vec{u}_I) + \vec{\Omega} \times \vec{u}_I = -\nabla(p/\rho) + \nu \nabla \cdot (\vec{u}_I) \tag{2.25}$$

$$\nabla \cdot \vec{u}_I = 0 \tag{2.26}$$

where I and R denote the inertial and relative reference frames, respectively. The rotational vector is denoted by $\vec{\Omega}$ and $\vec{r}$ is the vector from the origin of rotation to the cell.

One of the limitations of the MRF method is that the results are dependent on the wheel position since the geometry is not actually moved using this method. This can be a significant drawback for the analysis of a three-spoke wheel, for instance. Additionally, it has been shown that the choice of the MRF region can significantly affect the flow. Assuming a steady flow, the time derivative in Equation 2.25 vanishes. If the uniform flow is assumed, which is equivalent to considering an empty region, then $\nabla \vec{u}_I = 0$. Consequently, Equation 2.25 can be simplified to:

$$\vec{\Omega} \times \vec{u}_I = -\nabla(p/\rho) \tag{2.27}$$

Therefore, even if there are no rotating boundaries affecting the flow, a pressure gradient is introduced when $\vec{\Omega} \times \vec{u}_I \neq 0$. A special case where $\nabla p = 0$ is when the flow direction is along the axis of rotation, as is the case for an axial fan. However, for wheels, the axis of rotation is almost orthogonal to the main flow direction.

A simple 2D simulation with an empty MRF circular region illustrates this phenomenon. It is clear that the pressure gradient significantly alters the flow field.

2.5.3. Sliding Mesh

The sliding mesh approach involves physically moving parts of the mesh during every time step, making it the only method presented that achieves actual mesh rotation. Therefore, it is considered the most realistic method for modeling rotating rigid geometries. However, this approach has several drawbacks, including the need for an unsteady simulation when using a rotation mesh, as well as the requirement to update the connectivity between the stationary and rotating regions at each time step. These factors contribute to a

substantial increase in computational cost. Moreover, the current sliding mesh method is not suitable for modeling tires that are in contact with the ground because they lose their circular shape due to the formation of a contact patch and a bulge above it. This deformation eliminates the possibility of using the sliding mesh approach for tires since the tire is no longer radially symmetric.

2.5.4. Moving Reference Frame - grooves

The Moving Reference Frame - grooves (MRFg) approach is a hybrid technique introduced by Hobeika et al. [17] which combines RWBC and MRF to overcome the limitations of RWBC by utilizing MRF in areas where RWBC is not appropriate. While MRF results are significantly influenced by wheel position, for geometries with a high degree of rotational symmetry or repetitive patterns, such as tires, accounting for various tire positions may not be necessary. Therefore, in the MRFg approach, the MRF region is placed in the lateral grooves. In this specific case the MRF is applied on the spokes which show a rotational geometry and repetitive patterns, while the rim is modeled with RWBC.

2.5.5. Rotor Disk Model

The proposed model aims to simulate the grooves of a cycling wheel using the *rotorDisk class* available in OpenFOAM V10. This class allows for cell-based momentum sources to be applied on the velocity field, approximating the mean effects of rotor forces. The rotorDisk method was originally developed by Wahono [36] for simulating helicopter rotor downwash and is commonly used for simulating rotors such as fans and propellers that require a swirl effect in the solution. The basic concept of the rotorDisk method involves replacing the physical geometry with only its effects on the flow by adding reactive aerodynamic forces as a source term in the momentum equation (b_j).

Although it is unconventional to use the rotorDisk method to model the spokes of a cycling wheel, it is intended to achieve time-averaged effects of rotation independent of position, in order to eliminate unrealistic flow features produced by fixed spokes. The rotorDisk model is based on the Blade Element Theory (BET), which was initially developed by William Froude in 1878. This theory involves dividing the blade into a series of sections, calculating the forces and moments acting on each section, and then integrating them to obtain the total forces and moments. In the following section, some of the steps involved in applying BET to obtain the source term will be briefly described.

Blade Element Theory

Blade element theory is a mathematical process originally designed by William Froude (1878), David W. Taylor (1893) and Stefan Drzewiecki to determine the behavior of propellers. It involves breaking a blade down into several small parts and then determining the forces on each of these small blade elements. These forces are then integrated along the entire blade and over one rotor revolution in order to obtain the forces and moments produced by the entire propeller or rotor. The blades are considered as made up of a number of small elements, and the air forces on each element are calculated. The airflow around each element is considered two-dimensional and therefore unaffected by the adjacent parts of the blade. The independence of the blade elements at any given radius with respect to the neighboring elements has been established theoretically and has also been shown to be substantially true for the working sections of the blade by special experiments made for the purpose. It is also assumed that the air passes through the propeller with no radial flow and that there is no blade interference [10].

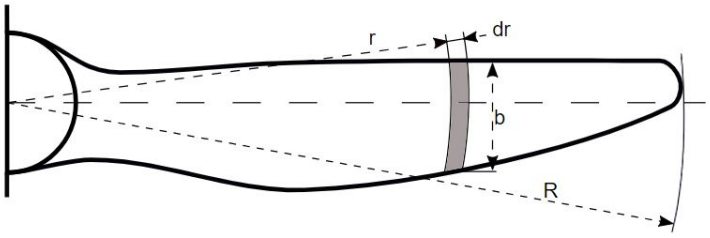

Figure 2.2: Blade Element

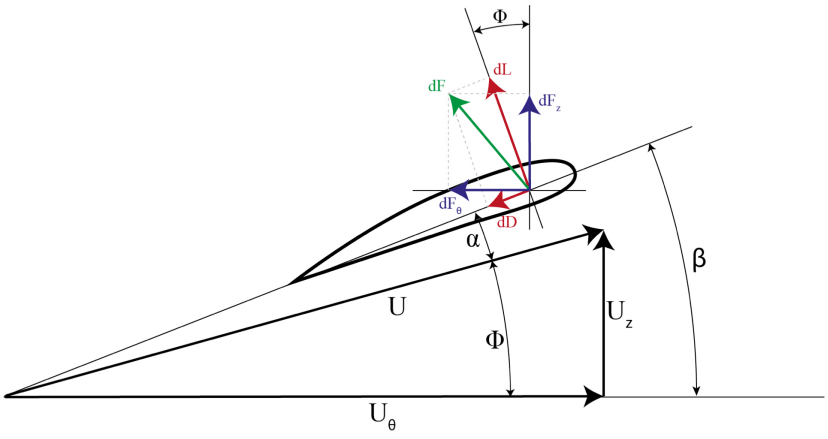

Figure 2.3: Decomposition of the various forces acting on the blade element.

The element method is applied by dividing the aerodynamic forces on the blade: The useful dimensions are shown in Fig.2.3 Considering the element of radius r shown in Fig.2.2, at the infinitesimal length, dr, and width b has a motion along a helical path determined by the horizontal velocity of the plane V and the tangential velocity of the blade element $2\pi rn$. Call the angle between the direction of motion of the element and the plane of rotation ϕ, and the blade angle β. The angle of attack α of the element relative to the air is then

$$\begin{cases} \alpha = \beta - \phi \\ \text{where } \phi = atan(U_z/U_\theta) \end{cases} \tag{2.28}$$

The sectional lift and drag coefficients are provided in pre-defined tables and are interpolated to determine the required values. Based on this, the axial and tangential forces acting on each section are calculated.

$$\begin{cases} f_z = \frac{1}{2}\rho V^2 c(c_L cos(\phi) - c_D sin(\phi)) \\ f_{theta} = \frac{1}{2}\rho V^2 c(c_L sin(\phi) + c_D cos(\phi)) \end{cases} \tag{2.29}$$

In order to account for the decrease in lift caused by tip vortices, a tip factor correction is typically applied to the lift component of each force. Subsequently, the sectional forces that are computed are converted to volume forces using a scaling factor that evenly distributes the force generated by all blades (n_B) over the entire circumference ($2\pi r$).

$$\begin{cases} F_{z,cell} = \frac{f_z(r_{cell}A_{cell})}{2\pi r_{cell}} n_B \\ F_{\theta,cell} = \frac{f_\theta(r_{cell}A_{cell})}{2\pi r_{cell}} n_B \end{cases} \tag{2.30}$$

The source term for the momentum equation is obtained by calculating the distance of the cell centroid from the rotor axis (r_{cell}), and transforming the resulting forces into the Cartesian coordinate system, which is then divided by the cell volume.

$$b_{j,cell} = \frac{F_{j,cell}}{V_{cell}} \tag{2.31}$$

where $j = x, y, z$ are the components of the transformed (Cartesian) force.

3 | Numerical Setup

This chapter presents the method for comparing the different rotation models.

First, a reference case is defined as the starting point for the sensitivity analyses. In the following Sections (3.1, 3.2, 3.3), the computational domain, the geometry and grid, the boundary conditions, the grid criteria and the solvers are presented respectively. In Section 3.4, a systematic study of mesh convergence is carried out to find the best trade-off between mesh and results. Section 3.5 defines and compares the different rotation models, introducing not only RANS simulations but introducing also DDES simulations for one of the cases. In section 3.6 a brief overview of AeroCloud is given to compare the sensitivity of the software.

3.1. Computational geometry

The geometry of the two wheels was inspired by DT Swiss R460, a commercial aluminium wheel, and modified so that there are two types of wheels, one with twenty symmetrical spokes and one lenticular. The spoked wheel consists of the hub, the rim and the spokes, while the tyre plays no role in this study, so no specific analysis is carried out for this component. The lenticular wheel is modelled as a single surface. The geometry of the spokes has a classic cylindrical shape with a diameter of 2 mm. In Fig. 3.1, 3.2, 3.3, 3.4 the final CAD geometry is presented.

Figure 3.1: Lenticular Wheel

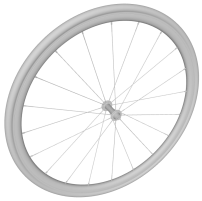

Figure 3.2: Spoked Wheel

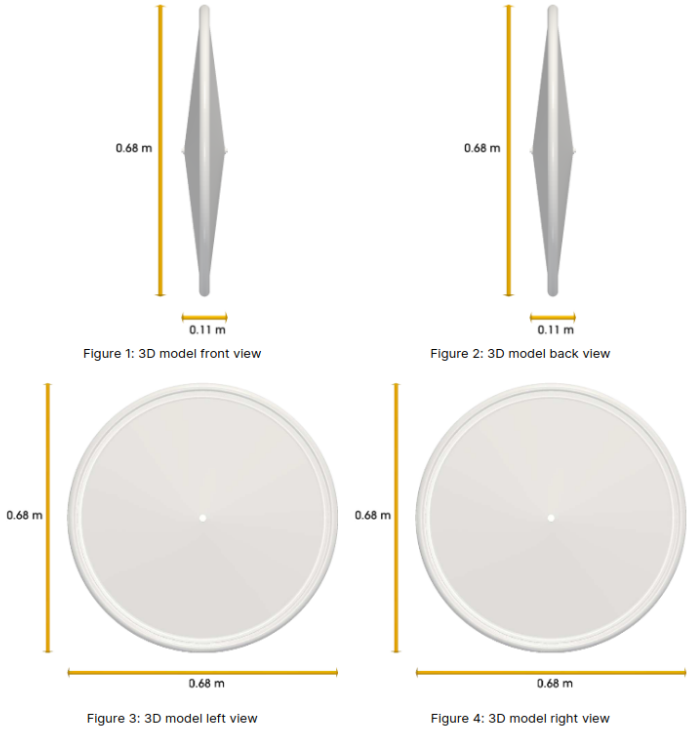

Figure 3.3: Geometry dimensions for the lenticular wheel

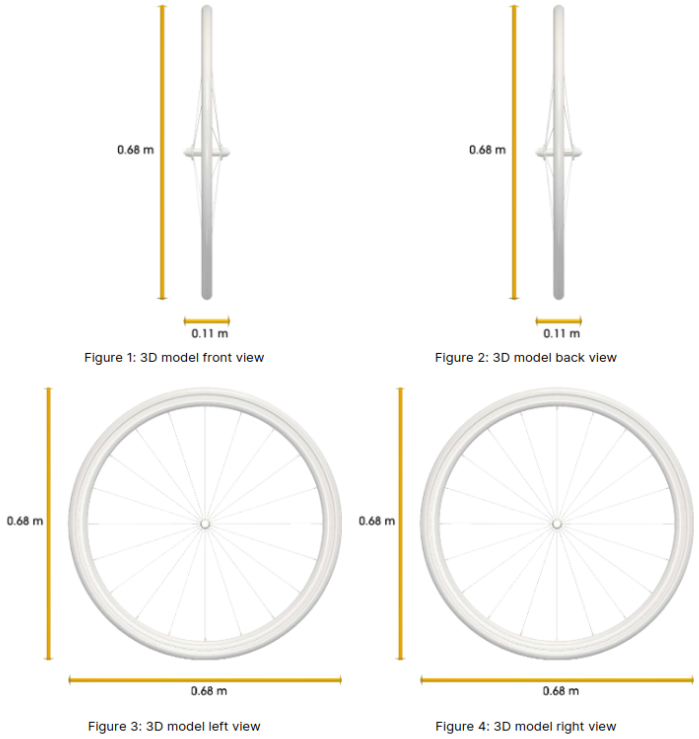

Figure 3.4: Geometry dimensions for the spoked wheel

3.2. Computational domain and grid

The computational domain is shown in Fig. 3.5.
Its dimensions are chosen based on CFD best practice guidelines for outdoor flows in the urban environment [6] and automotive external aerodynamics [18]. The distance of the wheel geometry to the lateral, top, and bottom planes of the domain is 5 ∅, where ∅ is the classic used model for a road bike of 700c x 25c. The upstream and downstream lengths of the domain are 5 ∅ and 10 ∅ respectively. This setup guarantees a Blockage Ratio (BR) below the 1%. In this case, the presence of the ground is neglected because the wheel is rotating in the middle of the computational domain at a sufficient distance from the ground.

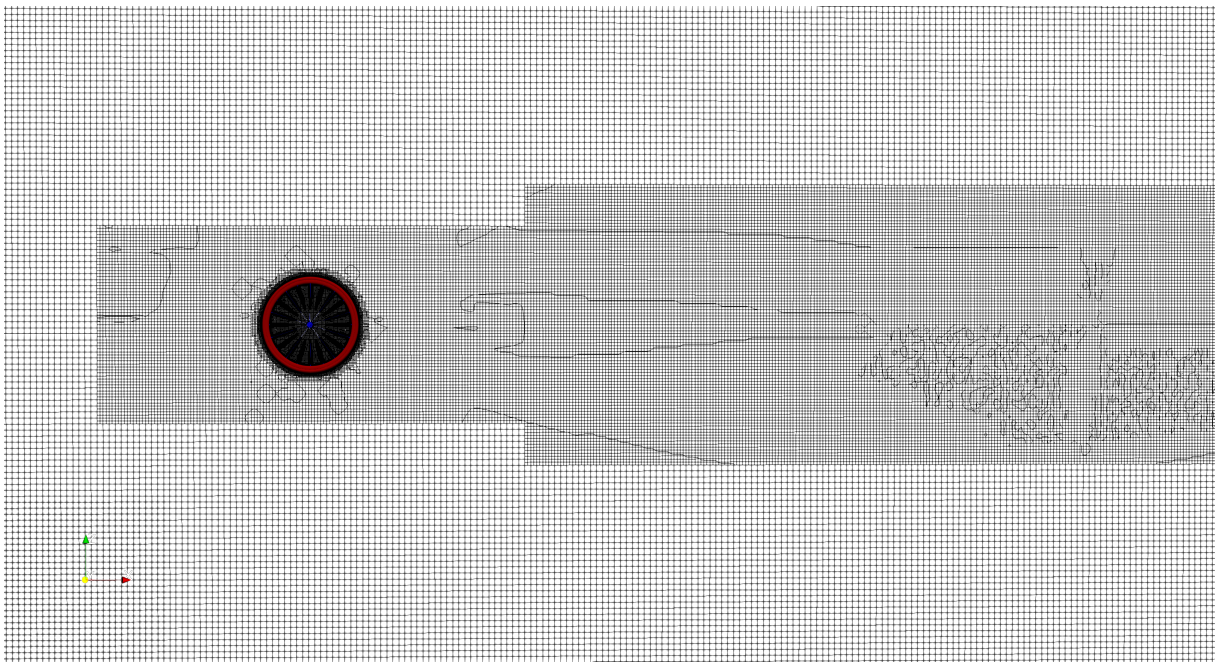

Figure 3.5: Mesh visualization (focus on the refinement)

For the reference case, the one investigating the mesh convergence, the rotation is modeled simply using the Rotating Wall Boundary Condition (RWBC) to have a fast and robust convergence and reasonable computational time for every case. For this case, the boundary condition is applied to the rim and spokes patches for the spokes wheel and to the overall disc for the case of the lenticular wheel. The center of rotation is centered in the hub of the wheel and the radiant velocity is obtained by dividing the flow velocity of the inlet boundary condition for the radius as described in the previous chapter. Particularly, the tangential velocity of the outer diameter of the wheel coincides with the simulated velocity of the flow at the inlet.

The computational grid is generated using $blockMeshDict$ where a starting reference distance of 0.08 m is used to initialize the reference volume around the wheel and then it decreases to 0.070, 0.060, 0.050, 0.045, 0.0425, 0.040, 0.038 $[m]$ to have a finer mesh. In this case, cubic cells are composed of all the rectangular shapes of the volume. Then, $surfaceFeatureDict$ imports the "stl" files of the geometry of the wheel which is used by $snappyHexMeshDict$ to mesh the geometry inside the initial domain.
All the parameters used inside $snappyHexMeshDict$ are chosen by the best knowledge of the author to have the best compromise between mesh quality, number of cells, and quality of the meshed geometry. The final results is showed in Fig. 3.14.

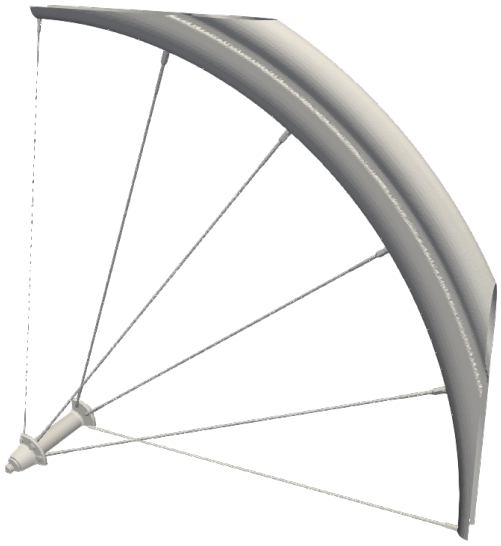

Figure 3.6: Surface details of the rim and spokes after the $snappyHexMesh$ meshing process.

Moreover, a refinement feature to catch the body-of-influence (BOI) around the geometry is created. The shape of the two BOIs is rectangular with a refinement level of 1 which means the initial volume of the cell is divided into four new cubics as highlighted in Fig. 3.5 where they can be seen by the darker black rectangular shapes. Next, in this directory, the option layer is activated to have 12 prism layers of 0.1 mm of height, independent of the mesh, with an expansion ratio of 1 in order to guarantee a y^+ lower than 5 on the overall geometry.

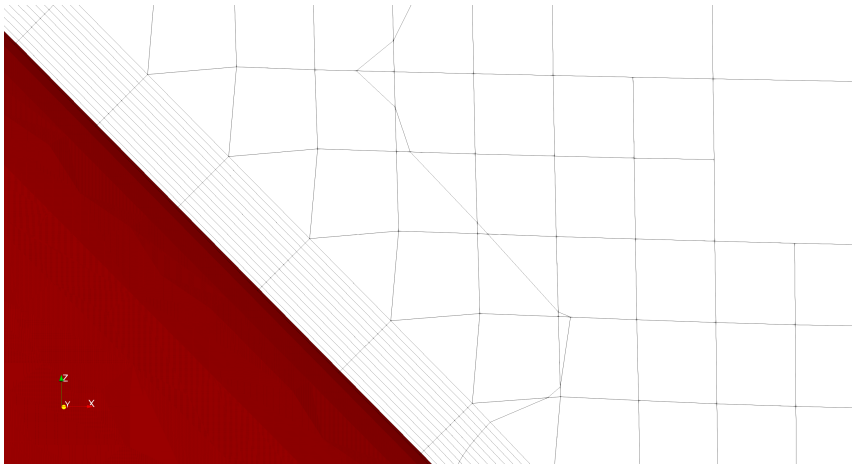

Figure 3.7: Layers on the rim and spokes after the *snappyHexMesh* layer addiction phase meshing process.

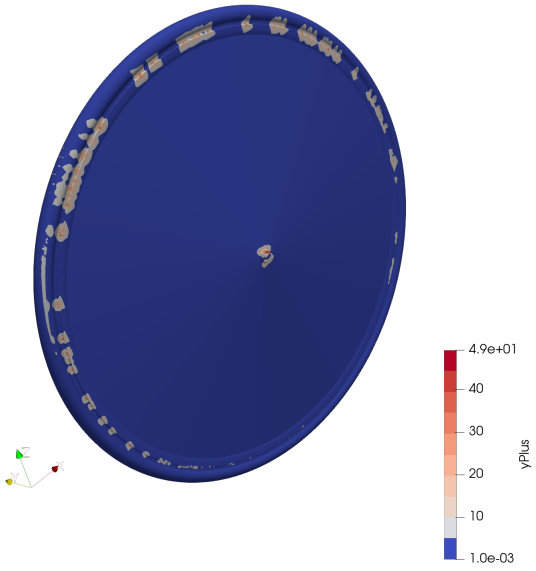

Figure 3.8: y^+ on lenticular wheel

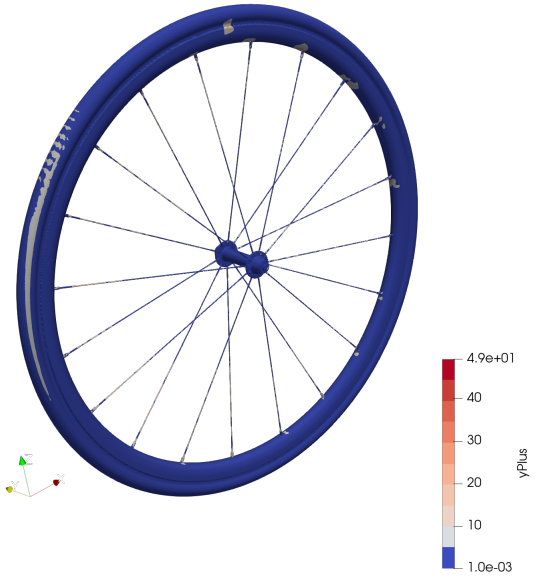

Figure 3.9: y^+on spoked wheel

3.3. Boundary conditions and computational settings

A uniform approach-velocity (U=15 m/s) and turbulence intensity (TI = 0,1%) profile is used at the inlet boundary, in line with the experiment found in the state of the art and with the turbulence value obtainable in the wind tunnel, especially in the Politecnico of Milan Wind Tunnel. The inlet-specific dissipation rate ω is computed from the turbulence intensity and hydraulic diameter. The latter is set to 0.68m based on the characteristic

dimensions used in the experiment. inletOutlet condition is used at the outlet. The pressure is set to zeroGradient at the lateral, top, and bottom faces of the domain, while equal to zero at the outlet. The boundary conditions for the quantities k and ω are set to slip for the lateral constraints, fixedValue at the inlet, and inletOutlet at the outlet while they used the wall functions on the wheel. Nut is calculated based on the initial assumptions on the whole domain a part of the surface on the wheel where it also uses the wall functions. The rotational velocity boundary condition is set at $41.12 rad/s$. The wheel roughness is assumed to be zero, which is a common simplification in cycling aerodynamics.

The velocity and the rotational velocity are then adapted to the different yaw angles. Indeed for the steady state case, the inlet velocity is maintained constant while the rotational velocity is calculated based on the yaw angle, while for the unsteady cases, the inlet velocity varies according to the setup to create the crosswind direction directly at the inlet. These two approaches are justified by the attempts to find the best stability and convergences for the different setups. All the values are deeply described in section $FlowAngle$ in the end of this chapter.

For the reference case, 3D RANS equations are solved together with the $k-\omega SST$ turbulence model which guarantees optimal stability. The RANS approach is the common approach for studies on cycling aerodynamics and has been shown to provide a good agreement with the WT measurements provided that proper computational parameters are applied. Note that no wall function models are used because of the multiple layers which do not require their applications. In this case, the solver $simpleFoam$ is used which reaches the convergence after a certain amount of iteration. All the values obtained are root mean squared over the last 400 steps of 2000 steps when the residuals and the output values show a good trend of convergence.

For the unsteady cases, $pimpleFoam$ is adopted and Δt of the order of magnitude around 10^{-4} or 10^{-5} is used to compute the simulation with a constraint of the Courant number which stays below 10. The choice has been made after some attempts to find the best compromise between the stability and computational time of the simulation. The simulations are carried out for $1s$ which corresponds to seven full rotations of the wheel and the results are obtained by averaging the last two rotations.

3.4. Mesh convergence

A mesh convergence study is conducted to reach the correct trade-off between accuracy and computational effort. The computed mesh is used during all the cases investigated a but not for the ones which adopted *pimpleFoam*. For the unsteady simulation, a coarser mesh is investigated to have a reasonable computational time but the increment of the quality of the turbulence model or of the rotation model adopted as well as a higher order solution method guarantees the convergence of the results. To study the convergence eight different meshes are tested. The refinement of the overall mesh is obtained by maintaining the same setup of *snappyHexMeshDict*, hence the same refinement for boxes and for surfaces, as well same amount and size of layers which are independent of the size of the initial mesh, while the number of initial cells obtained through *blockMeshDict* are intensified decreasing the length of each cell: from a distance of 0.08m until 0.038m. The size of the overall mesh and the number of surface cells for each mesh are shown in the Tab 3.1.

	number of elements			
	lenticular wheel	**surface**	**spoked wheel**	**surface**
mesh 1	2173857	119266	2482211	65513
mesh 2	3183847	156478	3455578	84753
mesh 3	4997174	213894	5154934	113693
mesh 4	8440146	308986	8606606	162825
mesh 5	14321292	380929	11941408	199063
mesh 6	16702862	424919	13961150	220934
mesh 7	19319130	480342	16162504	249288
mesh 8	22821162	546149	19254416	281195

Table 3.1: Number of elements for different mesh configurations

Where even if the *blockMeshDict* is initially the same the two different wheels have some difference in terms of the number of elements. This is because the lenticular wheel has a bigger surface which means more elements to mesh and more consistent boundary layers on the overall object. To evaluate the final mesh to use, the parameters compared are:

- The drag coefficient;
- The ventilation moment on y-axes;
- Qualitatively the pressure coefficient C_p is plotted around the wheel adopting as

zero angle the negative direction of x-axes (where the flow arrives on the wheel) and with an counter-clockwise direction as positive as shown in Fig. 3.10

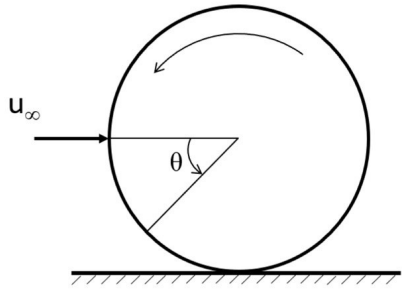

Figure 3.10: Counter-clockwise convention adopted

The convergence of the value is shown in the graph, while the table describes the percentage difference between each mesh.

For what concerns the values C_d and C_m, they are a-dimensionalized using as reference velocity $U_\infty = 15m/s$, reference area the overall surface of the rim which means $S_{ref} = \pi \cdot radius^2 = 0.362m^2$. Using this area as a reference standardize all the results according to other papers which treat the same topic [23]. Furthermore, it represents the worst-case scenario in terms of coverage surface by the wheel inside the simulated wind tunnel, because the rotational is perpendicular with respect to the flow, but it leads to a value of blockage ratio below the 1%. ($BR = \frac{S_{ref}}{S_{windtunnel}} = \frac{0.362m^2}{49m^2}$).

The different C_p are plotted in the following graphs.

	Errors between meshes			
	Lenticular Wheels		**Spoked Wheels**	
	Error Cd [%]	**Error Cm [%]**	**Error Cd [%]**	**Error Cm [%]**
mesh 1	2.7	5.2	15.9	17.8
mesh 2	1.5	1.6	5.8	6.2
mesh 3	1.4	1.0	6.9	1.0
mesh 4	1.7	1.9	2.7	9.2
mesh 5	2.4	0.4	2.6	2.1
mesh 6	0.2	1.1	1.9	1.4
mesh 7	1.5	0	0.5	1.0
mesh 8	0	0	0	0

Table 3.2: Convergence values and relative errors

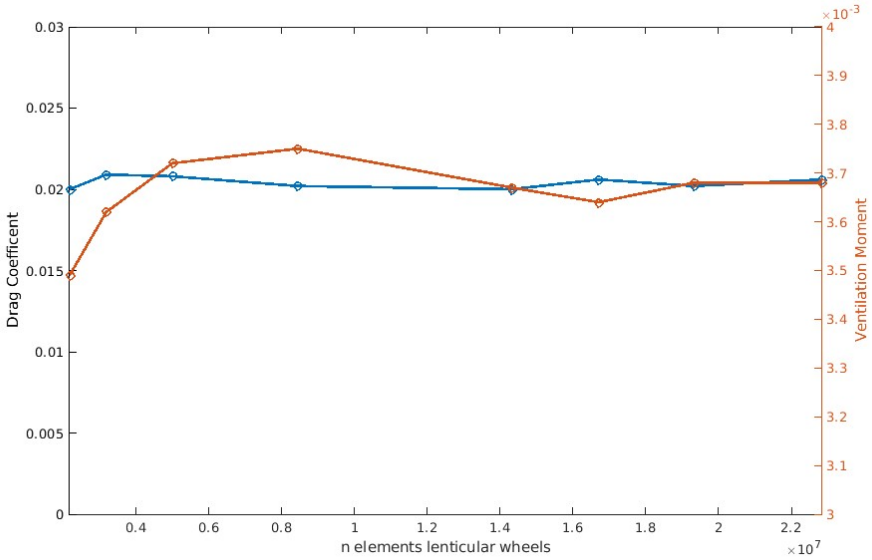

Figure 3.11: Mesh Convergence for the Lenticular Wheel

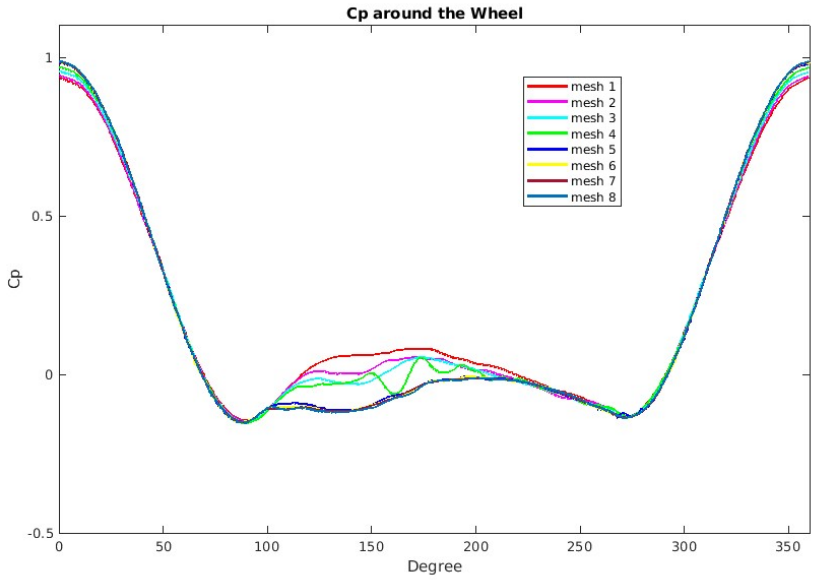

Figure 3.12: Pressure Coefficient around the Lenticular Wheel

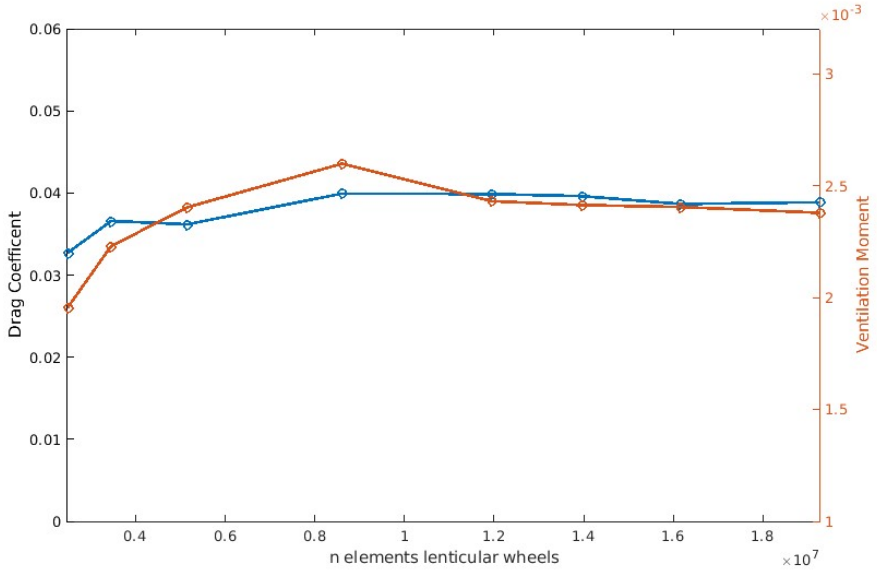

Figure 3.13: Mesh Convergence for the Spoked Wheel

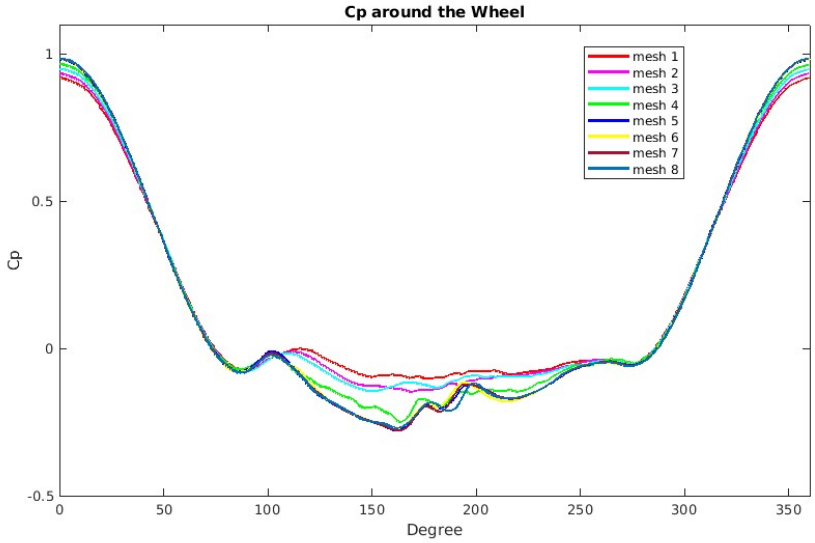

Figure 3.14: Pressure Coefficient around the Spoked Wheel

Mesh 6 is chosen because of the limited errors which stay below the 2%, also the C_p around the wheels converges.

3.5. Case Setups

As soon as numerical setup and mesh criteria are set, different rotational models are studied and tested to find the best compromise between computational cost, reliability, and accuracy of the models.

3.5.1. Impact of rotational modeling

The setup is made with wheels that can rotate freely in mid-air as the rotating model changes. Only the boundary condition involving the outer box of the "wind tunnel" remains the same as the one described in the previous paragraph. In OpenFOAM, different methods can be used to simulate the physical rotation of an object in a CFD simulation. The first three methods are standard and widely used depending on the objective of the simulation, while the fourth method is, to the best and humblest knowledge of the author, used for the first time in this field, and these are:

- Rotating Wall Boundary Condition (RWBC)
- Moving Reference Frame (MRF)
- Sliding Mesh (SM)
- Rotor Disk Method

Every case has its pro and cons, and the mesh and case setup is slightly different for every case as explained in the next sections. Furthermore, every case is simulated at 0, 5, 10, 15, and 20 degrees of yaw angle to evaluate the impact of the model at different wind conditions. The 5 different setups are chosen because are the most common wind condition during cycling races considering the cyclist's velocity [35].

3.5.2. Rotating Wall Boundary Condition

For this case, the mesh process is the one described in the previous paragraph because it is used as a reference case.

3.5.3. MRF

In this case, the process for the case setup is slightly different. After the meshing process, the command *topoSet* and *setsToZones* are used to define the region on which applied the moving reference frame. The impact of the MRF in terms of size and shape is investigated

at different yaw angles.

Impact of the size of the MRF volume

In the first case, a cylindrical region is chosen around the two types of wheels. The width of the cylinder remains constant and it is equal to $26cm$, while the radius increases from a value which is exactly the radius of the wheel ($0.34cm$) then $0.37cm$ and $0.40cm$. The thickness is chosen to be able to contain the wheel even at 20 yaw angle. Indeed for this setup, the cylinder volume containing the wheel remains in the same position while the wheel inside rotates around the z-axis. Moreover, for the 0 yaw angle, another simulation with a cylinder thickness of $11cm$ is investigated to analyze the sensibility also on this dimension and not only on the radius. In this case, the dimension is exactly the length of the hub of the wheel ($11cm$)

Figure 3.15: MRF configuration 1, $r = 34cm$, front view, case yaw angle = 20

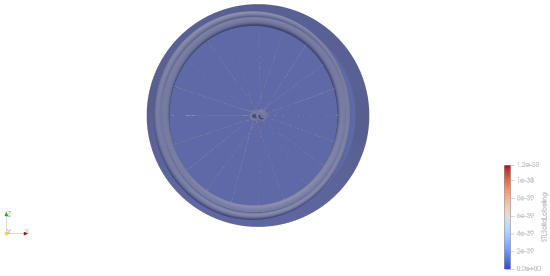

Figure 3.16: MRF configuration 1, $r = 34cm$, side view, case yaw angle = 20

The second case, hence the second shape investigated, is derived from the "stl", particularly the lenticular wheel. In OpenFOAM, there is an option to select a region inside a mesh starting from a geometry file. In particular using the lenticular wheel "stl" file distance of $1mm$, $1cm$, and $5cm$ (to compare almost three orders of magnitude) from the file are chosen to select the region. In this way, the region to apply MRF is very close to the geometry, especially for the lenticular case, but in the case of spokes, the spokes remain inside the region selected, and the thickness of the region is increased for the three different cases.

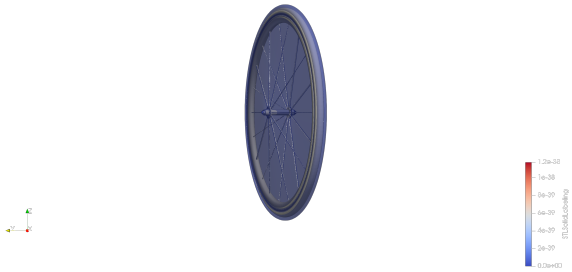

Figure 3.17: MRF configuration 1, $s = 0.001m$, front view, case yaw angle = 20

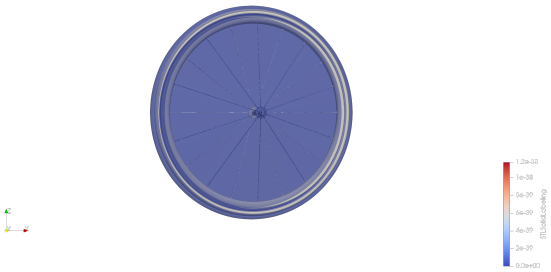

Figure 3.18: MRF configuration 1, $s = 0.001m$, side view, case yaw angle = 20

The third and the fourth cases are simulated only for the spokes wheel. The third one uses the same philosophy as the second but the files selected are the rim and the spokes "stl" geometry. In this case for the spokes the selected region is not a solid of revolution which is a controversial application for the MRF but for the sake of curiosity is still being investigated.

The fourth case is an application of a hybrid model. In particular, the rotating wall boundary condition is applied to the rim while for the spokes region, the MRF is applied. In this case, a frustum shape is modeled to cover the spokes region. This setup is called MRFg.

Figure 3.19: MRF configuration hybrid, case yaw angle = 20

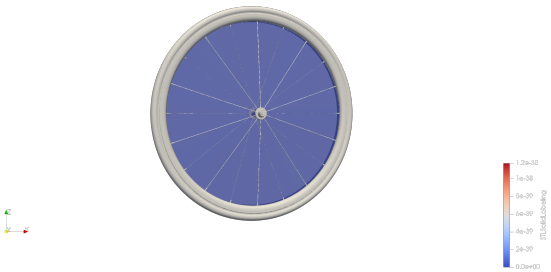

Figure 3.20: MRF configuration hybrid, case yaw angle = 20

3.5.4. DDES Case

This case adopts another mesh resolution which is also used for the investigation of the sliding mesh approach. This mesh resolution maintains the same level of the number of surface cells on the body but reduces the volume of the BOI. In fact, only the cylinder around the wheel is refined. Moreover, the boundary layer is solved with the wall function

so the layers are not present and this configuration significantly reduces the number of cells. Moreover, the application of DDES, in this case, is less related to the study of rotational modeling, but it simulates the structure of the turbulence vortex during a transient scenario. Due to the high computational cost of this turbulence approach, a truly accurate mesh is not the focus of this paper, which aims to highlight the advantages and disadvantages of the rotational model rather than a deep investigation of the turbulence model. For this case, only the case of zero yaw angle is analyzed due to the time needed for each simulation. The rotation model used for this case is the MRF volume resulting from the extrusion of the CAD by 1 mm. The choice was made after analyzing the rotation models, choosing the best compromise between the computational cost of the model and the reliability of the results.

3.5.5. Sliding Mesh

For the Sliding Mesh approach, the mesh setup is slightly different. Because of the high computational cost of this approach, the quality of the mesh is adapted. In this case, the ROIs are not anymore the two rectangular shapes as before, but just a cylinder around the wheel to have a high-quality mesh in the radial direction. In this way, the rotating region is obtained with the following dicts: $createBaffles$, $splitBaffles$, $createNonConfomformalCouples$.

The region used is a simple cylinder with a width of $26cm$ and radius a slightly bigger than the one of the wheels (radius = 35 cm).

The same meshing approach is used for both the lenticular and spokes wheels.

3.5.6. Rotor Disk Model

For this last approach, only the spoked wheels are investigated because the rotor model can ideally substitute the spokes. One of the geometry files used for the meshing procedure is different, indeed in this case the spokes are not geometrically imported but modeled using the $fvModels$ file inside the *constant* folder. Hence, only the hub is imported, as well as the rim. On these two surfaces, the rotating boundary condition is applied.

For the application of the model, where the spokes are replaced by volume forces, a region must be selected. In this case, to try to simulate the inclination of the spokes between the hub and the rim, a half-frustum region is adopted. Then the model is applied to its extremity to have the force applied at the exact place of the spokes. Moreover, two

symmetric regions must be chosen, because the application of the model requires two different coordinate systems to have the application at the inclined surface and not at the center. Different attempts are simulated to tune the model in terms of volume forces applications places. Only the best qualitative attempt is investigated in this work.

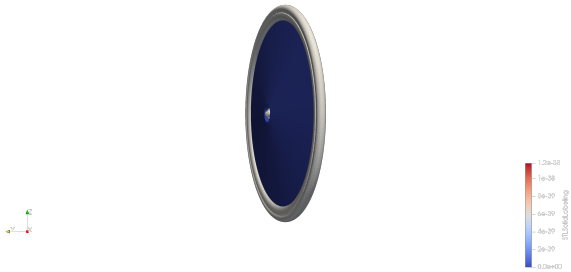

Figure 3.21: rotorDisk configuration, case yaw angle = 20

Figure 3.22: rotorDisk configuration, case yaw angle = 20

In the previous Fig 3.21 and Fig 3.22, the blue volume is the volume where the volume forces of the spokes are simulated, while on the rim the RWBC is applied. Every spoke is considered as a cylinder, thus the input inserted in the file are the number of spokes which are twenty, and the drag coefficient imposed which is chosen as 1.2 as found in the literature for Reynolds number between 10^4 and 10^6.

3.5.7. Flow Angle

As announced previously the wheels are tested at different yaw angles. The following Fig. 3.25 shows the wheel at speed V_{bg}, which stays for bike-ground. The crosswind is represented with the velocity V_{wg} (wind-ground) with a direction γ with respect to the direction of the bike wheel. The effective wind velocity that the road bike sees is given by V_{wb} (wind-bike) and by the angle β (yaw angle to the direction of motion). Thus any combination of wind speed, direction, and bicycle speed leads to final relative velocity V_{wb} and yaw angle β.

The situation is modeled inside the simulation by rotating the geometry or the moving mesh, increasing the rotation velocity ω to have a tangential velocity in the x direction constantly equal to the wind speed which remains constant at $U_{wind} = 15m/s$. Thus the force components are decomposed between axial and lateral force as shown in Fig. 3.24. Indeed the cyclist experiences an axial drag force F_a in a direction opposite to his direction of motion, and a side force F_s perpendicular to his direction of motion.

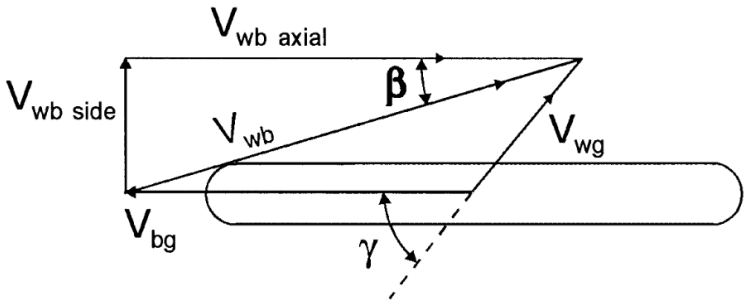

Figure 3.23: Velocity vectors for the bicycle wheel.

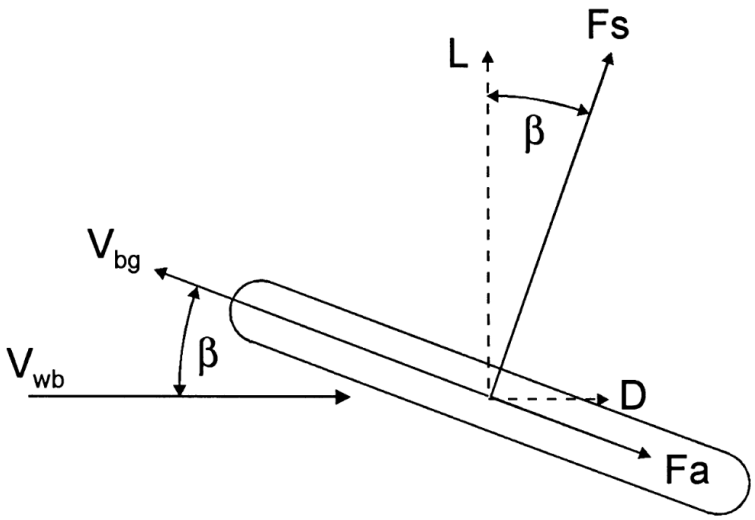

Figure 3.24: Measured and resolved forces on the wheel.

From Fig. 3.25 six standard conditions of cycling can be identified:

- Perfectly still conditions ($V_{bg} = V_{wb}, \beta = 0°, \gamma = 0°$);
- Headwind ($V_{bg} < V_{wb}, \beta = 0°, \gamma = 0°$);
- Tailwind ($V_{bg} > V_{wb}, \beta = 0°, \gamma = 180°$);
- 90° crosswind (($V_{bg} = V_{wb}$ axial, $\beta > 0°, \gamma = 90°$);
- Angled headwind ($V_{bg} < V_{wb}$ axial, $\beta > 0°, \gamma < 0°$);
- Angled tailwind ($V_{bg} > V_{wb}$ axial, $\beta > 0°, \gamma > 0°$);

It can be noticed that the force can be decomposed in axial and perpendicular directions

with respect to the wheel. For the calculation for axial and lateral components, it can be seen from Fig. 3.24 as $F_a = Dcose\beta - Lsin\beta$ and $F_s = Dsin\beta + Lcos\beta$. Hence the axial component of the "lift" acts in the direction of motion of the cyclist and it is considered a negative force that assists his motion rather than retards it. It follows that a simulation could arise where the axial lift component exceeds the axial drag component and then the axial force becomes negative implying that the wheel is acting like a sail to propel the cyclist forward. The same considerations apply to the side force (F_s) except that both the axial and side force components of (D) act in the positive direction [35]. Hence, in order to have the same U_∞ for every case at every yaw angle, the rotational velocity ω increases to have the tangential velocity for the $x - direction$ constant. Moreover, the rotation normally changes according to the yaw angle. In the table all the new rotational velocity and axis of rotation that counts for every boundary condition.

	Yaw Angles		
angle [°]	$omega[rad/s]$	**x**	**y**
0	44,12	0	1
5	44,2861693	0,087155743	0,996194698
10	44,79823288	0,173648178	0,984807753
15	45,67394914	0,258819045	0,965925826
20	46,94901937	0,342020143	0,939692621

Table 3.3: Initial Rotational Velocity and Axis of Rotation at Different Yaw Angles

For the unsteady case to have better convergence and stability during the simulation the geometry remains at the original position, hence the boundary condition on it in terms of the angular velocity of the sliding mesh is constant for every yaw angle, while the inlet velocity is deflected to simulate the effect of the yaw angle. Indeed, in the x-direction, the inlet velocity remains at 15 m/s, while a component in the y-direction is added and calculated based on the different angles. In particular, its magnitude is respectively 1.31, 2.60, 3.88, and 5.13 m/s. Because of the large domain and the low blockage ratio, the other boundary conditions remain standard, considering the lateral walls do not affect the results on the wheel. Results are compared qualitatively and quantitative based on the following criteria:

- F_d and F_l (respectively drag and lateral forces) decomposed on $x-axis$ and $y-axis$ for different yaw angles;
- C_p plot around the wheel;

- Qualitatively adopting the y-normal cutting planes;
- Comparing qualitatively using Q-Criterion.

3.6. AeroCloud by NablaFlow Setup

The final section of the numerical setup briefly explains the simulations obtained through AeroCloud. AeroCloud is an online platform where it is possible to make advanced CFD simulations fast and available to everyone. By keeping the workflow simple and efficient, AeroCloud takes care of the simulations while it is possible to increase the focus on design and development. The meshing and simulation processes are fully automated and tested on a wide range of validation cases to provide stable and reliable results. For this work, the lenticular wheel is investigated and the results are compared to RWBC of OpenFOAM. All the numerical setup is fully automated and the results are easily obtainable. Some details of the simulations are in the next table:

Aerocloud version	v6
Simulation type	Standard
Fluid	Air
Kinematic viscosity	15.0 cSt
Density	1.225 kg/m3
Speed	15.0 m/s
Yaw angles	0.0°, 5.0°, 10.0°, 15.0°, 20.0°
Ground	Off
Rotation	rolling
Number of cells	10798224

Table 3.4: Simulation Settings for AeroCloud

It can be noticed that the number of cells is slightly lower than the convergence obtained in OpenFOAM simulations, but in this setup, the boundary layer is computed through wall functions and not adopting the layer addiction phase which increases the final number of cells. Moreover, the yaw angles are computed by changing the direction of the flux and not rotating the geometry around its axis. For completeness of the coordinate system, the yaw angles and forces are defined as follows: Forces and moments are defined according to the right-hand coordinate system shown in fig.3.25. The original coordinate system of the 3D model (s) is adopted, with positive drag force along the x-axis and positive lift force along the z-axis. Roll, pitch, and yaw moments are calculated around the

corresponding coordinate axes. The yaw angle is defined as the angle between the wind vector and the model x-axis and is positive counter-clockwise. Hence maintaining the closest configuration available on AeroCloud to the previous reference case.

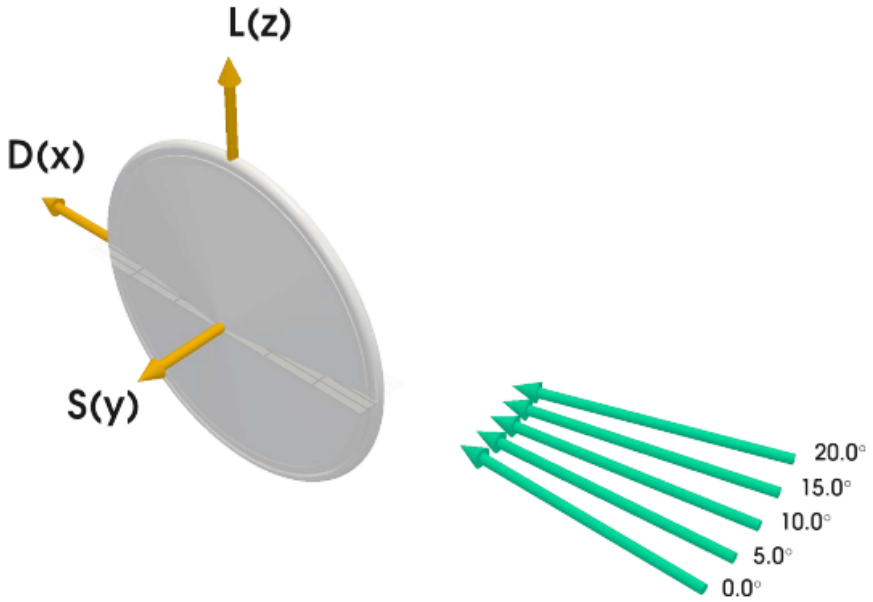

Figure 3.25: Coordinate system and wind direction

In order to visualize the flow feature AeroCloud offers an automated streamline setup which is used to compare the different simulations. Streamlines show the trajectory of a fluid particle as it moves downstream in a fluid flow. They can be used to show the overall structure of the flow field around a body and the extent of the wake. To visualize the streamlines we add a seeding array of weightless particles into the flow upstream of the object, like smoke traces are used to visualize airflow in a wind tunnel. In areas of accelerated flow, the streamlines come closer to each other, and in decelerated regions, they will separate. The colors of the streamlines correspond to the total flow velocity.

4 | Validation

In this study, the wind tunnel measurements conducted by Belloli et al. [19] are utilized for validating computational fluid dynamics (CFD).

4.1. Experimental Results

These experiments investigated by Belloli et al. [19] were aimed to measure the aerodynamic forces on two high-performance wheels. Additionally, a Particle Velocimetry test was performed to reconstruct the flow field around the wheels and examine differences caused by variations in tyre shape. In this context, the reference system defines drag force as the opposing force to the vehicle's motion. The relative velocity magnitude is evaluated based on the reference frame, which considers a wind blowing orthogonal to the bike's motion in both the study and subsequent simulations. To align the wheel's tangential velocity with the wind velocity, the wheel rotation was calibrated at a bike cruise speed of 50 km/h under stationary conditions.

The study took into consideration yaw angle tests ranging from -20° to 20° to account for a wide range of yaw angles experienced by cyclists. However, for validation in CFD, only yaw angles from 0° to 20° were considered. The Experimental Test was conducted at the Politecnico di Milano Wind Tunnel - CIRIVE, which features a closed circuit system with two test sections. One section, measuring 14x4 meters, is designed for low-speed boundary layer tests, while the other, measuring 4x4 meters, is used for high-speed tests.

The tests were performed in the lower section of the facility, which enables higher wind speeds. The maximum achievable wind velocity in this chamber is 55 m/s, determined by evaluating hydraulic load loss through pressure measurements upstream and downstream of the contraction cone preceding the test section. The dimensions of this section allow for full-scale testing with negligible blockage effects and very low turbulence ($I_t = 0.15\%$).

The objective of the test was to identify the aerodynamic differences between two tires mounted on a $DuraAceC60$ wheel, characterized by a v-shaped cross-section with a 60mm chord and 16 spokes featuring an elliptic cross-section. The CAD file of the wheel was

employed for CFD validation, with the simulated force values compared against the experimental tire outputs.

A specific balance setup was designed and replicated within the CFD simulations. To drive the wheel, an electric motor was positioned beneath the ground board, generating a uniform wind profile and shielding instruments and supports. The wheel support, connected to the wind tunnel section turntable, enabled rotation at different yaw angles to simulate crosswinds. The isolated wheel was secured to a steel holding fork attached to an aluminum plate fixed on the ground, with the motor, force balance and load cell connected to it. To stabilize the flow around the wheel and prevent vortex shedding from the wheel supports, two NACA 0021 profiles were employed to cover the steel holding fork, as depicted in Figure 4.1.

Figure 4.1: Detail of wheel support NACA 0021 profiles and PIV setup.

To visualize the flow field surrounding the wheel, a Particle Image Velocimetry (PIV) test was conducted. PIV serves as a valuable tool for evaluating the flow field, including the magnitude and direction of the flow, as well as visualizing flow structures that would

otherwise remain invisible. In this test, solid particles within the size range of 1-2 μm were introduced into the wind tunnel circuit and illuminated by a laser beam. A high-speed camera captured consecutive frames, which were subsequently processed to track the motion of the particles. To minimize light reflections, a black matte plastic film was applied to the floor beneath the wheel.

Aerodynamic forces on Tyre A and Tyre B have been plotted in 4.2 and 4.3:

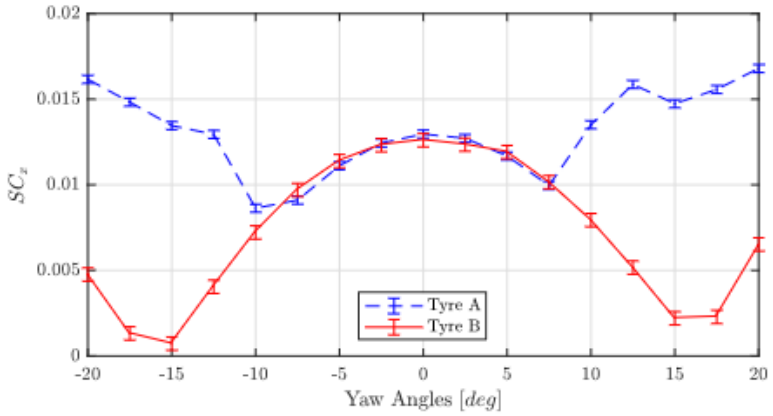

Figure 4.2: Normalised drag force [19]

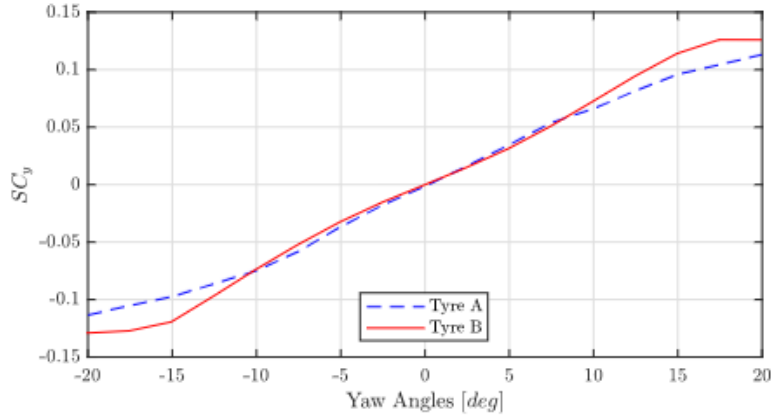

Figure 4.3: Normalised side force [19]

The wheels employed in the force measurement tests were also utilized for the PIV tests. However, the reconstructed flow field obtained from PIV lacks precision. Recordings were conducted for all tested yaw angles, but only the most representative ones are presented here. The PIV measurements assist in comprehending the factors contributing to the observed variations between the wheels. Here the plot of the main difference and the relative yaw angle can be seen in Fig. 4.4, 4.5, 4.6.

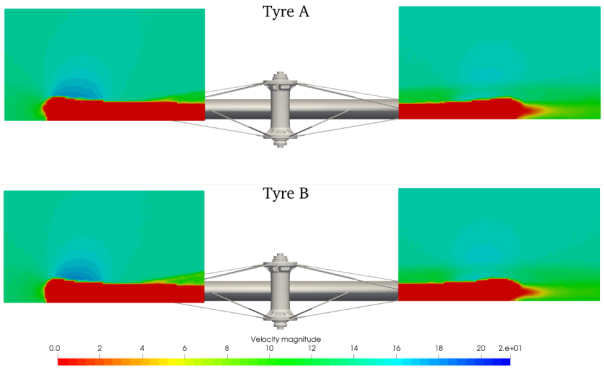

Figure 4.4: Velocity magnitude of the flow around wheels - Yaw angle = 00 deg at 102 mm over the hub [19]

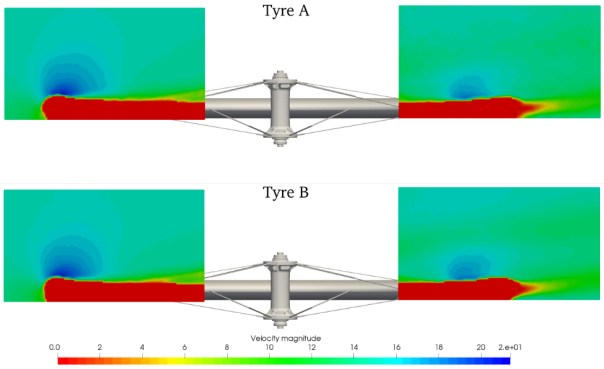

Figure 4.5: Velocity magnitude of the flow around wheels - Yaw angle = 10 deg at 102 mm over the hub [19]

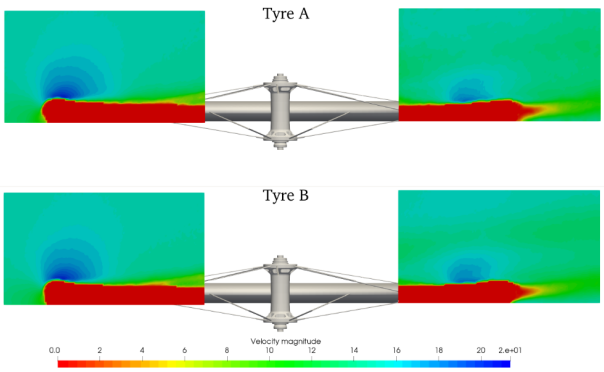

Figure 4.6: Velocity magnitude of the flow around wheels - Yaw angle = 15 deg at 102 mm over the hub [19]

4.2. Validation Results

The CFD setup is now explained and the results are compared with the wind tunnel test campaign. For the validation indeed a special setup has been implemented. The *blockMeshDict* has been modified to create the ground of the virtual wind tunnel maintaining the same initial dimension for the cell which was able to converge in the previous case. Moreover, the setup composed by the two NACA 0012, the *DuracAce C*60, and by the small shaft on which the wheel can rotate are obtained through the CAD and meshed with *snappyHexMesh*. The wheel rotation is simulated through the MRF approach and the volume considered is obtained thanks to 1mm extrusion from the CAD of the wheel, which demonstrates (as explained in the next chapter) good performance in terms of computational effort and results.

The boundary conditions are set to be close as possible as the real test. The geometry rotates inside the domain while the BC remains constant. The mesh and the setting are shown in Fig 4.7, 4.8 and Tab 4.1.

OpenFOAM version	v10
Fluid	Air
Density	1.225 kg/m3
Speed	13.89 m/s
Yaw angles	0.0°, 5.0°, 10.0°, 15.0°, 20.0°
Rotation	MRF
Number of cells	19356146
Number of surface faces	200484

Table 4.1: Simulation Settings for validation

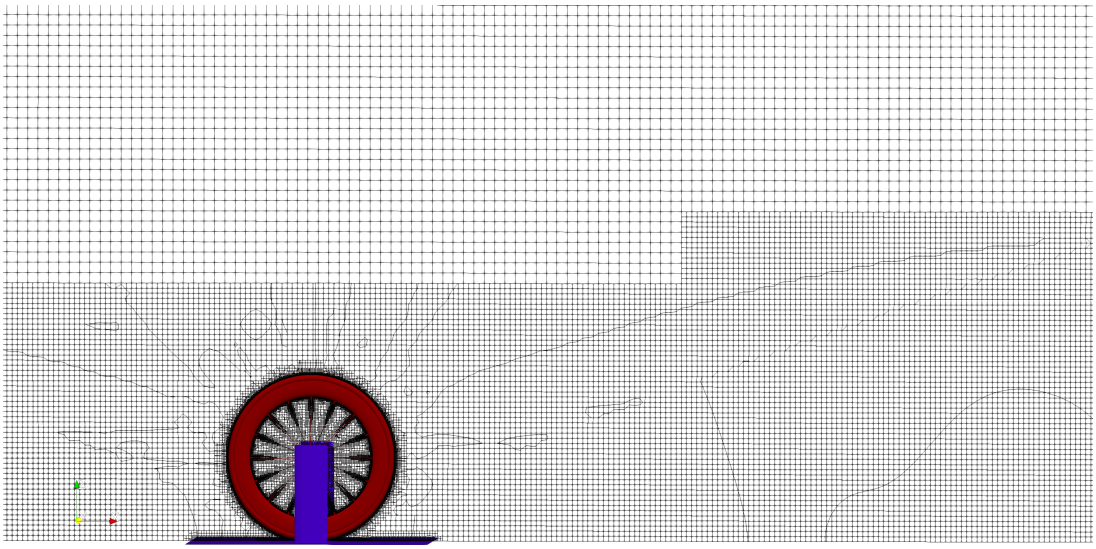

Figure 4.7: Mesh adopted for validation case

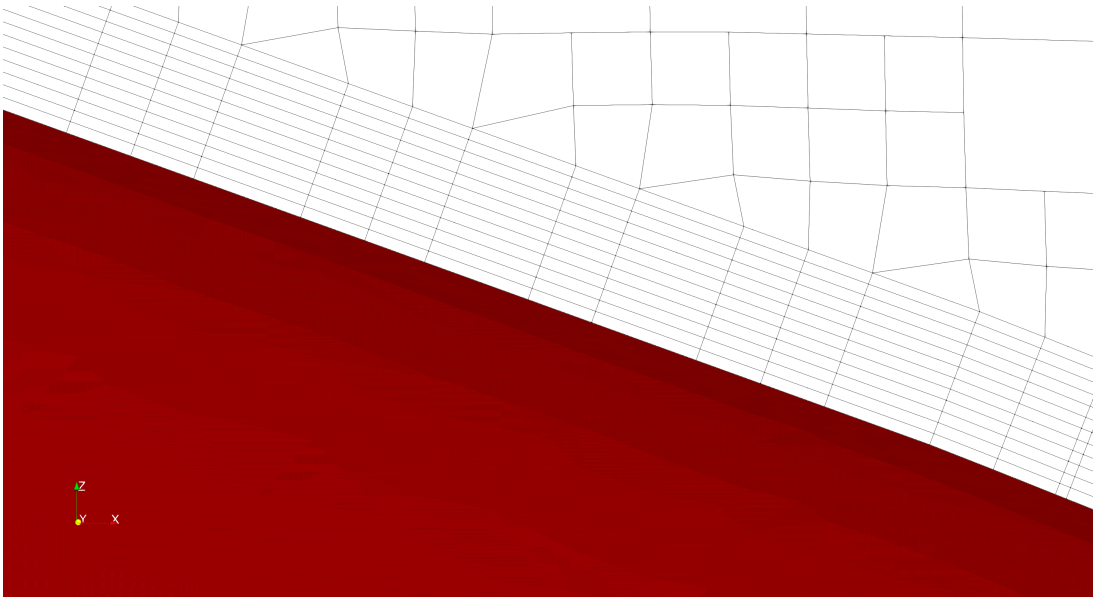

Figure 4.8: Detail of the mesh

In the table are presented the results at different yaw angle where the normalized forces are obtained as:

$$\text{Drag Force} = \frac{F_x}{1/2\rho V^2} \text{ and Side Force} = \frac{F_y}{1/2\rho V^2}$$

Validation - Normalized Force Comparison [N] (Percentage Difference compared to reference case)					
angle [°]	0	5	10	15	20
Ref Value	0.012	0.012	0.008 - 0.013	0.002 - 0.015	0.006 - 0.017
Drag Force	0.012 (0%)	0.011 (8%)	0.006 (25%)	0.003 (0%)	0.013 (0%)
Ref Range	0	0.037	0.070	0.01 - 0.12	0.11 - 0.12
Lateral Value	0	0.035 (5%)	0.063 (10%)	0.074 (0%)	0.065 (41%)

Table 4.2: Force comparison for validation

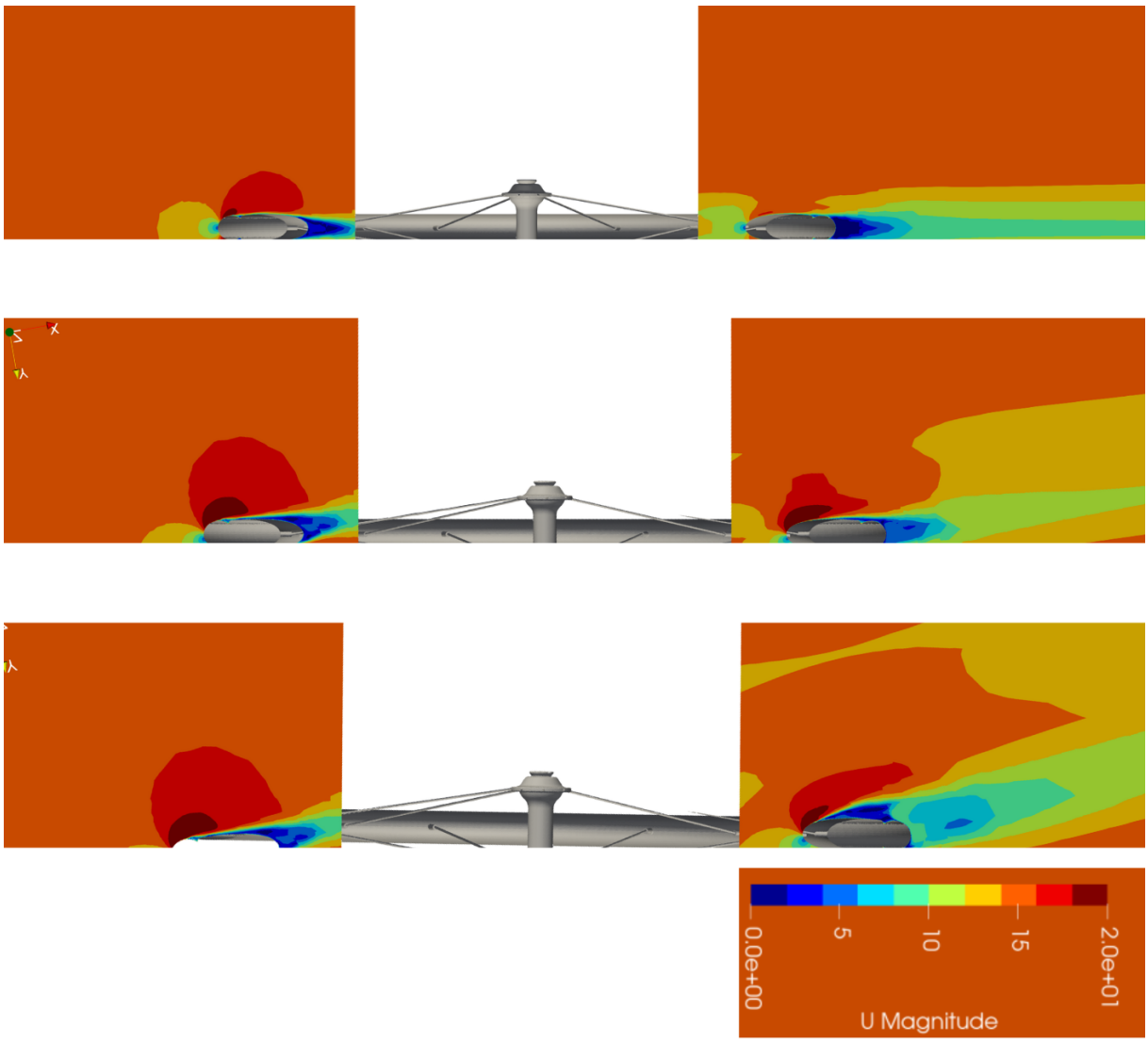

Figure 4.9: Velocity magnitude simulated- Yaw angle = 00, 10, 15 [deg] at 102 mm over the hub

The simulations result show significant agreement with the wind tunnel simulations. Indeed the values stay very close to range of the two tires tested. Only the drag force at 10 deg is 25% underestimated even for the lowest value, and the lateral force at 20 yaw angle is 41% underestimated. This behiaviour could be linked to the tire shape simulated which is slick in the case of the simulation, or for the present of the two NACA 0012 profiles which at 20 yaw angle can create some flux disturbances on the wheel and the turbulence model is not able to take them into account completely. Here in the figure, the flow feature at different yaw angle are presented and compared with the experimental results.

For what concern the quality of the flow simulated, the rotational model adopted is able to show the significant structure of high velocity flow which is created by the rim, especially at 10 and 15 deg of yaw angle. In fact for these two cases the flow behind the rim a red area is present and its size is also comparable to the blue one caught by the PIV in the wind tunnel. Also the wake size, coloured in blue in the simulations has an influenced comparable to the red one behind the rim which can be seen in the fig obtained by the PIV.

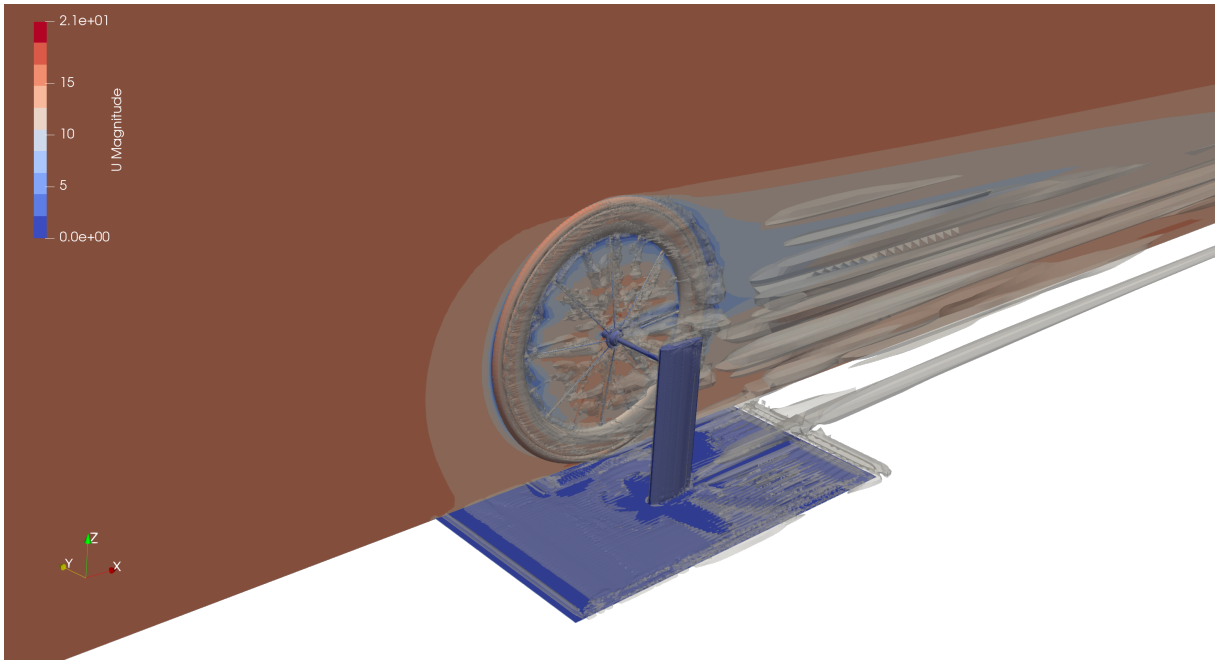

Figure 4.10: Velocity field at 0 yaw angle - Q criterion surface

5 | Results and Discussion

In this chapter, the results of simulations described in the previous section are presented. Methods are assessed by comparing time-averaged solutions for *pimpleFoam* and the last time-steps for the *simpleFoam* simulations, in any case when the convergence of values and residuals is reached. In the first section, the lenticular wheel is investigated, while in the second one, the spoked wheel is analyzed.

5.1. Lenticular Wheel

First of all the results of the lenticular wheel are analyzed starting from the steady solver to finishing with the unsteady algorithm.

5.1.1. Steady Models

For the lenticular wheel, the rotating wall velocity boundary condition case is used as a reference case. The choice has been made by the fact that a lenticular wheel is obtained by a solid of revolution [24].

Hence, before starting the methods comparison the RWBC solution is analyzed and described for the different yaw angles. The first figure 5.1 shows the drag force in the wheel direction and the side force in the lateral direction with respect to the wheel. The side force starts from zero value because of the symmetry of the problem, while it increases due to the huge surface of the disc wheel which demonstrates the instability of its use during the group races, and adopted on the front fork only on the track in closed conditions. The drag force shows an opposite trend. It starts from a positive value but because of the high flow velocity, the U_∞ is equal to $15 m/s$, the lenticular wheel shows the sail effect and the drag force over the 10° becomes negative.

To better explain the different forces acting on the wheel, the pressure coefficient is plotted in Fig. 5.2. Figure 5.2 illustrates the distribution of the pressure coefficient (C_p) along the center line of the wheel. The graph demonstrates the evolution of the C_p profile at

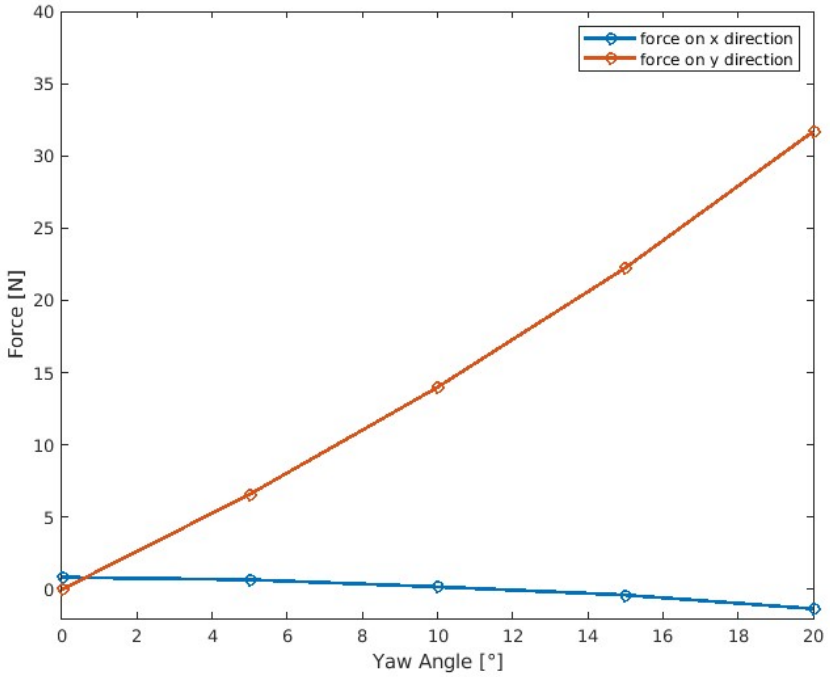

Figure 5.1: Forces on drag and lateral directions at different yaw angles.

various yaw angles. A C_p value of one is associated with stagnating flow, and it is found around 0° for the wheel with 0 yaw angle. The starting C_p (At 0°) decreases when the yaw angle increases because the stagnation point moves to the upper surface of the tyre. With increasing θ, C_p decreases until it reaches the lowest point around 90° for the red case, which means under the wheel, while for the other yaw angles, it moves forward because the depression caused by the huge lenticular surface has a higher impact respect to the rotation. Notably, at the rear of the wheel (at 180°), the coefficient remains constant and equal to zero which is linked to the separation flow region, especially at 270°, which is the top of the wheel, where the separation point may occur. For the other cases, the low-pressure zone expands as the yaw angle increases.

To further illustrate this trend, the C_p profile at $z = 0$ considering the z-axis as the normal of the plane, C_p is plotted in the subsequent figure 5.3. This plot highlights the changes in pressure coefficient at different yaw angles, considering the front and back of the wheel with respect to the flow direction as the reference system. Consequently, the upwind surface refers to the surface that faces the incoming wind.

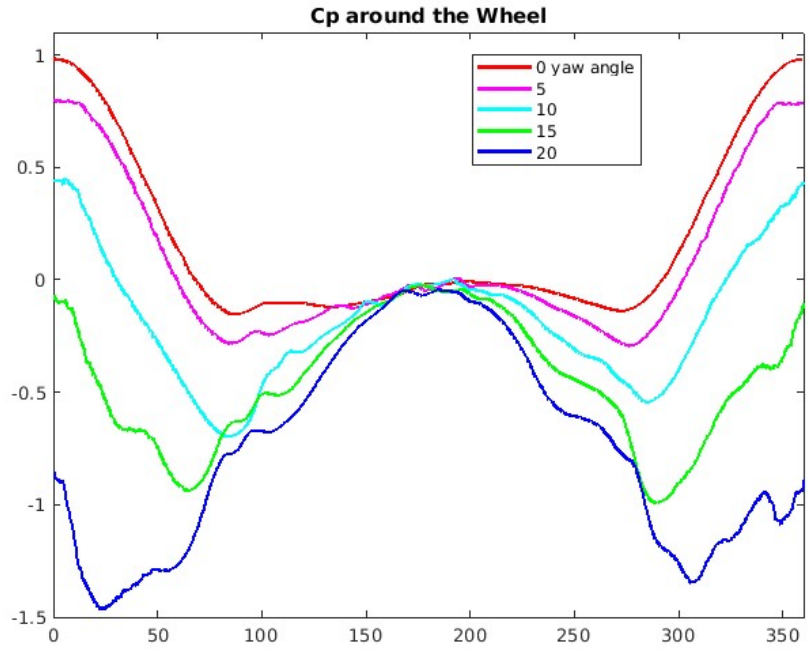

Figure 5.2: C_p profile around the wheel at different yaw angles

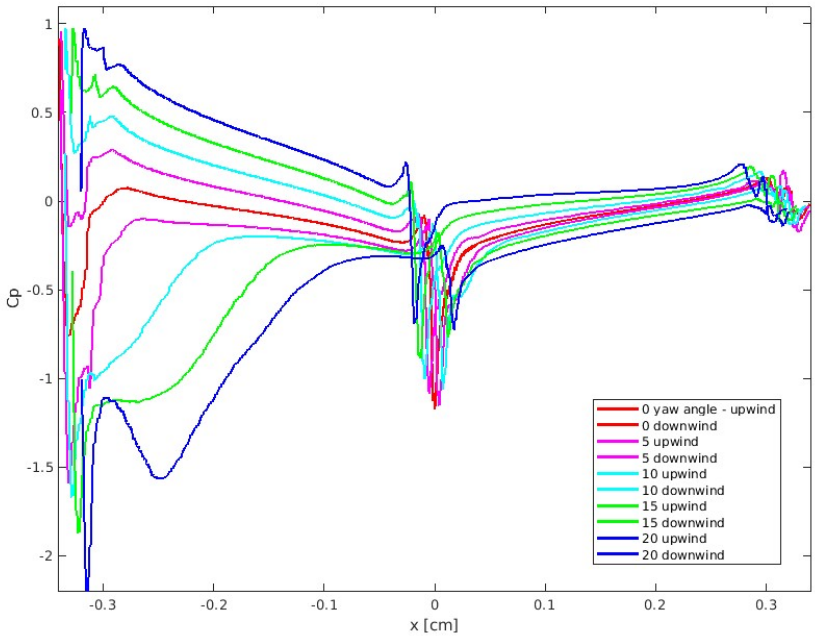

Figure 5.3: C_p profile at $z = 0cm$ at different yaw angles

At a yaw angle of 0°, the two surfaces exhibit symmetry with respect to the flow, resulting

in the two plots coinciding on the same line. However, as the yaw angle increases, the upwind profile diverges from the downwind profile, particularly in the first half of the wheel, prior to the hub. As explained before the stagnation point, so when C_p is equal to one, moves forward as the yaw angle increases. This is because as the wheel rotates around the z-axis, the most forward point is not anymore placed on the front of the wheel but it moves to the upwind surface. Moreover, it is crucial to note an abrupt pressure change at the hub, which may induce turbulence and flow separation downstream.

Moreover, the presence of a high wake zone behind the front section of the wheel, caused by an increased crosswind, leads to the generation of z-moments on the wheel. This factor renders the wheel unsuitable for windy conditions during outdoor applications, especially when used as a front wheel. Also, it can be associated with the pressure lateral force linked to the lenticular wheel when the yaw angles increase.

Graphically speaking, the wake and the separation zones are estimated showing the C_p on the back side of the wheel and using as $iso-surface\ C_{ptot} = 0$. Hence, the $iso-surface$ shows the same trend and increases its influence according to the yaw angle.

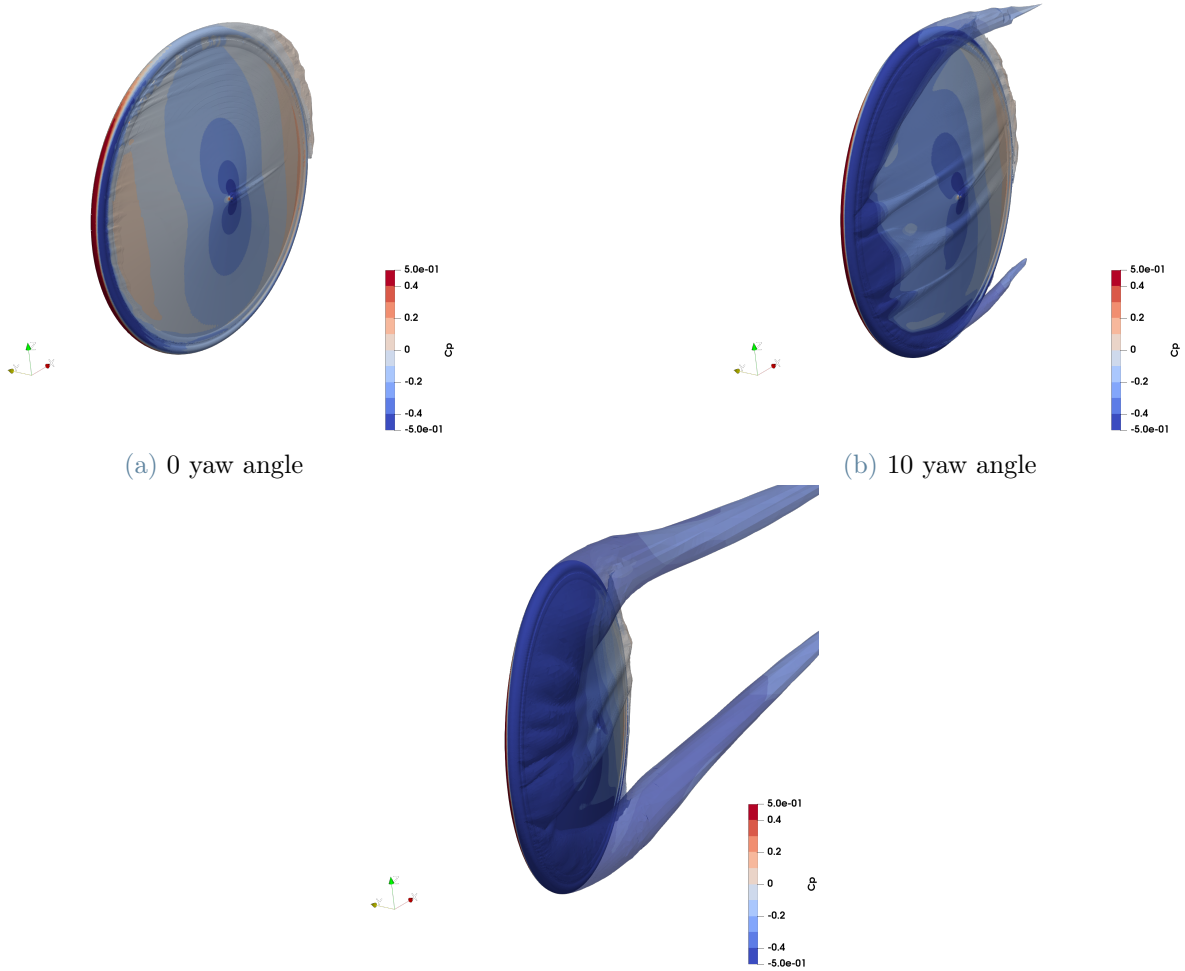

(a) 0 yaw angle

(b) 10 yaw angle

(c) 20 yaw angle

Figure 5.4: View of the low-pressure side of the wheel

MRF Analysis

Adopting as a reference case the RWBC which is analyzed in the previous paragraph, in this paragraph an analysis of the moving reference frame cases is investigated.

First of all the drag and lateral forces are compared for the different yaw angles. All the computed values are shown in the table 5.1 and 5.2:

Steady State Models - Drag Force [N] (Percentage Difference compared to reference case)					
angle [°]	0	5	10	15	20
RWBC	0.84	0.67	0.18	-0.38	-1.33
Cyl r = 34 cm	2.39 (184%)	2.18 (225%)	1.31 (627%)	0.12 (131%)	-1.49 (12%)
Cyl r = 37 cm	2.33 (177%)	2.23 (233%)	1.35 (650%)	0.23 (160%)	-1.50 (13%)
Cyl r = 40 cm	1.95 (132%)	1.86 (178%)	1.17 (550%)	0.15 (139%)	-1.19 (11%)
Surface 1 mm	0.82 (2%)	0.65 (3%)	0.15 (17%)	-0.54 (42%)	-1.27 (5%)
Surface 1 cm	0.89 (6%)	0.75 (12%)	0.24 (33%)	-0.36 (5%)	-1.04 (22%)
Surface 5 cm	1.21 (44%)	1.15 (72%)	0.66 (267%)	0.11 (129%)	0.07 (105%)

Table 5.1: Drag Force [N] for different rotational models

The Moving Reference Frame (MRF) approach, when the volume surrounds the wheel, exhibits various trends in two different cases: (1) using a simple cylinder with a width of 26cm with variable diameter and (2) using an extrusion with varying thickness of the ".stl" file representing the disc wheel geometry. It must be reminded that the cylinder volume remains the same during all the simulations at the different yaw angles while the volume obtained through the CAD file rotates according to the yaw angle following the geometry of the wheel.

Analyzing the results at zero angles with respect to the drag force in comparison to the reference case, it is observed that a smaller volume used for the second approach leads to closer results with the Rotating Wall Boundary Condition (RWBC). When using the cylinder, the results are overestimated for all the cases, but increasing the radius of MRF leads to smaller drag forces. The drag force reaches an overestimation of 650% at 10 degrees of yaw angle when simulated with a cylinder of 37 cm of radius. This is caused also because the reference force is very small which leads to a huge error due to the normalization. For the other angles, the volume which performs better is the biggest one. For the $radius = 40cm$ the errors are respectively 132%, 178%, 550%, 139% and 11%. In any case, also the trend changes, postponing the sail effect. For the RWBC simulation, the negative drag can be observed between 10 and 15 degrees while for cylinder MRF it happens between 15 and 20 degrees of yaw angles. It is also interesting to notice that when the drag force becomes negative, its value becomes immediately bigger than the one simulated with RWBC. Another interesting effect of adopting MRF to simulate the rotational effect of the wheel it's the dependency on the thickness of the cylinder. Indeed for the 0 yaw angle, an attempt to optimize the volume of MRF was simulated. For these

cases, the thickness adopted is $11mm$, equal to the thickness of the hub of the lenticular wheel. Even for these simulations, the results are surprisingly different compared to the reference case, but at the same time, the drag value computed is proportional to the thickness. Indeed the respective values are $1.07N$, $1.05N$, and $0.71N$, which are 27%, 25% bigger than the reference case, and 15% smaller for the last case. Hence, also when the thickness of the region of MRF changes, the results are unpredictable. When the radius increases the value are smaller, while when the thickness increases the values become bigger.

Conversely, when the volume is chosen based on the CAD geometry, a different trend is observed. Specifically, when the thickness is only 1mm, the force is almost equal to the reference case, as it is also the case for a thickness of 1cm, while it reaches higher values when the thickness is 5cm. Also for these two cases, the sail effect happens in the same interval and the trend of the forces remains similar to the initial case.

Indeed, similar to the previous scenario where the distance from the wheel was 5, the result is significantly different, overestimating the forces by 44% at 0 yaw angle and by 72%, 267%, 129% and 105%. Moreover, with this setup, the sail effect cannot be appreciated. Indeed the drag force at 20 yaw angle remains positive and the relative error is higher than in the other two cases.

For what concerns the lateral forces, the cylinder cases perform better in terms of relative errors but just because of the bigger initial values which lead to a less severe normalization. Contrary to the drag force, in these cases, the forces are underestimated, especially for the bigger cylinder where the lateral force at 20 yaw angle is surprisingly bigger than the one simulated at 15 degrees. Indeed at 20 yaw angle, the force is almost half of the one calculated for the RWBC. In all the other cases, the errors stay below 31%. Contrary to the drag force, for the lateral ones the volume which performs better is the cylinder with the $radius = 34cm$. Indeed, the errors stay always below 20%, in particular 16%, 13%, 14%, and 20%.

Also in these cases, the smallest MRF volume obtained through the CAD file performs absolutely well, while the other two are able to obtain values that stay below 10% of error. Only the bigger volume simulated at 20 yaw angle underestimates the force of 19%.

Particularly the volume of 1 mm has an average error of 1%, while the 1 cm has some discrepancies at 5 yaw angle (5%) and 20 yaw angle (7%).

Going deeper into the analysis the pressure coefficient is plotted around the wheel. Indeed the pressure coefficient for a yaw angle of 0 degrees is also compared in Figure 5.12. It

Steady State Models - Lateral Force [N] (Percentage Difference compared to reference case)					
angle [°]	0	5	10	15	20
RWBC	0	6.58	13.99	22.25	31.68
Cyl r = 34 cm	0	5.54 (16%)	12.38 (13%)	19.20 (14%)	25.44 (20%)
Cyl r = 37 cm	0	5.27 (20%)	11.45 (18%)	17.23 (23%)	22.85 (28%)
Cyl r = 40 cm	0	4.60 (30%)	9.87 (29%)	15.32 (31%)	15.27 (52%)
Surface 1 mm	0	6.53 (1%)	14.00 (0%)	22.57 (1%)	31.40 (1%)
Surface 1 cm	0	6.28 (5%)	13.92 (1%)	21.40 (4%)	29.53 (7%)
Surface 5 cm	0	6.80 (3%)	15.11 (8%)	22.83 (3%)	25.62 (19%)

Table 5.2: Lateral Force [N] for different rotational models

is noteworthy that the divergence of the plots from the reference case, shown in red, is proportional to the computed value for the drag forces.

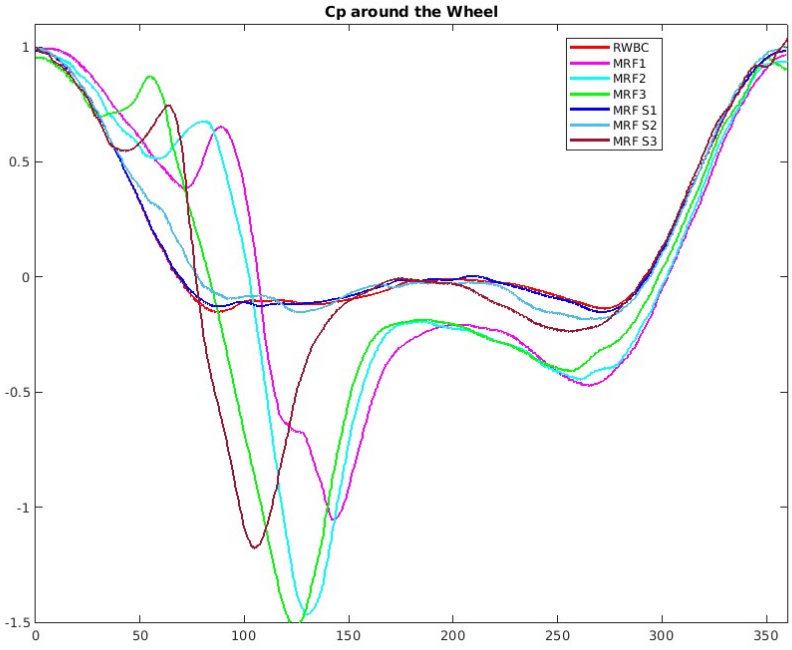

Figure 5.5: C_p profile around the wheel for different steady-state rotational model

The cylinders with a radius of 37 and 40, cm and a surface thickness of 5cm exhibit a pronounced negative peak around 100° and 110°, reaching pressure coefficient (C_p) values exceeding -1. Additionally, a positive peak is observed around 60°. Notably, a significant negative gradient is evident below the wheel. Similarly, the "small" sized cylinder volumes exhibit a comparable pattern characterized by two peaks, one positive and one negative.

However, the positive peak is delayed and occurs approximately at 100°, while the negative peak appears shortly after 150°.

Moreover, for the cylinder cases, the pressure coefficient is underestimated from 90 degrees to 310 degrees. This huge volume of low pressure could be the cause of the higher drag forces computed and shown in the previous table. Contrary the surface cases perform better in the upper region (from 180 degrees to 310 degrees).

Furthermore, for both cases of surface extrusion volume, 1 mm and 1 cm, a good agreement with the reference case is observed, as indicated by the small quantitative difference computed for the drag force. It is also interesting to note that in the second half of the graph, corresponding to the upper part of the wheel, the plots are mostly similar. Several graphical examples are also provided to illustrate how the flux changes between the models. In the next figures, it illustrates the velocity flux on the wheel and on the $y - plane$, while in dark blue is shown the $iso - surface$ for $C_{ptot} = 0$.

In these seven setups, it can be clearly seen how the velocity field varies between every approach. The closer approach with respect to the rotating wall boundary conditions is adopting the minimum thickness for the extrusion of the CAD geometry. Indeed in Fig e for all three cases, the wake and the iso-total pressure surface are similar to the reference case, considering the iso-total pressure plotted as $p_{tot} = 0\ Pa$. Particularly the velocity field and the wake developed behind the wheel are almost the same and very conservative with respect to the other approach where the magnitude, direction, and surface are getting bigger, more complex, and pointing down. For what concerns the cylinder cases, even for the small cylinder, two turbulence wakes are present at the bottom of the wheel, when the gradient of pressure is at its maximum. Also, the low-velocity field behind the body is pointing down, while in the reference case is parallel to the flux. Increasing the volume of the cylinder, hence increasing the diameter, the low-velocity field, and the total pressure iso-surface increases their area of influence. It must be noticed that with this mesh configuration, at the boundary of the moving reference frame and the external mesh, some weird behavior of the flux is observed, especially on the top of the wheel where some area of accelerated flux can be seen.

For the cylinder case, a high-velocity area is developed under the wheel which happens just after a low-velocity area. The velocity field is hard to understand and interpret. For the radius 0.34 and 0.37 at 0 yaw angle a high-velocity region can be seen behind the wheel that decelerates behind the initial velocity on the right of the figures. This high-velocity region is less present when a bigger cylinder is used or when the cad geometry is applied. Indeed, the extrusion of the CAD surface, on the contrary, is more conservative. Only

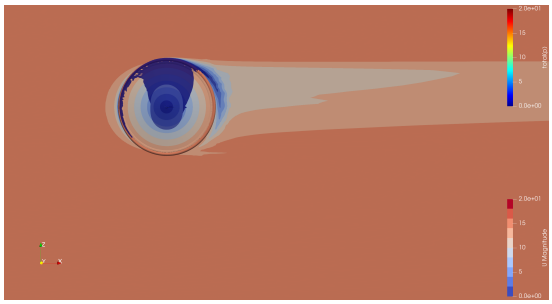

(a) Rotating Wall Boundary Condition

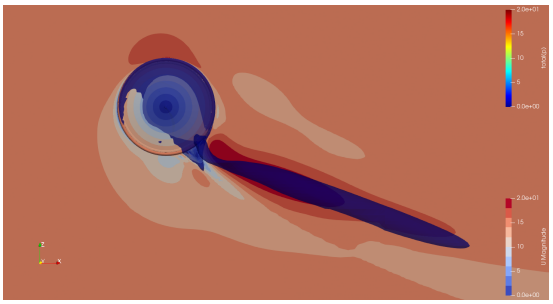

(b) Moving Reference Frame - Cylinder $r = 0.34cm$

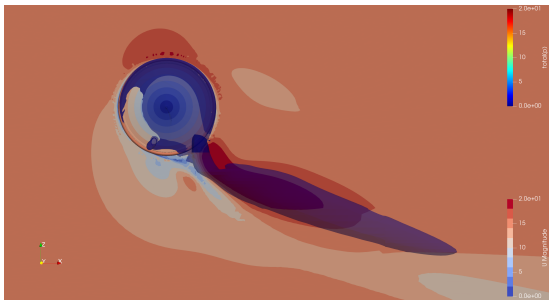

(c) Moving Reference Frame - Cylinder $r = 0.37cm$

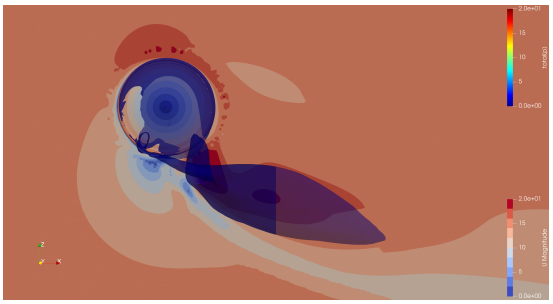

(d) Moving Reference Frame - Cylinder $r = 0.40cm$

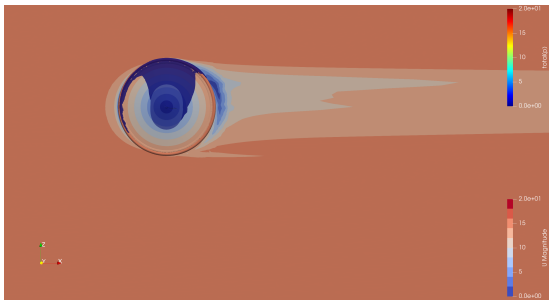

(e) Moving Reference Frame - Surface Extrusion 1 mm

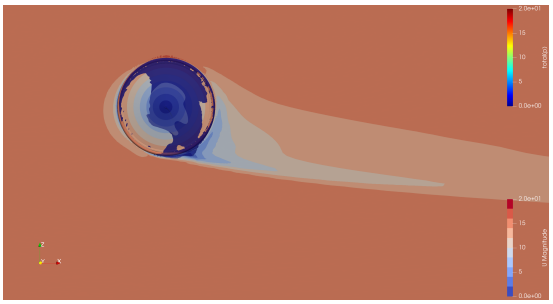

(f) Moving Reference Frame - Surface Extrusion 1 cm

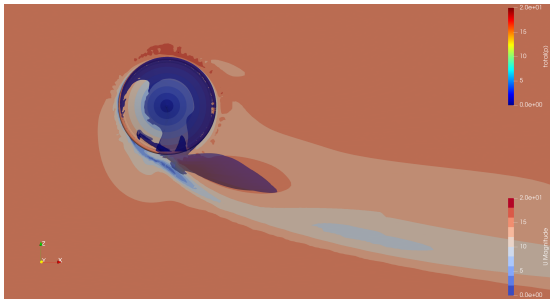

(g) Moving Reference Frame - Surface Extrusion 5 cm

Figure 5.6: Velocity field for different steady rotating models

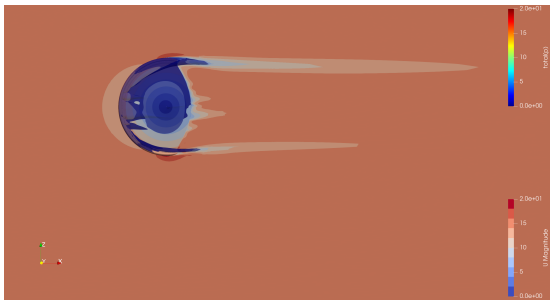

(a) Rotating Wall Boundary Condition

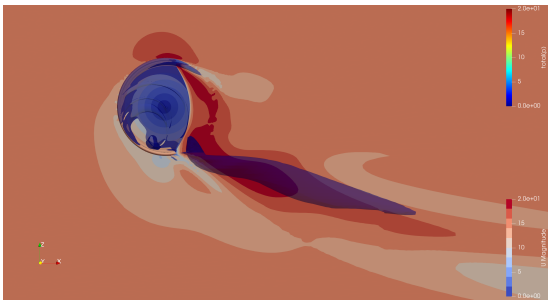

(b) Moving Reference Frame - Cylinder $r = 0.34cm$

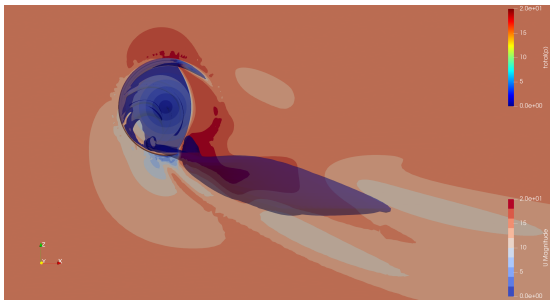

(c) Moving Reference Frame - Cylinder $r = 0.37cm$

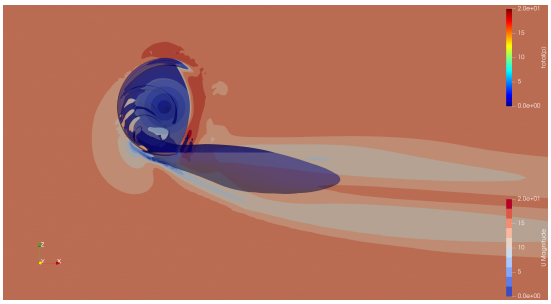

(d) Moving Reference Frame - Cylinder $r = 0.40cm$

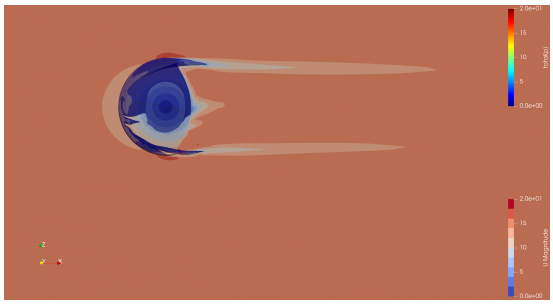

(e) Moving Reference Frame - Surface Extrusion 1 mm

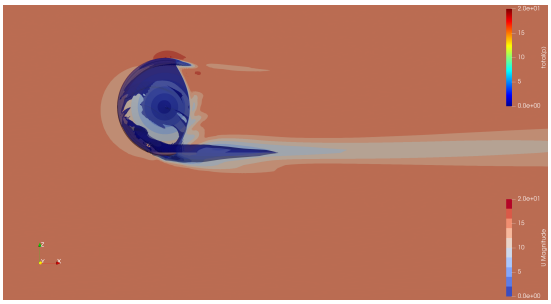

(f) Moving Reference Frame - Surface Extrusion 1 cm

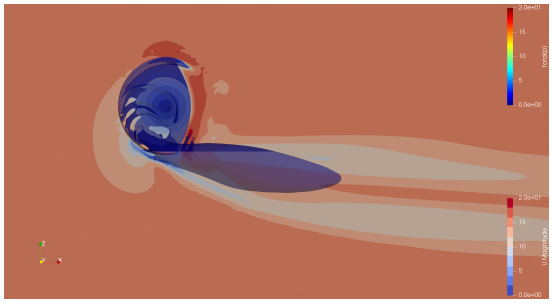

(g) Moving Reference Frame - Surface Extrusion 5 cm

Figure 5.7: Velocity field for different steady rotating models at 10 degrees of yaw angle

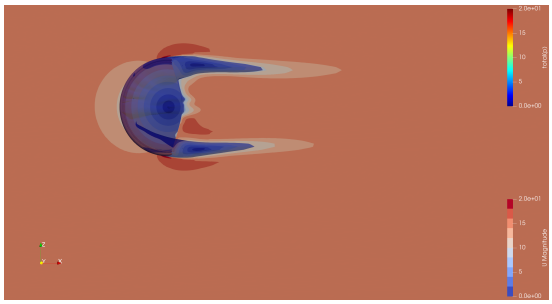

(a) Rotating Wall Boundary Condition

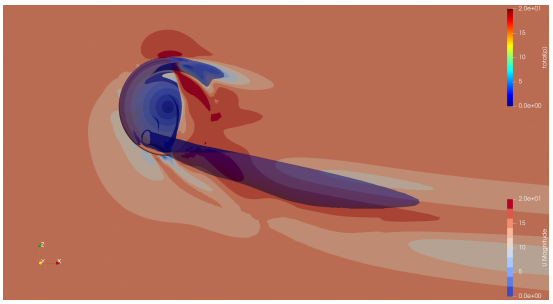

(b) Moving Reference Frame - Cylinder $r = 0.34cm$

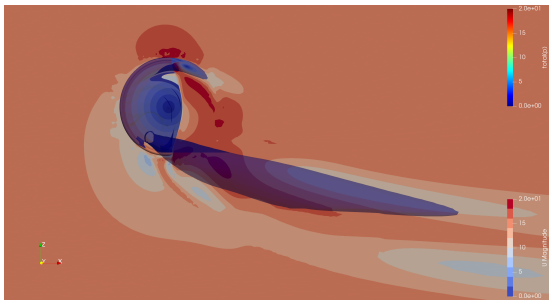

(c) Moving Reference Frame - Cylinder $r = 0.37cm$

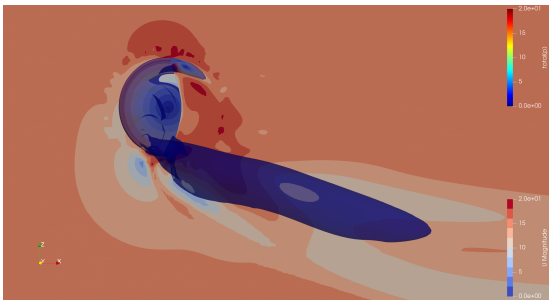

(d) Moving Reference Frame - Cylinder $r = 0.40cm$

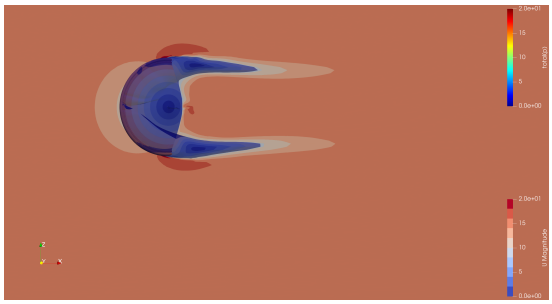

(e) Moving Reference Frame - Surface Extrusion 1 mm

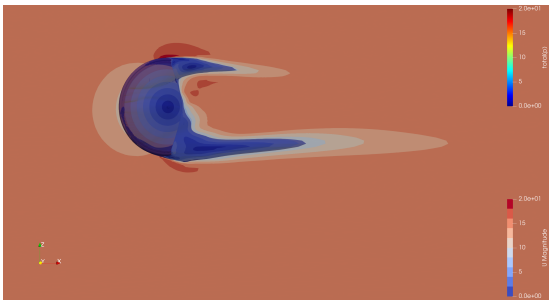

(f) Moving Reference Frame - Surface Extrusion 1 cm

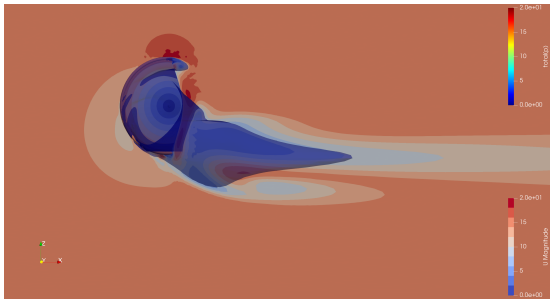

(g) Moving Reference Frame - Surface Extrusion 5 cm

Figure 5.8: Velocity field for different steady rotating models at 20 degrees of yaw angle

in the last case, the big wakes and the deflection of the flux are created, but the trend is demonstrated also by the medium thickness case where the iso-surface is still attached to the wheel, but the flux starts to be deflected to the bottom. It must be noticed that with these configurations the high-velocity region depicted in red is not present. These observations are similar even for the case at 10 yaw angle and 20 yaw angle. The flux developed on the y-plane is different but the evolution of the velocity field is similar to the previous scenario.

For the cylinder cases can be found again the red region and huge wake are visible through the blue surfaces. Also, in the last big cylinder region the red region is less spread than in the other two. The volume in Fig g develops similar features to the cylinder adopted in Fig d, while f is getting closer to the reference case but not in the same effective way as adopting the minimum surface extrusion as in case e. Briefly commenting on the last case, it can be noticed that cases a and e are almost identical while b and c develop similar fluxes behind with high-velocity area and huge wake visible not only through the iso-surface but also through the evolution of the velocity field. In this case, some big differences are present between the adoption of huge volumes of MRF. Indeed the iso-surfaces between cases d and g are very different, particularly in g the trend of the flux of pointing down is not present.

Comparison with aeroCloud

In this section, a comparison between the results obtained through the platform AeroCloud is explained. In the two tables, the numerical results of the drag force and lateral force at different yaw angles are shown. Starting from the drag force, the two software are able to predict with limited error the case for 0 and 5 yaw angles while the forces diverge for bigger angles. Especially even at 10 degrees the drag force becomes negative.

The differences can be explained by the two different approaches used to simulate the yaw angles. In OpenFOAM, the yaw angle is created by rotating the geometry while the boundary conditions remain constant as it can be shown in the previous figures where from the y-plane only a section of the entire geometry is visible, while in AeroCloud as explained in the previous paragraph the rotation is given by deviating the inlet flux the surface sees, as graphically explained by the streamlines in the next figures. Hence at bigger angles, the different methods become remarkable and the forces simulated vary. The same different setup leads to an overestimation of what concerns the lateral forces. Indeed the errors stay limited under the 20% but in every case, the forces are bigger with respect to reference one.

Steady State Models - Drag Force [N] (Percentage Difference compared to reference case)					
angle [°]	0	5	10	15	20
RWBC	0.84	0.67	0.18	-0.38	-1.33
AeroCloud	0.89 (6%)	0.61 (9%)	-0.17 (194%)	-1.01 (165%)	-1.87 (41%)

Steady State Models - Lateral Force [N] (Percentage Difference compared to reference case)					
angle [°]	0	5	10	15	20
RWBC	0	6.58	13.99	22.25	31.68
AeroCloud	0	7.51 (14%)	16.67 (19%)	25.86 (16%)	35.95 (13%)

One of the advantages of using AeroCloud is the simplicity to implement a simulation and the powerful postprocessing tool that offers. In the following figures can be appreciated the flux streamlines that characterized the velocity field ad different yaw angles. From the second view, the one which sees the wheel from the top, it is clear how the yaw angle is simulated. With this software, the flux is deviated while the geometry remains parallel to the x direction.

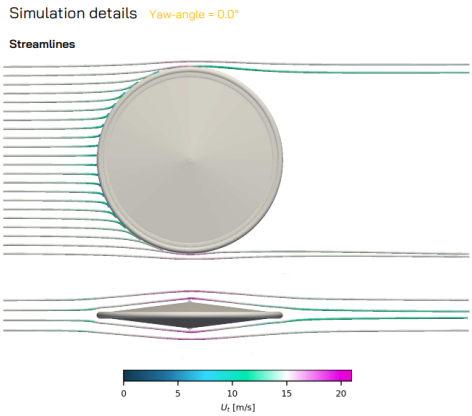

(a) 0 yaw angle

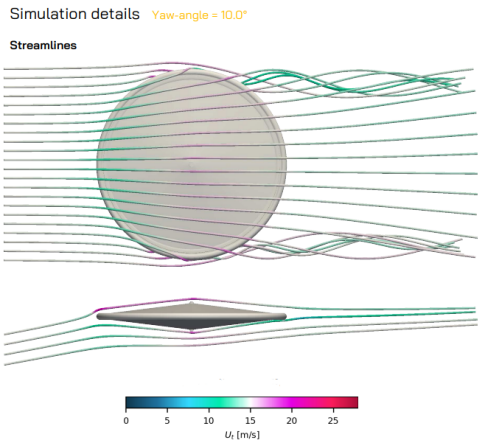

(b) 10 yaw angle

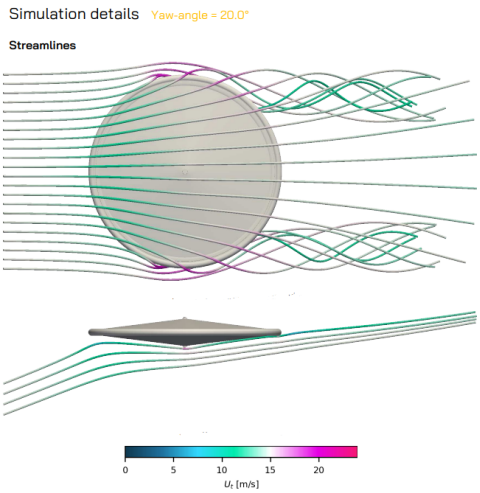

(c) 20 yaw angle

Figure 5.9: Velocity streamlines at different yaw angles

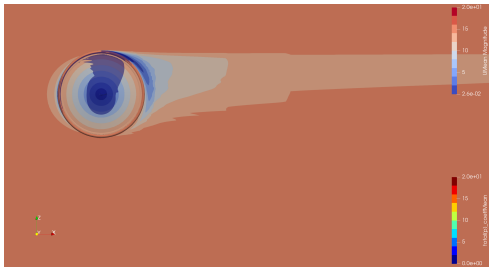

(a) 0 yaw angle

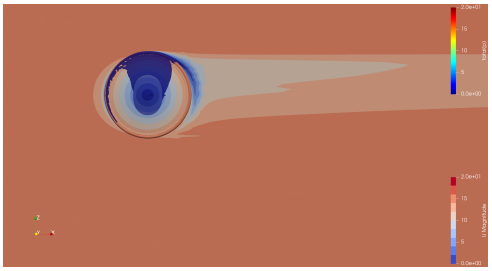

(b) 0 yaw angle

(c) 0 yaw angle

(d) 0 yaw angle

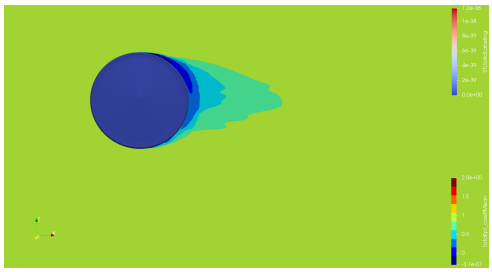

(e) 10 yaw angle

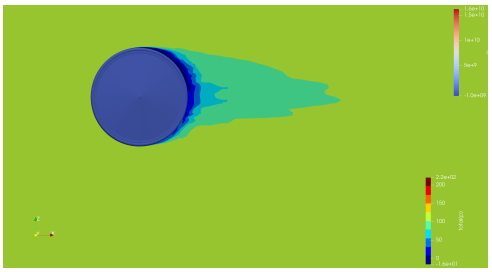

(f) 10 yaw angle

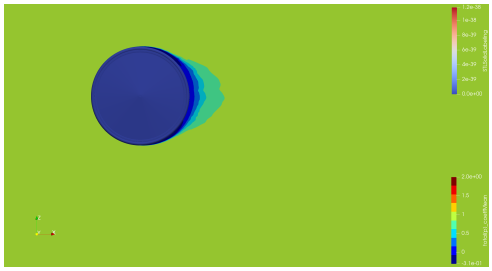

(g) 20 yaw angle

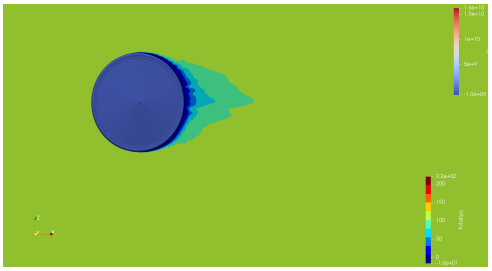

(h) 20 yaw angle

Figure 5.10: C_{ptot} and Velocity field compared between the two softwares

In the images is possible to highlight that at 0 yaw angle, the velocity flux is almost identical, while the total pressure coefficient C_{ptot} shows more negative values but a smaller wake. This trend of the pressure is evident also in the cases at 10 and 20 yaw angle where the wake of the RWBC is bigger than the one of AeroCloud. It must be underlined again that for the yaw angle cases, the angle of attack is simulated in two different ways and it could be the reason behind the difference. However, the two simulations share a flux way similar to the one simulated by the MRF.

5.1.2. Unsteady Models

For these cases, the unsteady solver *pimpleFoam* for incompressible flow available in OpenFoam is used. The results are root mean squared for the last two rotations as described in the previous chapter.

DDES Case

This experimental setup aims to provide a comparative analysis of turbulence modeling by adopting an alternative approach to solving turbulence within a rotational model. In this study, the Delayed Detached Eddy Simulation (DDES) method is employed to account for turbulence effects, while the Multiple Reference Frame (MRF) volume method is utilized to simulate rotation. The MRF volume is specifically configured to represent a lenticular wheel with a thickness of 1 mm.

In the current case, the drag force is determined by averaging the measurements obtained from the last two complete rotations. The resulting drag force is found to be 1.04 N, which is 24% higher than the reference case. This disparity can be attributed to the choice of turbulence model as well as the limitations of the mesh utilized in this computationally intensive method. Notably, the present simulation employs wall functions for the calculation of boundary layers and shear forces, as opposed to resolving them explicitly.

It must be highlighted that at a yaw angle of 0 degrees, the drag force is evenly distributed between pressure and viscous forces. Specifically, in this setup, viscous forces contribute to 60% of the total drag force. Therefore, given the extensive surface area, a more comprehensive analysis employing DDES could be performed by increasing the number of elements and incorporating additional layers, as demonstrated in previous cases.

The objective of this simulation is twofold: to achieve a higher level of accuracy in force magnitude estimation and to serve as an initial implementation of the DDES turbulence model in the OpenFOAM software. The obtained results exhibit promising trends, warranting further investigation and validation of this model.

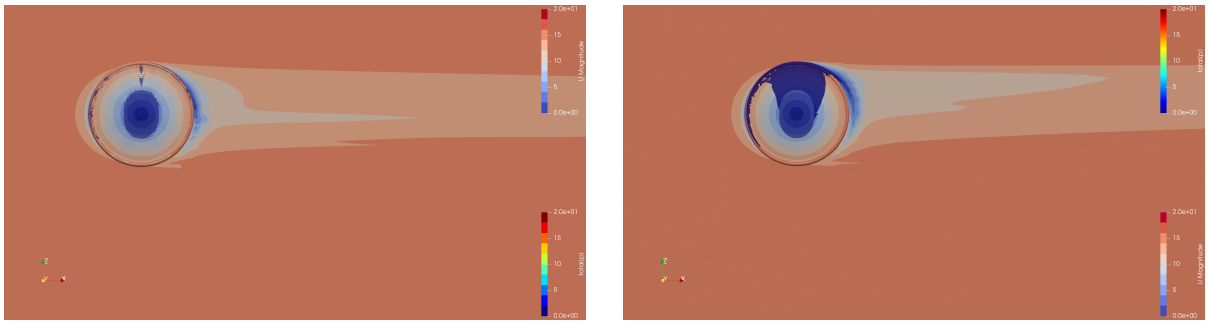

(a) DDES (b) RWBC

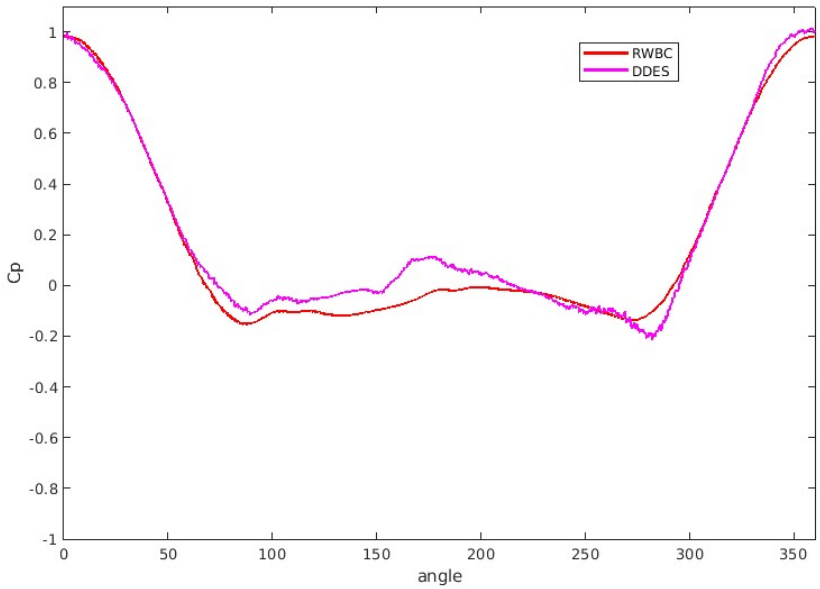

Figure 5.12: C_p profile around the wheel for DDES and RWBC

Even if the drag force value shows some discrepancies the C_p plot confirms the trend of the pressure around the wheel computed by RWBC. Even in this case, a negative peak is present at 90° and also at the top (270°). The value of the coefficient remains in all the angles very close to the one calculated by RWBC.

Sliding Mesh

The sliding mesh rotational method certainly increases the computational efforts required for the simulation. Indeed, it requires an unsteady solver, *pimpleFoam*, to simulate the rotation of the wheel. At each time step the mesh which contains the wheel moves inside the domain to simulate its rotation. The virtual simulation time is 1 s, which corresponds to seven full rotations of the wheel, but the results are obtained by applying the root mean square definition on the last two full rotations. The computed results compared to the reference case are shown in the next tables. Even for this case the drag forces and lateral forces are compared and the relative errors are in the brackets.

Steady State Models - Drag Force [N] (Percentage Difference compared to reference case)					
angle [°]	0	5	10	15	20
RWBC	0.84	0.67	0.18	-0.38	-1.33
SM	0.64 (24%)	0.52 (22%)	-0.21 (216%)	-0.88 (131%)	-1.55 (17%)

Steady State Models - Lateral Force [N] (Percentage Difference compared to reference case)					
angle [°]	0	5	10	15	20
RWBC	0	6.58	13.99	22.25	31.68
SM	0	4.54 (31%)	10.01 (28%)	18.23 (18%)	24.14 (24%)

The quantitative results underestimate in all the cases the value computed by RWBC. In particular, the reason associated is the different boundary conditions that aim to substitute the rotation of the geometry. Unfortunately, OpenFOAM is not able to build enough qualitative mesh to compute the rotation of the geometry maintaining stable the simulation. Apparently, when the geometry remains perpendicular to the x-axis and the inlet velocity direction changes, the impact of the wind is less severe which leads to smaller forces in the side direction. Also in this case must be underlined that the drag becomes negative between the 5 to 10 yaw angle, similar to the case of AeroCloud which shares the same setup in terms of boundary condition.

Unfortunately, because of the unsteadiness of the methods, an average plot of the pressure coefficient around the wheel is not possible. Indeed the cells are attached to the wheel and at every time step they change the angle position with respect to the absolute reference

system. In order to compare, at least qualitatively the pressure coefficient around the wheel, the coefficient is plotted and compared to the reference case at different time steps. Particularly they are chosen randomly to cover three different possible scenarios.

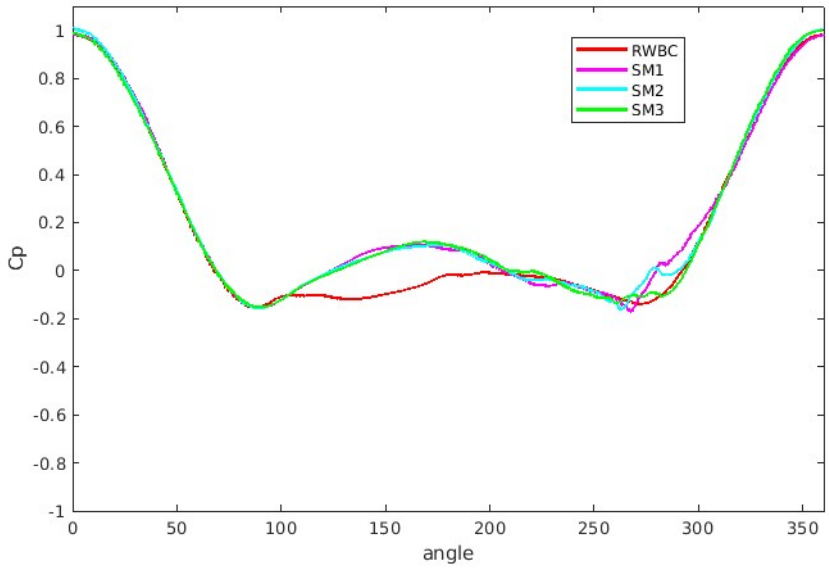

Figure 5.13: C_p profile around the wheel at different time steps

It must be noticed from the figure that the C_p even in this model does not have peaks like with MRF approaches. Indeed, from 0 to 100 degrees, the profiles are almost identical between the models. The sliding mesh approach at every time step has less re-circulation or detachment of the flux behind the wheel. The value of the coefficient between 100 to 200, is above the reference case. This trend can be linked to the lower force calculated on the x-axis between the two rotational models. For what concerns the other front trend of the coefficient, when it goes from 270 to 360 degrees, the curves overlap again.

Also, these time steps are compared qualitatively looking at the velocity field and iso-surface of total pressure at different yaw angles.

At this point also the flux at 0, 10, and 20 around the wheel is shown graphically in the next figures:

Also for this case, the Sliding Mesh simulates the rotation in a similar way to the one adopted by AeroCloud. The inlet velocity is not anymore parallel but a component on the y direction is added to have the same angle of attack.

At 0 yaw angle, the wake of obtain thanks to the SM approach is limited with respect to the RWBC. Also, the $iso - surface$ obtained when the total pressure is equal to 0 has a

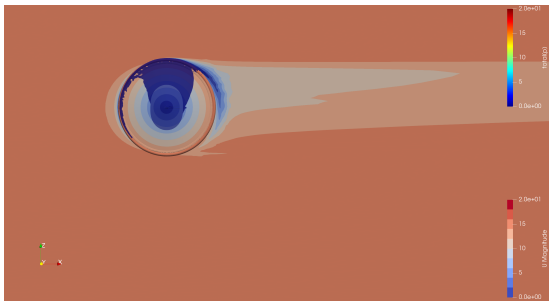

(a) Rotating Wall Boundary Condition

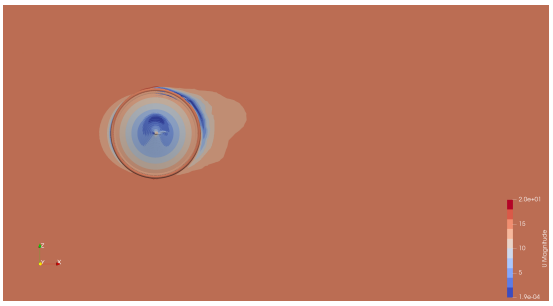

(b) Sliding Mesh

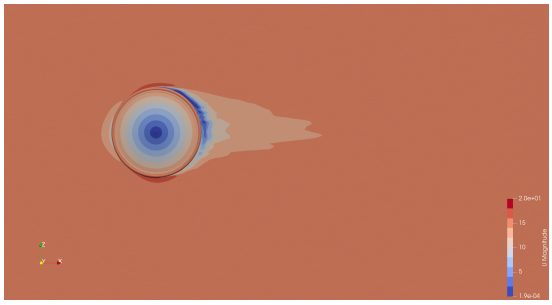

(c) Rotating Wall Boundary Condition at 10°

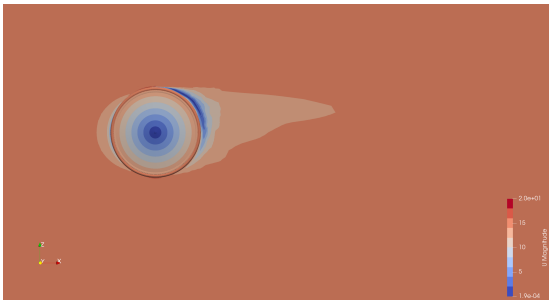

(d) Sliding Mesh at 10°

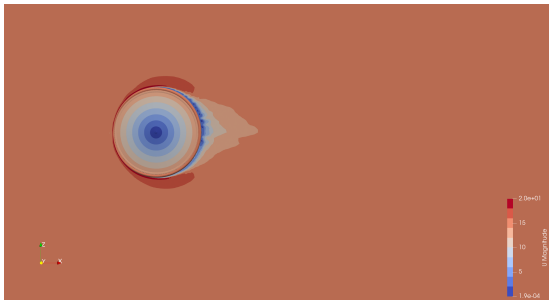

(e) Rotating Wall Boundary Condition at 20°

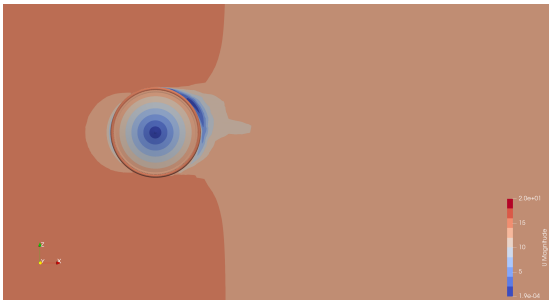

(f) Sliding Mesh at 20°

Figure 5.14: Velocity field for different steady rotating models at 20 degrees of yaw angle

smaller influence. This demonstrates also the smaller force computed by this approach.

Increasing the yaw angle, the two figures become similar. At 10° must be noticed that the plotted plane for RWBC is not the y-plane but the plane normal to the disc wheel. Indeed the wheel for RWBC is rotated by 10 deg, hence also the plane in the fig is rotated by 10 deg. The new plane indeed should represent the zone behind the wheel that is no anymore parallel to the flux but parallel to the axis of rotation of the wheel. In this case, the two wake are closer than the previous one, even if the difference could be given by the different approach to simulating the rotation of the geometry which for what concern the SM is not possible to compute moving the geometry inside the domain because moving the geometry decreases the quality of the mesh, so the computation becomes less stable and also more time-consuming.

The same approach and configuration are used to show the discrepancies at 20° of yaw angle. In this case, the different boundary conditions have a higher impact on the overall flux. However, if the focus is given only to the wake behind the disc wheel the flux structure becomes similar. Indeed is present a low-velocity zone, which is predominant on the upper part of the back of the wheel, and the wake is almost symmetrical with respect to the x-axis. Also, the zone of interest of the lower velocity with respect to the initial condition covers the same area behind the wheel.

Considering these considerations, the results of RWBC, which decreases the computational time, are straightforward for the CFD analysis for what concern the disc wheel. Moreover, the MRF case obtained from the extrusion of the disc wheel file of only 1 mm shows significant results in terms of estimation of the flux, forces, and computational time.

5.2. Spoked Wheel

In this section, the results of the spoked wheel are analyzed starting from the steady solver to finishing with the unsteady algorithm.

5.2.1. Steady Models

Even for the spoked wheel, the rotating wall velocity boundary condition (RWBC) case is used as a reference case for the sake of simplicity and to have a symmetry case to be compared with the previous results, even if theoretically speaking, this choice does not represent the real phenomena as demonstrated by Hokeicka in his study [17] where the presence of the spokes which are not obtained from a solid of revolution decrease the effectiveness of this approach.

Hence, before starting the methods comparison the RWBC solution is analyzed and described for the different yaw angles. The first figure 5.15 shows the drag force in the wheel direction and the side force in the lateral direction with respect to the wheel. The side force starts from zero value because of the symmetry of the problem, while it increases due to the rim surface of the wheel which shows a different slope compared to the lenticular wheel. Moreover, in this case, the wheel analyzed has a low profile rim, which is suitable to have a lightweight wheel for the climbing stage or an entry-level wheel for amateurs cyclists. Indeed, the maximum lateral force obtained at 20 degrees is six times lower than the one generated by the other wheel.

The drag force shows another trend. It continuously increases as the yaw angle increases. Indeed the lateral forces help to decrease the drag force, but in this case, due to the low profile rim, they are not able to counterbalance the increment of the drag force.

To better explain the different forces acting on the wheel, the pressure coefficient is plotted in Fig. 5.16. Figure 5.2 illustrates the distribution of the pressure coefficient (C_p) along the center line of the wheel. The graph demonstrates the evolution of the C_p profile at various yaw angles. A C_p value of one is associated with stagnating flow, and it is found around 0° for the wheel with 0 yaw angle, while it decreases when the yaw angle increases because the stagnation point moves to the upper surface of the tire.

With increasing θ, C_p decreases until it reaches the lowest point around 90 for the red case, which means under the wheel. For the other yaw angles, it moves forward because the depression caused by the rim surface has a higher impact with respect to the rotation. Notably, at the rear of the wheel (at 180°), the coefficient remains constant and equal to

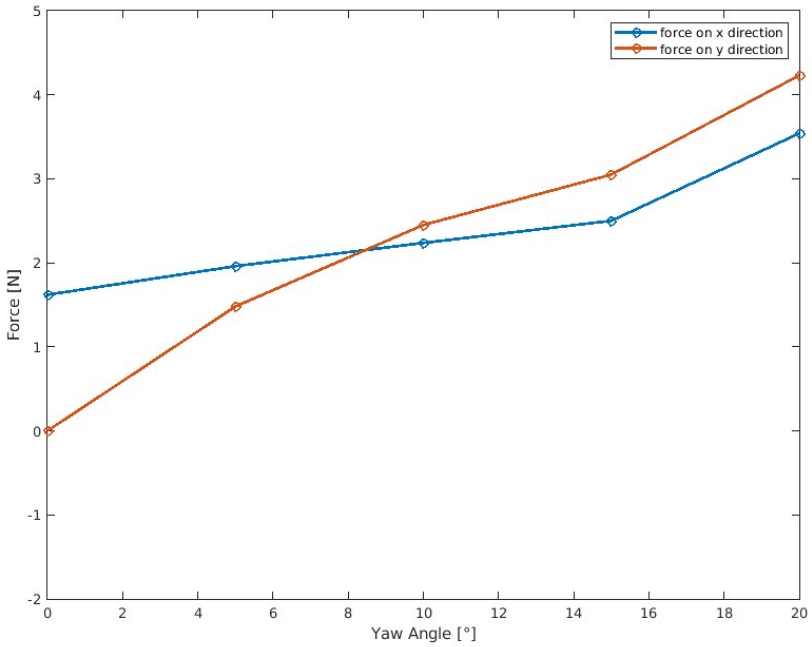

Figure 5.15: Forces on drag and lateral directions at different yaw angles.

zero which is linked to the separation flow region. For the case with 20° of way angle the presence of the spokes generates a very low-pressure zone due to the high turbulence that creates.

Moreover, at 270°, which is the top of the wheel, the pressure is influenced again by the presence of the rim, and the separation points may occur and the total pressure value assumes values around 0. For the other cases, the low-pressure zone expands as the yaw angle increases.

Graphically speaking, the wake and the separation zones are estimated showing the C_p on the back side of the wheel and using as $iso-surface\ C_{ptot} = 0$. Hence, the $iso-surface$ shows the same trend and increases its influence according to the yaw angle. At 20° the complex iso surface structures are visible and they can be linked to the unsteady value of the pressure behind the wheel plotted in the previous graph.

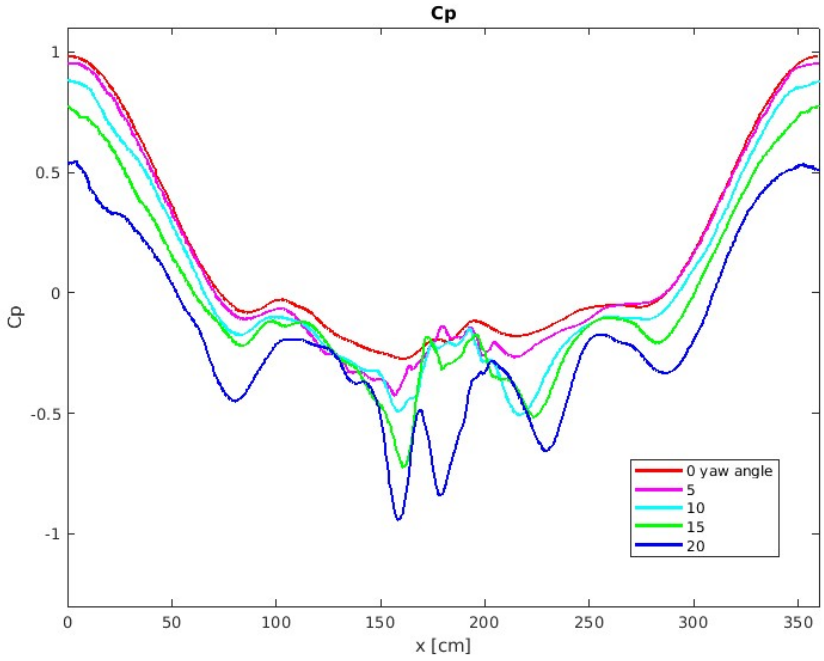

Figure 5.16: C_p profile around the wheel at different yaw angles

H

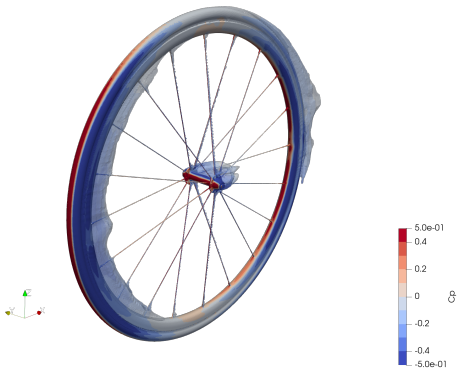

(a) 0 yaw angle

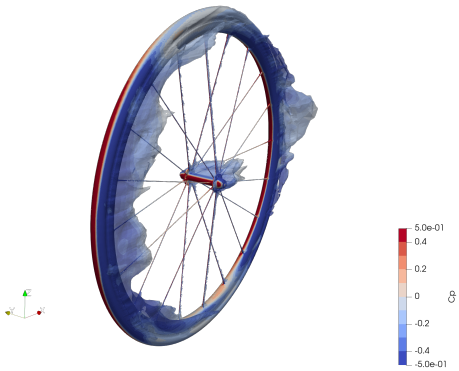

(b) 10 yaw angle

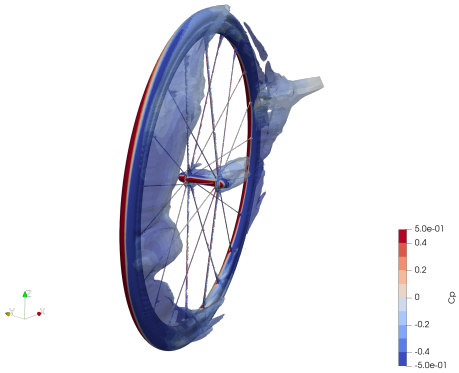

(c) 20 yaw angle

Figure 5.17: View of the low-pressure side of the wheel

MRF Analysis

This paragraph examines an analysis of the moving reference frame cases, using the RWBC that was the subject of the previous paragraph's analysis as a reference case.

First of all the drag and lateral forces are compared for the different yaw angles. All the computed values are shown in the table 5.3 and 5.4:

Steady State Models - Drag Force [N] (Percentage Difference compared to reference case)					
angle [°]	0	5	10	15	20
RWBC	1.62	1.96	2.24	2.50	2.54
Cyl r = 34 cm	1.70 (5%)	1.92 (2%)	2.19 (2%)	2.55 (2%)	1.93 (24%)
Cyl r = 37 cm	1.76 (9%)	1.82 (7%)	2.13 (5%)	2.34 (6%)	2.22 (13%)
Cyl r = 40 cm	1.67 (3%)	1.84 (6%)	1.95 (13%)	2.05 (18%)	1.94 (24%)
Surface 1 mm	1.69 (4%)	2.00 (2%)	2.21 (1%)	2.43 (3%)	2.50 (5%)
Surface 1 cm	1.75 (8%)	1.87 (5%)	2.17 (3%)	2.43 (3%)	2.24 (12%)
Surface 5 cm	1.38 (15%)	1.66 (15%)	2.28 (2%)	2.61 (4%)	2.74 (8%)
MRFg	1.70 (5%)	1.82 (7%)	2.04 (9%)	2.45 (2%)	2.06 (19%)
MRFspokes	1.72 (6%)	1.97 (1%)	2.32 (3%)	2.34 (6%)	2.22 (13%)

Table 5.3: Drag Force [N] for different rotational models

Also for the spoked wheel, some tendencies should be highlighted, depending on the MRF method chosen: so when the MRF is created with a cylinder of 26 mm, emphasizing that in this case the position of the volume position remains constant, or when the MRF volume is the extrusion of the ".stl" file which is able to cover all the spokes of the wheel. For the spoked wheel, there are also two new approaches: the hybrid approach called MRFg, where the MRF is applied only to the spokes thanks to a frustoconical volume, and the RWBC on the rim and the MRFspokes, which no longer uses as volume for the MRF the file of the disc wheel CAD, but that of the spoked wheel ones. In the last case, the volume is no longer obtained by a rotation body, but directly from the spokes and the rim.

Analyzing the results no specific correlation can be found. Starting with the cylinder case, the relative errors are lower concerning the disc wheel. In particular, the bigger the volume lower the force evaluated in the drag direction. This behavior is linked to the fact that with a bigger MRF setup, the lateral forces, as analyzed later, increase, hence the drag force benefits of this trend. Indeed, at 20 yaw angle, due to the higher effect

of the lateral force, the drag force decreased, contrary to the RWBC where the forces continuously increase.

The relative error, for this case, remains quite low. Only at 20 yaw angle reaches values of 24%, 13%, and 24% for the case of 34, 37, and 40 cm. However, when the cylinder considered is with a radius of 40 cm the error becomes consistent even when the yaw angle is 10 deg.

Even for this case, the results depend on the thickness of the cylinder, indeed when the cylinder is only 11 cm thick, the drag force at 0 yaw angle is 1.44, 1.49, and 1.48 which are 23% lower than the reference case.

When the volume is chosen through the extrusion of the CAD, only when the thickness is 1 mm and 5 cm the drag force continuously increases, for the other cases, the drop at 20 yaw angle is present. Indeed with 1 mm the relative error remains under 5%. When the thickness is 1 cm only at 20 yaw angle the error becomes significant. Only with the biggest volume the force are very underestimated at 0 and 5 yaw angles, while since the 10 yaw angle, the forces are overestimated but the growth trend is present.

The analysis of the last two approaches remains similar. Even for this case, the relative errors remain under the 10%, only at 20 yaw angles the drop of the force is present which leads to an error of 19% for the hybrid model and of 13% for the spokes one.

Steady State Models - Lateral Force [N] (Percentage Difference compared to reference case)					
angle [°]	0	5	10	15	20
RWBC	0	1.48	2.45	3.05	4.23
Cyl r = 34 cm	0	1.91 (29%)	3.17 (29%)	3.29 (8%)	6.76 (60%)
Cyl r = 37 cm	0	2.13 (44%)	2.24 (9%)	3.49 (14%)	6.47 (53%)
Cyl r = 40 cm	0	1.61 (9%)	2.40 (2%)	4.32 (42%)	5.47 (29%)
Surface 1 mm	0	1.34 (9%)	2.57 (5%)	3.54 (1%)	4.58 (8%)
Surface 1 cm	0	1.78 (20%)	2.72 (11%)	3.48 (4%)	4.94 (17%)
Surface 5 cm	0	1.73 (17%)	3.43 (40%)	4.76 (44%)	6.60 (56%)
MRFg	0	1.61 (9%)	3.53 (44%)	3.92 (60%)	6.97 (64%)
MRFspokes	0	1.68 (14%)	3.48 (42%)	3.94 (61%)	5.10 (21%)

Table 5.4: Lateral Force [N] for different rotational models

For what concerns the lateral forces, the estimation of the forces shows different results.

Starting from the cylinder cases, the forces are always overestimated, especially at 20 yaw angle where the relative error reaches 60%. The case of 40 cm performs better, indeed the relative error for the different yaw angles is closer to the RWBC results, and only at 15 and 20 yaw angles, the estimation diverges and the error is consistent around 42% and 29% respectively.

Even for the lateral case, the 1 mm extrusion setup maintains a relative error below 10%. The order of magnitude of the forces are comparable to RWBC, indeed in this case the drop of the drag force at 20 yaw angle is not present in the previous table. Also at 1 cm the simulation of the force confirms the order of magnitude, even if at 5 yaw angle and 20 yaw angle the calculated value is quite higher leading to an error of 20% and 17% respectively. For the last case, when the extrusion is 5 cm the lateral forces are always higher and the values show a relative error significant and stable over the 17% with peaks of 56%.

The last two models also show the overestimation trend, even if the last one so when the spokes are used for the MRF volume the errors remain lower. For these last two setups, the error at 10 yaw angle is very consistent. Visualizing the flow could explain this result.

Going deeper into the analysis the pressure coefficient is plotted around the wheel. Indeed the pressure coefficient for a yaw angle of 0 degrees is also compared in Figure 5.18. It is noteworthy that the divergence of the plots from the reference case, shown in red, is proportional to the computed value for the drag forces.

Even if at 0 yaw angle the relative errors are less severe than in the lenticular wheel case the pressure coefficient plot shows very different pressure profiles. Indeed the reference case is the red ones which represent the RWBC. The divergences from the red curves increase according to the volume used. The light green curve and dark red ones represent the cylinder with 40 cm of radius and the surface with the maximum thickness, while the light blue and the purple ones represent the other two cylinder cases. For these curves, it can be noticed one pressure peak is around 90° and one negative pressure peak in the back of the wheel, is around 120/150°. In between a very steep negative gradient is present which can lead to a very severe detachment of the flow according to these simulations. The hybrid model and the surface of 1 cm show a positive peak around 100° but it assumes the value of 0.2/0.3 and then they have a plateau until the top of the wheel, so until 270° when the pressure coefficient goes again to 1.

For the cases, RWBC, the surface of 1 mm, and extrusion of the spokes, the pressure profile are very similar. They do not show any peak in the first quarter of the graph, then the value assets around 0, slowly increasing until 270° when it starts to increase until it

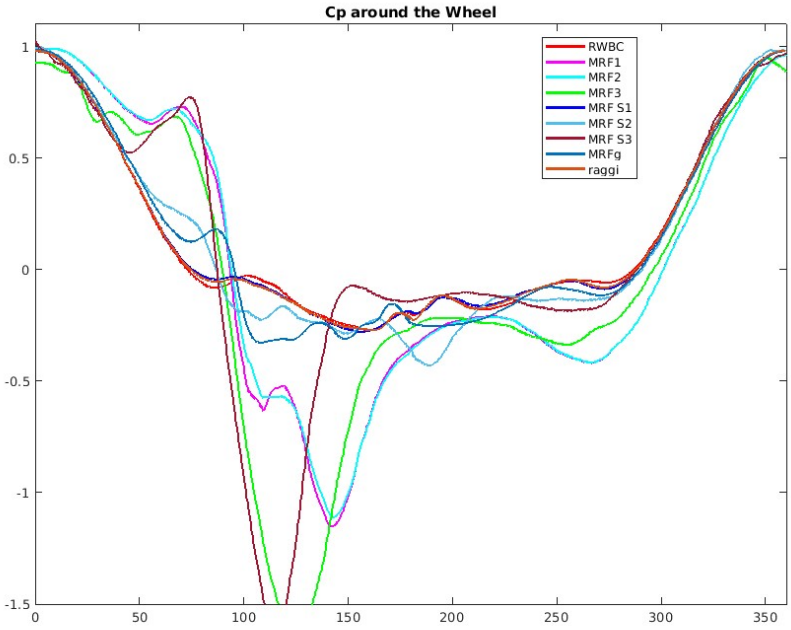

Figure 5.18: C_p profile around the wheel at different yaw angles

reaches again 1 at 360°.

Qualitatively speaking, this graph demonstrates that the small thickness of extrusion as well as adopting the spokes as starting point to choose the volume where applying MRF leads to a good simulation for this application. The last comparison to understand the performance of the models also at different yaw angles is made by showing the velocity flux on the wheel and on the $y-plane$, as well as $iso-pressure\ surfaces$ which represents when the total pressure is equal to one. The figures are made for the cases of 0 yaw angle, 10 yaw angle, and 20 yaw angle.

The qualitative comparison of the flow for these nine setups shows that the velocity field and the $iso-pressure$ surfaces vary between the different approaches.

During the validation analysis, the surface extrusion of 1 mm was able to catch the important characteristic of the flow and also the value computed. Starting from this case it can be noted that only the RWBC and the last approach can show iso pressure surface and velocity field close to the MRF surface approach of 1 mm. The wake is also similar which has a low-velocity area behind in the upper half behind the rim and it decreases its intensity in the lower half. These approaches are also more conservative in terms of the quality of the velocity field and they do not show the complex structures which are created in the other cases. In particular, for the cylinder cases, when the MRF is bigger,

more complex and bigger $iso - pressure$ surfaces are present and the velocity field is pointing down. The same behavior is present for the biggest surface extrusion MRF case. While for the case extruded of 1 cm and for the hybrid case the iso pressure surface cover only the rim and the spokes as in the reference cases, while the flow starts pointing down creating a low-velocity area on the lower half of the rim. Also, as already highlighted in the disc wheel, the MRF in cases c,d, and g creates some weird flow features on the upper part of the rim where an area of accelerated flow can be seen.

The same trend is confirmed at 10 and 20-yaw angles. Cases a, e, and i show similar iso pressure and velocity field, even if for the MRF setup the flow is slightly pointing down, but even inside the spokes the flow shows the same characteristic for these cases. The MRF cylinder cases show very different iso pressure surfaces but in all the approaches the flow is very compromised, indeed very low-velocity zone close to high-velocity ones are present in the lower half behind the wheel.

The only difference here is given by the surface of 5 cm and by the hybrid model. For what concerns case g the iso pressure and the flow are less distorted compared to the cylinder case MRF approaches, while the hybrid model has a significant impact on the velocity field which also creates an $iso - pressure$ surface bigger than other cases.

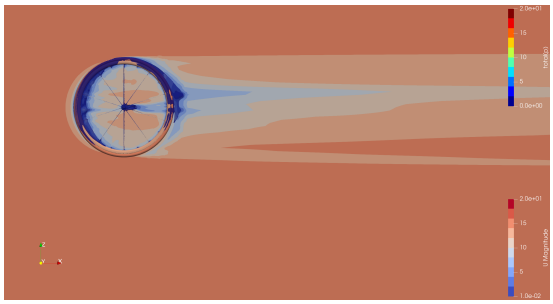

(a) Rotating Wall Boundary Condition

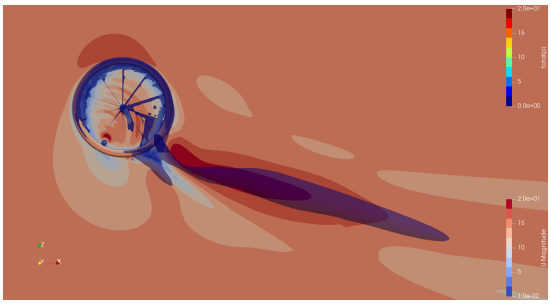

(b) Moving Reference Frame - Cylinder $r = 0.34cm$

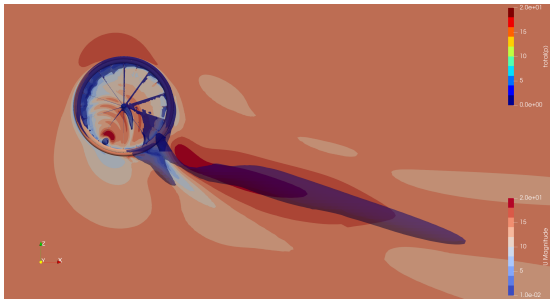

(c) Moving Reference Frame - Cylinder $r = 0.37cm$

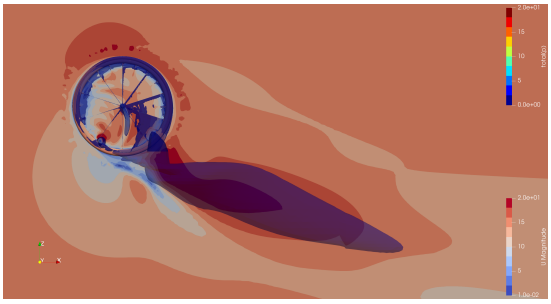

(d) Moving Reference Frame - Cylinder $r = 0.40cm$

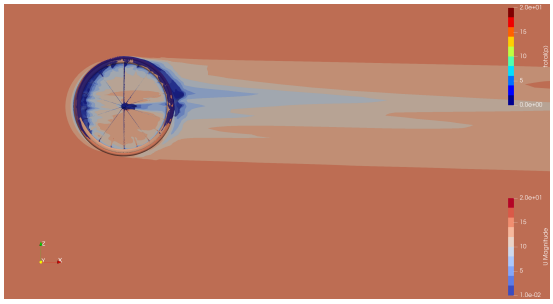

(e) Moving Reference Frame - Surface Extrusion 1 mm

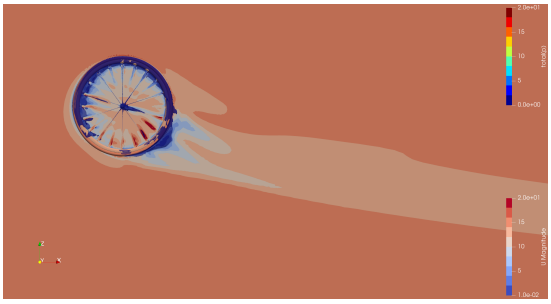

(f) Moving Reference Frame - Surface Extrusion 1 cm

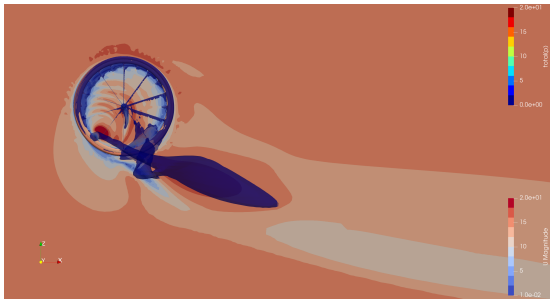

(g) Moving Reference Frame - Surface Extrusion 5 cm

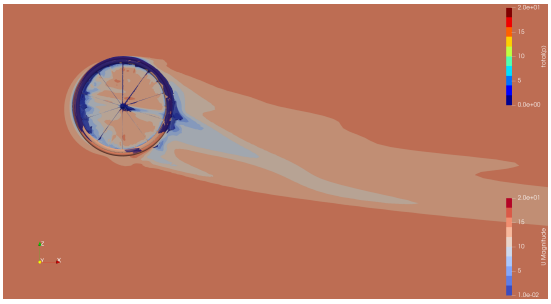

(h) Moving Reference Frame - Hybrid Model

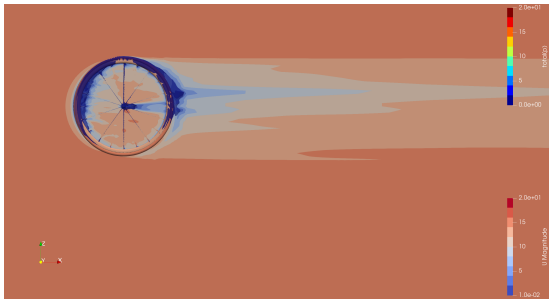

(i) Moving Reference Frame - Surface Extrusion Spokes

Figure 5.19: Velocity field for different steady rotating models for the spoked wheel

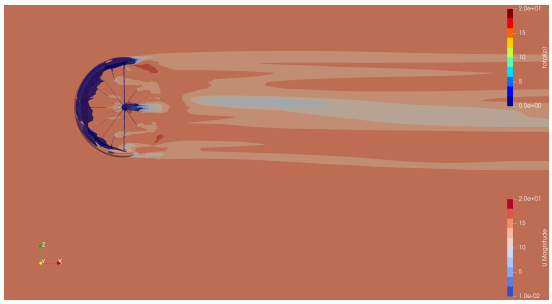

(a) Rotating Wall Boundary Condition

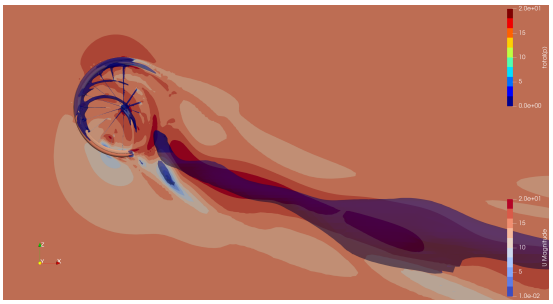

(b) Moving Reference Frame - Cylinder $r = 0.34cm$

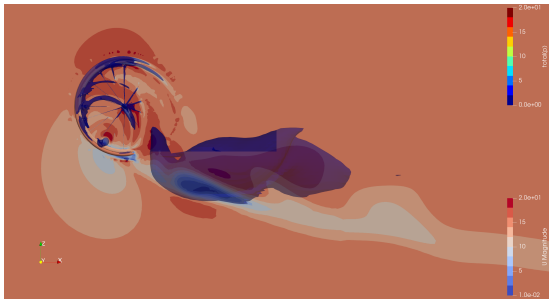

(c) Moving Reference Frame - Cylinder $r = 0.37cm$

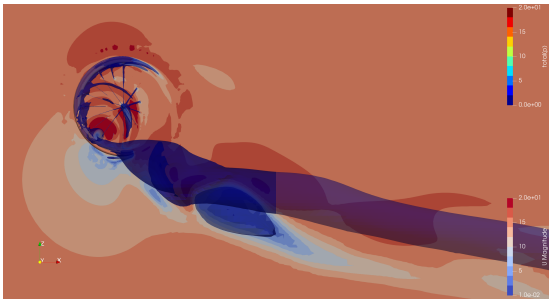

(d) Moving Reference Frame - Cylinder $r = 0.40cm$

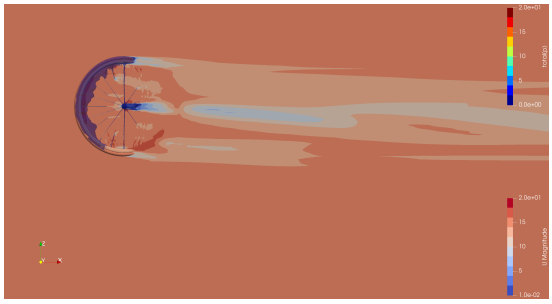

(e) Moving Reference Frame - Surface Extrusion 1 mm

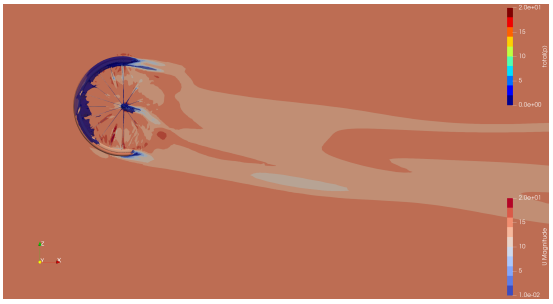

(f) Moving Reference Frame - Surface Extrusion 1 cm

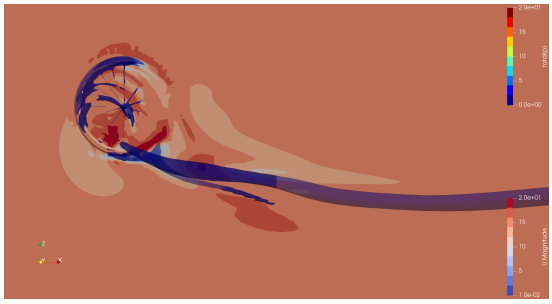

(g) Moving Reference Frame - Surface Extrusion 5 cm

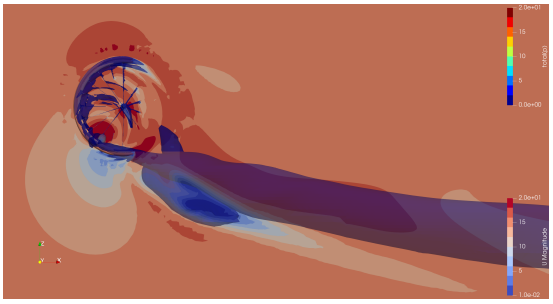

(h) Moving Reference Frame - Hybrid Model

(i) Moving Reference Frame - Surface Extrusion Spokes

Figure 5.20: Velocity field for different steady rotating models at 10 degrees of yaw angle

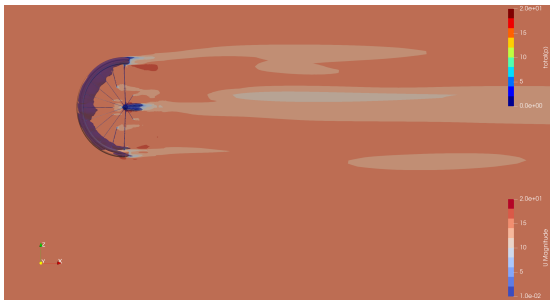

(a) Rotating Wall Boundary Condition

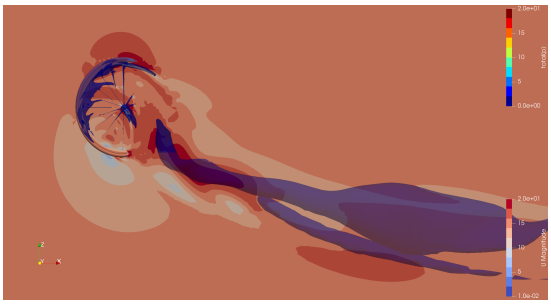

(b) Moving Reference Frame - Cylinder $r = 0.34cm$

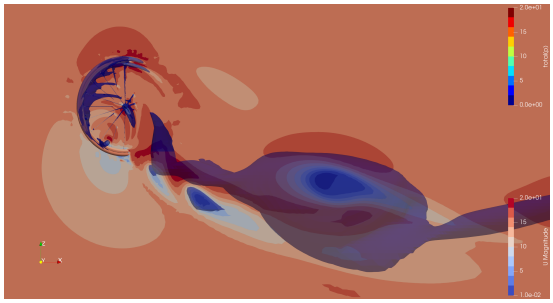

(c) Moving Reference Frame - Cylinder $r = 0.37cm$

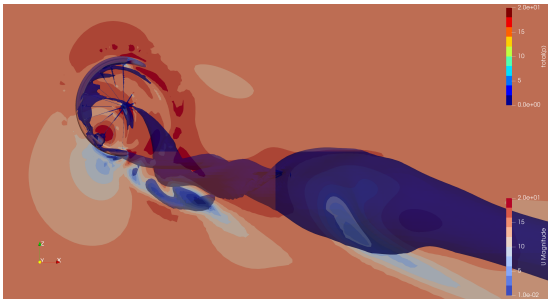

(d) Moving Reference Frame - Cylinder $r = 0.40cm$

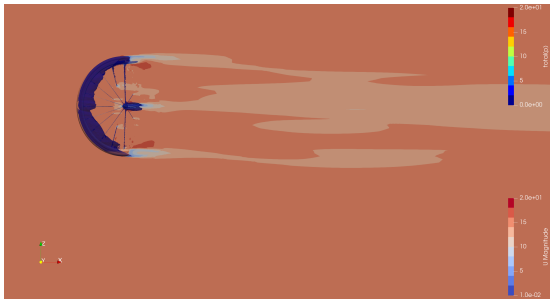

(e) Moving Reference Frame - Surface Extrusion 1 mm

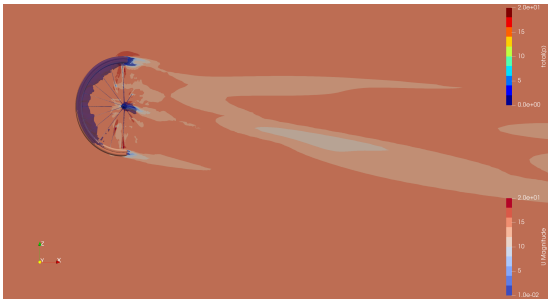

(f) Moving Reference Frame - Surface Extrusion 1 cm

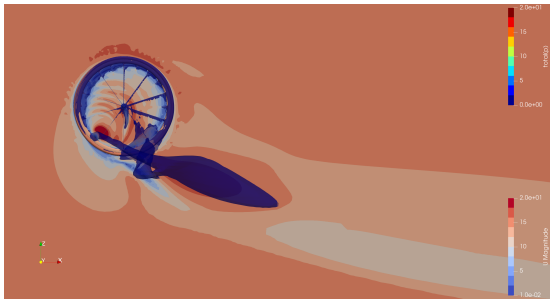

(g) Moving Reference Frame - Surface Extrusion 5 cm

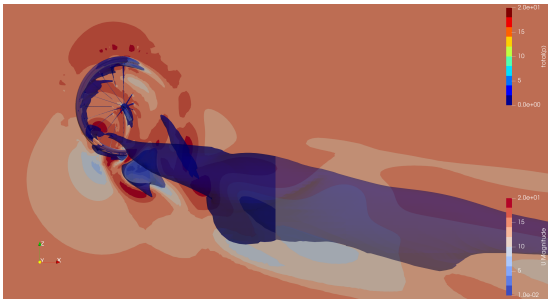

(h) Moving Reference Frame - Hybrid Model

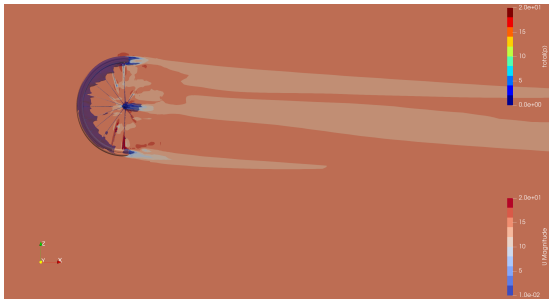

(i) Moving Reference Frame - Surface Extrusion Spokes

Figure 5.21: Velocity field for different steady rotating models at 20 degrees of yaw angle

Rotor Disk Model

In this section, an attempt to compare the rotor disc model approach with the previous RWBC case.

In the two tables, the numerical results of the drag force and lateral force at different yaw angles are shown, in this case to quantitatively compared the forces only the rim is taken into account. In fact, for this approach as explained in the numerical setup, the spokes are not meshed and they are substituted by a force model on the volume of their influence.

Steady State Models - Drag Force [N] on the rim (Percentage Difference compared to reference case)					
angle [°]	0	5	10	15	20
RWBC	1.02	1.20	1.31	1.71	1.80
rimDisk	1.08 (6%)	1.38 (15%)	1.45 (11%)	1.67 (2%)	1.93 (7%)

Steady State Models - Lateral Force [N] on the rim (Percentage Difference compared to reference case)					
angle [°]	0	5	10	15	20
RWBC	0	1.61	2.46	3.03	4.00
rimDisk	0	1.43 (12%)	2.58 (5%)	2.90 (4%)	3.92 (2%)

The forces comparison for what concerns the rim shows interesting results. The relative error stays for most of the cases under the 10%. Only at a 5-yaw angle the force is overestimated in the drag direction and underestimated in the lateral direction, and at 10 yaw angle is overestimated at 11%.

The good behavior of the model is also confirmed by the Cp plot. Indeed, at 0, 5, and 10-yaw angles, even if the discrepancies of the forces are present, the pressure coefficient curves show good agreement. Only at 15 and 20 deg, the same differences can be noticed, especially in the zone behind the wheel, so between angles 90 and 270. This behavior can be linked to the spokes presence, in which the interaction with the flow is averaged in the case of the model, while with RWBC the spokes remain in the same position leading to some pressure peaks which can influence the pressure on the rim.

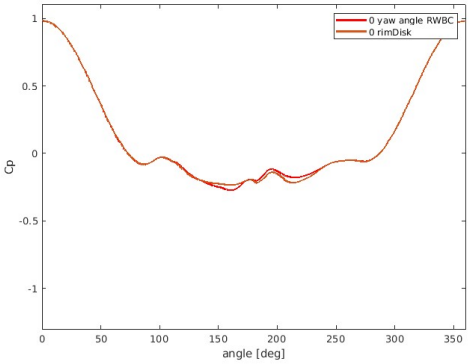

(a) 0 yaw angle

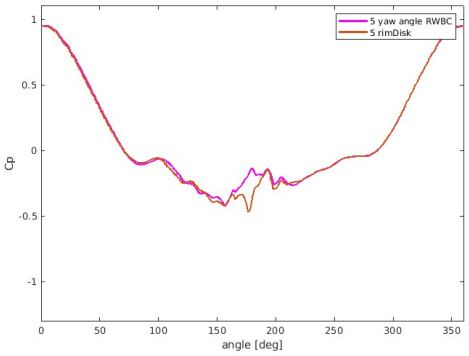

(b) 5 yaw angle

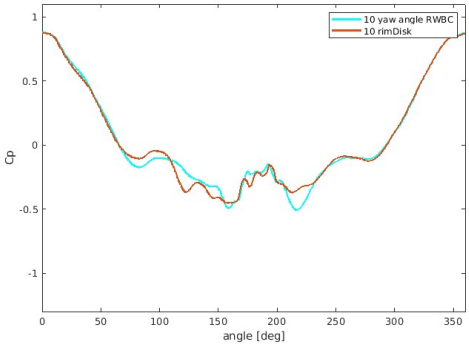

(c) 10 yaw angle

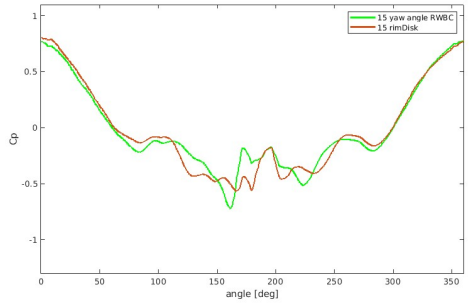

(d) 15 yaw angle

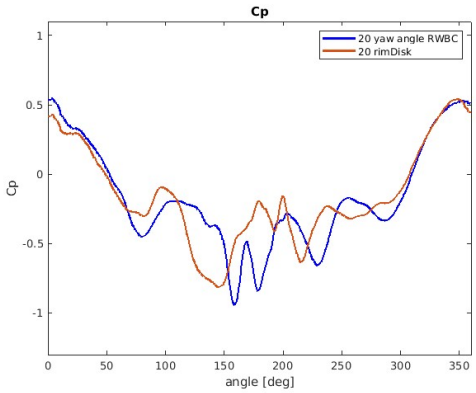

(e) 20 yaw angle

Figure 5.22: Cp profile at different yaw angle

The last step to validate the rotor disk model is a qualitative comparison of the velocity field and iso surface pressure. At 0 yaw angle, the RWBC approach shows a bigger low-velocity zone behind the rim, and between the spokes, it can be noticed an almost symmetric behavior between the upper and lower half, while considering the rotor disc approach, the wake is slightly more severe, but inside the rim, an high and low-velocity zone can be seen. For the other cases, the behavior is similar. Indeed, at 10 yaw angle,

the low-velocity zone colored in salmon is wider for the rotor disc approach and also is present inside the rim in the upper half where the spokes should rotate in the opposite direction with repsect ot the main velocity. Also at 20 yaw angle, the upper wake is more extended than in the RWBC approach. Also in this case the model is visible through the presence of the dot inside the rim.

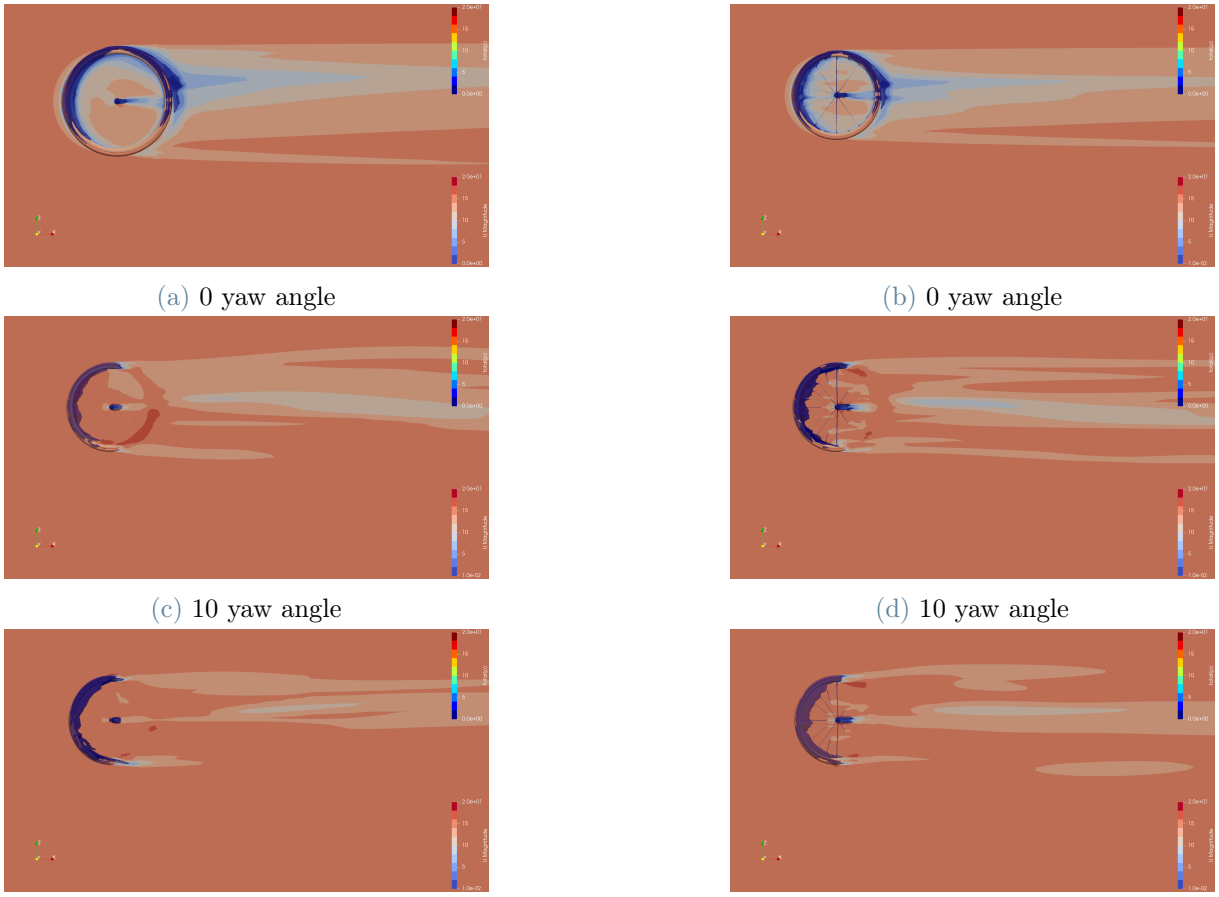

(a) 0 yaw angle

(b) 0 yaw angle

(c) 10 yaw angle

(d) 10 yaw angle

(e) 20 yaw angle

(f) 20 yaw angle

Figure 5.23: Velocity field compared between rotor disk model and RWBC

5.2.2. Unsteady Models

The unstable solution for incompressible flow, *pimpleFoam*, offered by OpenFoam, is employed in these situations. As mentioned in the preceding chapter, the results are the root mean square for the last two rotations.

DDES Case

This experimental setup aims to perform a comparative analysis of turbulence modeling by adopting an alternative approach to solving turbulence within a rotational model. In this study, the DDES (Delayed Detached Eddy Simulation) method is used to account for turbulence effects, while the MRF (Multiple Reference Frame volume methods is used to simulate rotation. The MRF volume is specifically configured to represent a lenticular wheel with a thickness of 1 mm.

In the present case, the drag force is determined by averaging the measurements of the last two complete rotations. The resulting resistance force is 1.35 N, which is 17% lower than in the reference case. This discrepancy can be attributed to the choice of turbulence model as well as the limitations of the mesh used in this computationally intensive method. In particular, the present simulation uses wall functions for the calculation of boundary layers and shear forces instead of resolving them explicitly.

It must be emphasized that at a yaw angle of 0 degrees, the drag force is evenly distributed between pressure and viscous forces. In this case, the viscous forces contribute 60% of the total drag force. Considering the large surface area, a more comprehensive analysis could be performed with DDES by increasing the number of elements and including additional layers as shown in previous cases.

The aim of this simulation is twofold: to achieve higher accuracy in the estimation of force magnitudes and to serve as the first implementation of the DDES turbulence model in the OpenFOAM software. The results obtained show promising trends that require further investigation and validation of this model.

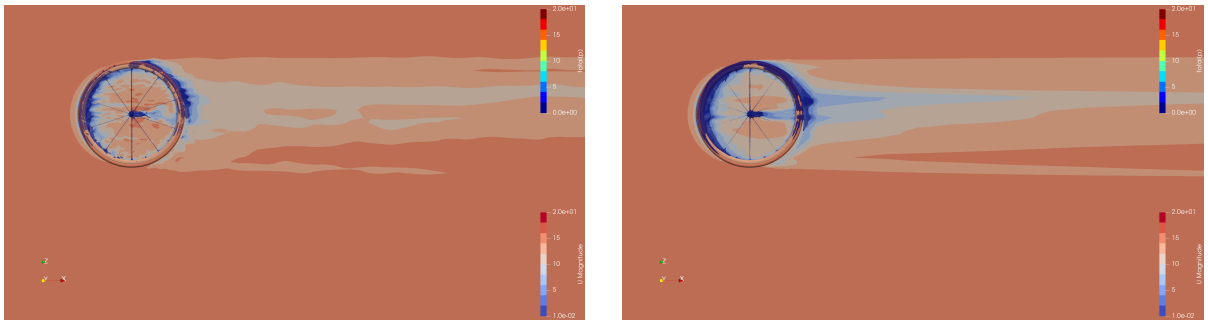

(a) DDES (b) RWBC

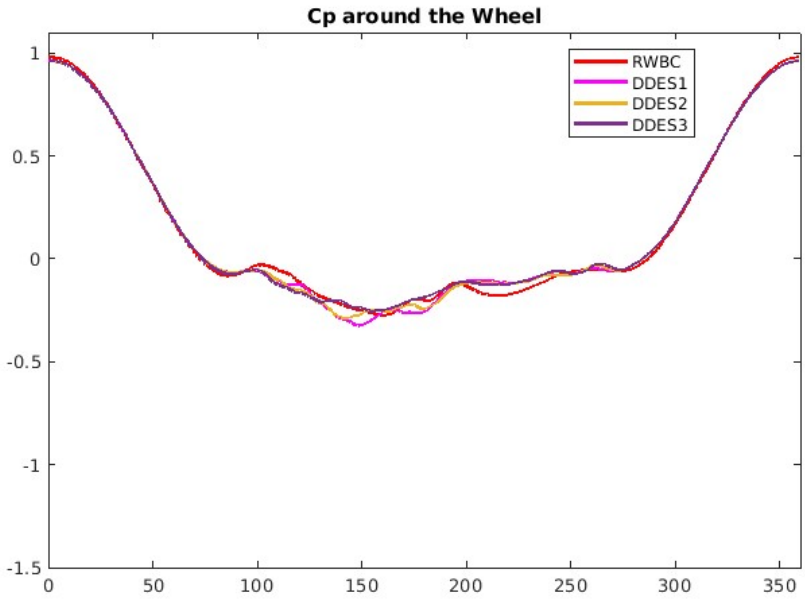

Figure 5.25: C_p profile around the wheel for DDES and RWBC

Even if the drag force value shows some discrepancies the C_p plot confirms the trend of the pressure around the wheel computed by RWBC. The two curves overlaps and it can be noticed how the unsteady behaviour characterized the pressure on the last time steps leading to slight different pressure coefficient plots.

Sliding Mesh

The utilization of the sliding mesh rotational method significantly amplifies the computational requirements for the simulation. Specifically, it necessitates the use of an unsteady solver, *pimpleFoam*, to effectively simulate the rotation of the wheel. During each time step, the mesh which covers the wheel moves within the domain to accurately replicate its rotation. The virtual duration of the simulation is 1 second, which corresponds to seven complete rotations of the wheel. However, the results are derived by applying the root mean square definition solely to the last two full rotations.

The computed results are presented in the subsequent tables, where a comparison is made between the obtained values and those from the reference case. The analysis covers the examination of drag forces and lateral forces, with the relative errors provided within parentheses.

Steady State Models - Drag Force [N] (Percentage Difference compared to reference case)					
angle [°]	0	5	10	15	20
RWBC	1.62	1.96	2.24	2.50	2.54
SM	1.45 (11%)	1.82 (7%)	2.15 (4%)	2.31 (8%)	2.40 (6%)

Steady State Models - Lateral Force [N] (Percentage Difference compared to reference case)					
angle [°]	0	5	10	15	20
RWBC	0	1.48	2.45	3.05	4.23
SM	0	1.34 (10%)	2.30 (6%)	2.63 (14%)	3.35 (21%)

The quantitative results underestimate in all the cases the value computed by RWBC. In particular, the reason associated is the different boundary conditions that aim to substitute the rotation of the geometry. Unfortunately, OpenFOAM is not able to build enough qualitative mesh to compute the rotation of the geometry maintaining stable the simulation.

At 0 yaw angle, the force is 11% lower, but the computed results share equally the contribution of this force between the spokes and the rim, while in the previous case, the major contribution was given mostly by the rim. Also for this case, to diminish the number of cells and maintain a higher quality of the mesh, the boundary layer is not

present so for what concern the viscous force its value can be underestimated as well. Even in the other cases, the forces are underestimated at every yaw angle.

Moreover, the pressure plots show a Cp value around 0 for the whole part behind the wheel, i.e. between 90 to 270 deg. The higher static pressure could be linked to the lower pressure drag simulated in the y direction.

Unfortunately, because of the unsteadiness of the methods, an average plot of the pressure coefficient around the wheel is not possible. Indeed the cells are attached to the wheel and at every time step they change the angle position concerning the absolute reference system. To compare, at least qualitatively the pressure coefficient around the wheel, the coefficient is plotted and compared to the reference case at different time steps. Particularly they are chosen randomly to cover three different possible scenarios.

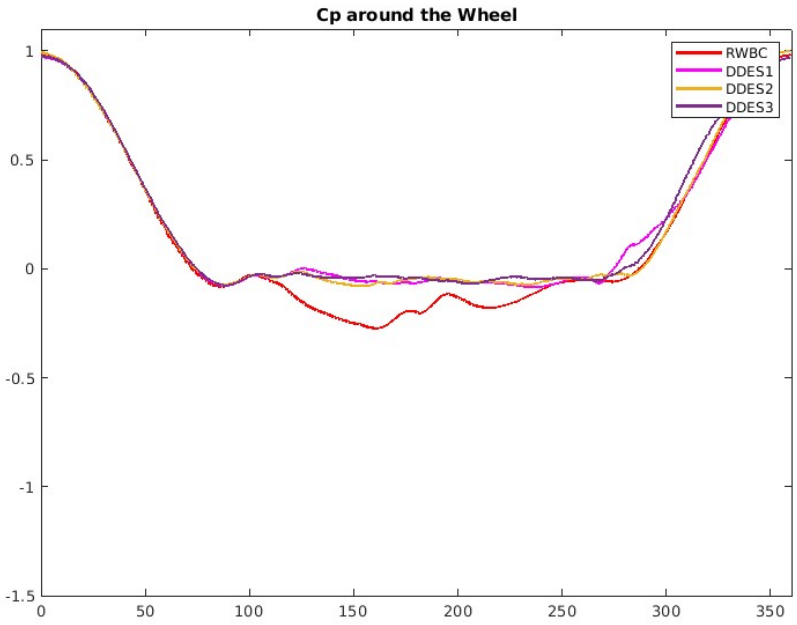

Figure 5.26: C_p profile around the wheel at different time steps

Also, these time steps are compared qualitatively looking at the velocity field and at different yaw angles.

At this point also the flux at 0 around the wheel is shown graphically in the next figure:

At the 0-yaw angle, three different graphical examples are available to show the different positions of the spokes. For all three cases, the wake and the iso pressure surface have a lower influence in terms of dimensions, indeed the pressure surface is present just on the

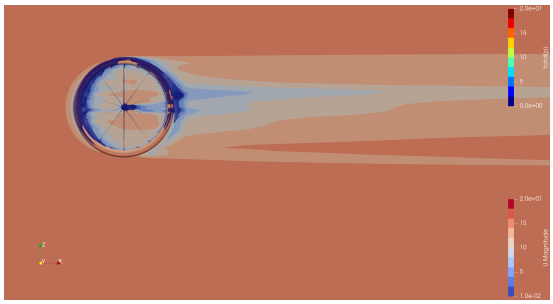

(a) Rotating Wall Boundary Condition

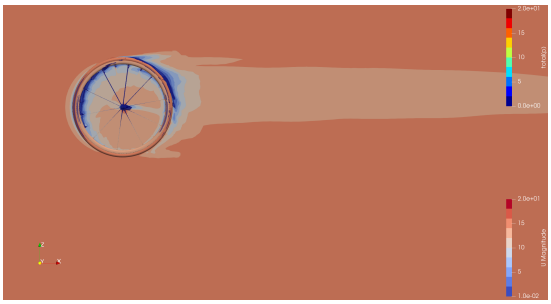

(b) Sliding Mesh

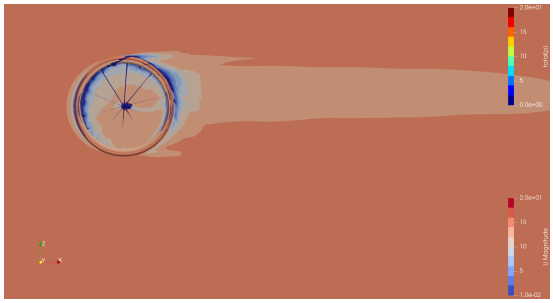

(c) Sliding Mesh

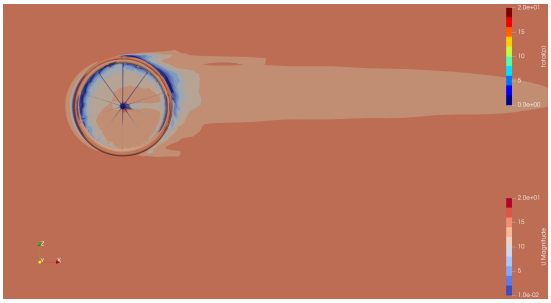

(d) Sliding Mesh

Figure 5.27: Velocity field for SM at 0-yaw angle

upwind section of the rim and on the spokes on the upper part which are the ones that rotate against the wind. Also, the wake does not show the low-velocity surface indicated with the blue color.

6 | Conclusion

This thesis conducted a comprehensive comparison of rotational approaches for simulating bike wheels, with a specific focus on lenticular and spoked wheel cases. Initially, the model was validated using the MRF (Multiple Reference Frame) volume method, employing the extrusion of the CAD file of the disc wheel with a thickness of 1 mm. The rotational approach exhibited favorable agreement with results obtained from testing conducted in the Politecnico di Milano wind tunnel.

The first wheel investigated was the lenticular wheel. Its rotation was simulated using the RWBC (Rotating Wall Boundary Condition), which served as the reference case for scenarios at different yaw angles. Subsequently, various approaches utilizing the MRF method were explored, and it was found that only the approach used for validation showed agreement with the RWBC. This led to the initial conclusion that while the MRF method can yield results with good residuals and reduced computational requirements, its application is highly sensitive to the volume considered. A quantitative and qualitative comparison of different setups revealed consistent relative errors in the computed forces, both underestimating and overestimating, without establishing a definitive relationship between the application of the MRF and the output values.

For the steady solver, another comparison was conducted to showcase the robustness of the results, which were compared with the output of AeroCloud. Despite obtaining the rotation of the model in two different ways, the drag force, particularly with regard to the sailing effect, exhibited comparable results.

Regarding the lenticular wheel, the thesis also compared results obtained from unsteady solvers. Specifically, the DDES (Delayed Detached Eddy Simulation) at 0 yaw angle demonstrated favorable agreements in terms of wake and pressure coefficient, albeit with slightly lower computed forces. On the other hand, the sliding mesh approach, which effectively simulated the rotation, exhibited strong correlations with the RWBC.

The second wheel analyzed in this thesis was the spoked wheel. In addition to simulating and comparing previous setups, new approaches were implemented to further investigate its behavior. Similar to the previous case, the MRF volume obtained through the disc

wheel CAD file and a thickness of 1 mm demonstrated outstanding performance in terms of computational time and resulting flow. Adopting the extrusion of the rim and spokes themselves with a small thickness as the MRF also allowed for simulating the flow with comparable computational resources. The hybrid approach technique showed interesting results at 0 yaw angle but exhibited very complex turbulence structures as the yaw angle increased.

For this setup, a new approach was introduced, inserting volume forces instead of the spokes. The comparison of forces and the plot of pressure coefficients showed promising values for further application. Moreover, the flow exhibited reasonable results at every yaw angle, which is remarkable considering it was the first application and contributed to enhancing mesh quality.

Even for this case, unsteady models were implemented. The DDES case provided interesting results, with the flow, wake, and computed values aligning closely at 0 yaw angle. The pressure coefficient curves at three different time steps were compared, mostly following the reference case (RWBC). Finally, the sliding mesh approach was analyzed, confirming the good estimation of the steady solver for the best MRF cases. This is promising considering the inherent unsteadiness of the problem due to the presence of spokes. Three qualitatively different velocity field figures were plotted, revealing a less severe wake behind the wheel and more complex structures inside the spokes, but the average structure remained comparable.

6.1. Future Development

This study examines the influence of rotational models and explores the implementation of the DDES method to provide additional comparisons. The main limitations of this study are briefly discussed, which can be addressed and investigated in future research.

The investigation of the wheel-ground contact impact was not included, and the turbulence model adopted was the $k-$ model, leaving room for further exploration of alternative turbulence approaches. The CFD simulations were conducted under low turbulence level approach flow conditions and compared with wind tunnel measurements obtained under similar conditions. While this is a common practice, additional investigations can be conducted to better represent real-world scenarios.

Moreover, in the case of unsteady simulations, a mesh convergence study should be conducted, and a dedicated investigation for this method is warranted. Additionally, alternative approaches for modeling the yaw angle can be explored and compared. The study

presents two main methods for simulating crosswinds: geometry movement and applying different boundary conditions. However, the validation of the second approach is lacking, and further research in this direction is recommended. This approach eliminates the need to remesh the geometry for each yaw angle variation, but a further investigation on the reliability of the boundary condition must be analyzed. Unfortunately, with this setup the direct comparison with the wind tunnel experiment cannot be properly made, hence all the results obtained with SM in this thesis must be taken into account carefully.

Considering the extensive number of simulations in this study, implementing an automated post-processing method, similar to AeroCloud, can streamline data analysis and enable a focus on optimizing wheel performance.

Finally, it is important to acknowledge that assessing the final performance of a cyclist requires considering the entire cycling system, including all bicycle components.

Bibliography

[1] Basics of Y Plus, Boundary Layer and Wall Function in Turbulent Flows. URL https://www.learncax.com/knowledge-base/blog/by-category/cfd/basics-of-y-plus-boundary-layer-and-wall-function-in-turbulent-flows.

[2] ITALY IS THE NEW MEN'S TEAM PURSUIT OLYMPIC CHAMPION. URL https://pinarello.com/global/en/news/italy-are-the-new-men-s-team-pursuit-olympic-champions.

[3]

[4] N. T. Basse. Turbulence intensity scaling: A fugue. *Fluids*, 4(4):1–13, 2019. ISSN 23115521. doi: 10.3390/fluids4040180.

[5] D. Berzi. Fluid Mechanics, lecture notes. chapter Turbulence. Politecnico di Milano, Italy, 2019.

[6] B. Blocken. Computational fluid dynamics for urban physics: Importance, scales, possibilities, limitations and ten tips and tricks towards accurate and reliable simulations. *Building and Environment*, 91:219–245, 2015. ISSN 0360-1323. doi: https://doi.org/10.1016/j.buildenv.2015.02.015. URL https://www.sciencedirect.com/science/article/pii/S0360132315000724. Fifty Year Anniversary for Building and Environment.

[7] E. C.R.Kyle. Improving the racing bicycle. *Mechanical Engineering*, 106:34–35, 9 1984.

[8] B. D. L. Z. e. a. Crouch, T.N. Riding against the wind: a review of competition cycling aerodynamics. *Sports Eng*, 20:81–110, 5 2017. doi: https://doi.org/10.1007/s12283-017-0234-1.

[9] K. E. H. P. C. J. Defraeye T, Blocken B. Aerodynamic study of different cyclist positions: Cfd analysis and full-scale wind-tunnel tests. *Biomech*, 43:1262–1268, 7 2010. doi: 10.1016/j.jbiomech.2010.01.025.

[10] W. Froude, W. T. David, and D. Stefan. *The Elementary Relation between Pitch, Slip, and Propulsive Efficiency*. Inst. Naval Architects, 1878.

[11] G. Gibertini, G. Campanardi, L. Guercilena, e. C. T. Macchi, C.", and J. C. H. Goh. Cycling aerodynamics: Wind tunnel testing versus track testing. In *6th World Congress of Biomechanics (WCB 2010). August 1-6, 2010 Singapore*, pages 10–13, Berlin, Heidelberg, 2010. Springer Berlin Heidelberg. doi: 10.1007/978-3-642-14515-5_3.

[12] M. Godo, D. Corson, and S. Legensky. An aerodynamic study of bicycle wheel performance using cfd. 01 2009. ISBN 978-1-60086-973-0. doi: 10.2514/6.2009-322.

[13] M. Godo, D. Corson, and S. Legensky. A practical analysis of unsteady flow around a bicycle wheel, fork and partial frame using cfd. 01 2011. ISBN 978-1-60086-950-1. doi: 10.2514/6.2011-1237.

[14] F. Grappe, R. Candau, A. Belli, and J. Rouillon. Aerodynamic drag in field cycling with special reference to the obree's position. *Ergonomics*, December 1:1299–1311, 12 1997. doi: 10.1080/001401397187388.

[15] D. I. Greenwell, N. J. Wood, E. K. L. Bridge, and R. J. Addy. Aerodynamic characteristics of low-drag bicycle wheels. *The Aeronautical Journal*, 99(983):109–120, 1995. doi: 10.1017/S0001924000028281.

[16] J. Guerrero. Turbulence modeling in openfoam: Theory and applications, 2021. URL `http://www.wolfdynamics.com/training/turbulence/OF2021/turbulence_2021_OF8.pdf`.

[17] T. Hobeika and S. Sebben. Cfd investigation on wheel rotation modelling. *Journal of Wind Engineering and Industrial Aerodynamics*, 174:241–251, 2018. ISSN 0167-6105. doi: https://doi.org/10.1016/j.jweia.2018.01.005. URL `https://www.sciencedirect.com/science/article/pii/S0167610517307286`.

[18] M. Lanfrit. Best practice guidelines for handling automotive external aerodynamics with fluent. *Fluent Deutschl. GmbH Birkenweg 14a 64925 Darmstadt/Germany*, 2005.

[19] S. G. G. P. S. O. M. Belloli, P. Schito and C. Somaschini. Aerodynamic investigations of a standalone rotating bicycle wheel. 2020.

[20] F. Malizia and B. Blocken. Bicycle aerodynamics: History, state-of-the-art and future perspectives. *Journal of Wind Engineering and Industrial Aerodynamics*, 200:104134,

2020. ISSN 0167-6105. doi: https://doi.org/10.1016/j.jweia.2020.104134. URL https://www.sciencedirect.com/science/article/pii/S0167610520300441.

[21] F. Malizia and B. Blocken. Cfd simulations of an isolated cycling spoked wheel: Impact of the ground and wheel/ground contact modeling. *European Journal of Mechanics - B/Fluids*, 82:21–38, 2020. ISSN 0997-7546. doi: https://doi.org/10.1016/j.euromechflu.2020.02.002. URL https://www.sciencedirect.com/science/article/pii/S0997754619306144.

[22] F. Malizia and B. Blocken. Cfd simulations of an isolated cycling spoked wheel: The impact of wheel/ground contact modeling in crosswind conditions. *European Journal of Mechanics - B/Fluids*, 84:487–495, 2020. ISSN 0997-7546. doi: https://doi.org/10.1016/j.euromechflu.2020.07.009. URL https://www.sciencedirect.com/science/article/pii/S0997754620301965.

[23] F. Malizia, H. Montazeri, and B. Blocken. Cfd simulations of spoked wheel aerodynamics in cycling: Impact of computational parameters. *Journal of Wind Engineering and Industrial Aerodynamics*, 194:103988, 2019. ISSN 0167-6105. doi: https://doi.org/10.1016/j.jweia.2019.103988. URL https://www.sciencedirect.com/science/article/pii/S0167610519305884.

[24] B. B. Malizia F., van Druenen T. Impact of wheel rotation on the aerodynamic drag of a time trial cyclist. *Sports Engineering*, 24(1), 2021. ISSN 1460-2687. doi: 10.1007/s12283-021-00341-6. URL https://doi.org/10.1007/s12283-021-00341-6.

[25] N. N. Mansour, J. Kim, and P. Moin. Near-wall k-ϵ turbulence modeling. *AIAA Journal*, 27(8):1068–1073, 1989. ISSN 00011452. doi: 10.2514/3.10222.

[26] B. M. M. D. Martin JC, Gardner AS. Modeling sprint cycling using field-derived parameters and forward integration. *Med Sci Sports Exerc*, 38:592–597, 3 2006. doi: 10.1249/01.mss.0000193560.34022.04.

[27] C. J. M. K. C. A. Martin JC, Milliken DL. Validation of a mathematical model for road cycling power. *Appl Biomech.*, 14:276–291, 3 1998. doi: 10.1123/jab.14.3.276.

[28] A. D. Monte, L. Leonardi, C. Menchinelli, and C. Marini. A new bicycle design based on biomechanics and advanced technology. *International Journal of Sport Biomechanics*, 3(3):287 – 292, 1987. doi: 10.1123/ijsb.3.3.287. URL https://journals.humankinetics.com/view/journals/jab/3/3/article-p287.xml.

[29] P. Norman. 2023 men's worldtour team bikes and equipment | who's

riding what?, 2023. URL https://www.bikeradar.com/features/pro-bike/worldtour-bikes/.

[30] M. Pogni and N. Petrone. Comparison of the aerodynamic performance of five racing bicycle wheels by means of cfd calculations. *Procedia Engineering*, 147:74–80, 2016. ISSN 1877-7058. doi: https://doi.org/10.1016/j.proeng.2016.06.192. URL https://www.sciencedirect.com/science/article/pii/S1877705816306397. The Engineering of SPORT 11.

[31] S. Pope. *Turbulent Flows*. Cambridge University Press, 2000.

[32] M. P. S. F. Prampero PE, Cortili G. Equation of motion of a cyclist. *J Appl Physiol Respir Environ Exerc Physiol*, 47:201–206, 1 1979. doi: 10.1152/jappl.1979.47.1.201.

[33] S. M. Richardson. *Fluid mechanics*. 9th edition edition, 1989. ISBN 0891166718. doi: 1260258319.

[34] C. B. Silva and J. C. F. Pereira. Analysis of the gradient-diffusion hypothesis in large-eddy simulations based on transport equations. *Physics of Fluids*, 19(3), 03 2007. ISSN 1070-6631. doi: 10.1063/1.2710284. URL https://doi.org/10.1063/1.2710284. 035106.

[35] G. Tew and A. Sayers. Aerodynamics of yawed racing cycle wheels. *Journal of Wind Engineering and Industrial Aerodynamics*, 82(1):209–222, 1999. ISSN 0167-6105. doi: https://doi.org/10.1016/S0167-6105(99)00034-3. URL https://www.sciencedirect.com/science/article/pii/S0167610599000343.

[36] S. Wahono. Development of virtual blade model for modelling helicopter rotor downwash in openfoam. 2013.

[37] D. Wilcox. *Turbulence Modeling for CFD*. DCW Industries, 2010.

List of Figures

List of Tables

Acknowledgements